

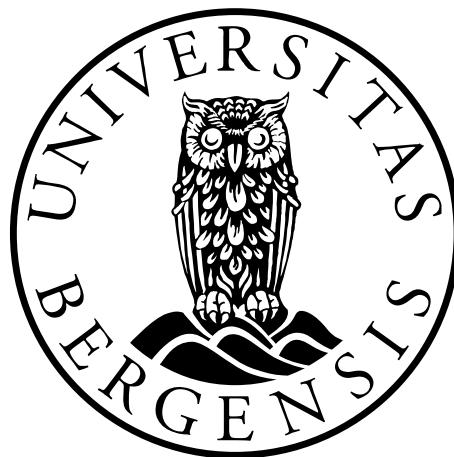
---

# Monte Carlo simulations of neutron based in-vivo range verification in proton therapy – characteristics of proton-induced secondary particles

---

**Eidi Helland**

Supervisors: Kristian Smeland Ytre-Hauge and Ilker Meric



Master thesis in medical physics and technology

Department of Physics and Technology

University of Bergen

December 2019



# Acknowledgements

First of all, I would like to thank my supervisors, Dr. Kristian S. Ytre-Hauge and Dr. Ilker Meric.

Thank you, Kristian, for presenting me with the topic of my thesis and for introducing me to the interesting and exciting field of proton therapy. Your help and guidance throughout this project have been invaluable. You have provided me with inspiration and all the necessary tools to write this thesis and have made this an enjoyable experience. Thank you, Ilker, for your helpful guidance and feedback in our meetings. Your thoughts and input have elevated my thesis. I would also like to thank Ph.D. candidate Lars Fredrik Fjæra for your useful python scripts applied for the patient plan in this thesis, as well as your help when I had technological difficulties with FLUKA and other installations.

Thank you to all my friends and to my fellow physics students, and especially thanks to Janne Therese Syltøy for all the help, conversations and support you have given me over the last five years. I appreciate our friendship and it's been a pleasure working with you all these years.

A special thanks to my loving and wonderful family, my mother, father, brother and sister. Your support has been invaluable, and I am forever grateful. Finally, I would like to thank Remy for your love and encouragement during this period. You have always been there, and I am thankful for everything you have done for me.

Bergen, December 2019

Eidi Helland



# Abstract

Radiation therapy is an important treatment modality within cancer treatment, with the aim to deliver a high dose to the target volume while sparing the surrounding tissue. Protons have favourable characteristics of depositing the treatment dose more conformal compared to conventional photon therapy, motivating further development and improvement within proton therapy. Despite the beneficial qualities of proton radiation, uncertainties in the proton beam range prevents full exploitation of proton therapy's potential to reduce dose to healthy tissues compared to photon therapy. Detection of secondary neutrons created in the patient through nuclear interactions, has been proposed as a method for monitoring the proton beam range during treatment, as there has been shown a correlation between the spatial neutron production distribution and the beam range. However, other generated secondaries may interfere with the secondary neutron detection. The amount and distribution of different secondaries which may reach the proposed neutron detector has not yet been investigated.

The overall objective of this thesis was therefore to use Monte Carlo (MC) simulations to quantify the production of secondary radiation, including protons, prompt gamma-rays, neutrons and alpha particles. This knowledge is essential for estimating interference from the different secondary particle species on the measurements of secondary neutrons for the purposes of range monitoring.

The production of secondary radiation was examined for two cases: a water phantom and a clinical treatment plan for a patient. MC simulations were conducted with the FLUKA MC simulation package. The water phantom was simulated with clinically relevant monoenergetic proton beams of 100, 160, 200 and 230 MeV, and the clinical treatment plan imported to FLUKA had beam energies between 93-197 MeV. A hydrogen-rich material, converting neutrons to protons, and two particle detectors were implemented in FLUKA.

A clear resemblance between the results from the water phantom and the patient treatment plan was seen. The results indicated that secondary protons had the highest production rate, followed by secondary neutrons and prompt gamma-rays. Alpha particles were observed to have little potential relevance on the neutron measurements. Towards the converter surface, secondary protons had the highest reduction compared to the production rate and prompt

gamma-rays and neutrons were the dominating secondaries at the converter surface. The proportion of protons reaching the converter and their energy was found sensitive to the phantom size, indicating that the ratio between the secondaries can vary for each patient case, with more protons reaching the converter for smaller patients.

Possible shielding methods in order to reduce potential noise from unwanted secondary radiation in the detector can be adding a layer of lead or tungsten prior to the converter surface, in order to stop and absorb protons and to some degree gamma-rays, while secondary neutrons can traverse and convert to detectable protons.



# Contents

<b>ACKNOWLEDGEMENTS.....</b>	<b>III</b>
<b>ABSTRACT.....</b>	<b>V</b>
<b>CONTENTS.....</b>	<b>VIII</b>
<b>1. INTRODUCTION .....</b>	<b>1</b>
1.1 RADIOTHERAPY.....	1
1.2 PROTON THERAPY .....	3
1.3 PROTON RANGE UNCERTAINTIES .....	5
1.4 PROJECT OBJECTIVES.....	7
<b>2. PHYSICS OF PROTON THERAPY .....</b>	<b>8</b>
2.1 CHARGED PARTICLE INTERACTIONS WITH MATTER .....	8
2.1.1 <i>Stopping power</i> .....	9
2.1.2 <i>Coulomb scattering</i> .....	11
2.1.3 <i>Nuclear interactions</i> .....	12
2.1.4 <i>Linear energy transfer</i> .....	13
2.2 GAMMA-RAYS IN PROTON THERAPY .....	14
2.3 NEUTRONS IN PROTON THERAPY .....	15
2.4 DOSIMETRY AND DEPTH DOSE CURVES.....	16
2.4.1 <i>Absorbed dose</i> .....	16
2.4.2 <i>Relative biological effectiveness</i> .....	17
2.4.3 <i>Spread-out Bragg peak</i> .....	17
<b>3. IN-VIVO RANGE VERIFICATION IN PROTON THERAPY .....</b>	<b>19</b>
3.1 RANGE UNCERTAINTIES.....	19
3.2 IN-VIVO RANGE VERIFICATION METHODS .....	20



3.2.1	<i>Direct methods</i> .....	20
3.2.2	<i>Indirect methods</i> .....	21
3.3	SECONDARY NEUTRON DETECTION FOR IN-VIVO RANGE VERIFICATION .....	22
<b>4.</b>	<b>MATERIALS AND METHODS</b> .....	<b>25</b>
4.1	WATER PHANTOM SIMULATIONS .....	25
4.1.1	<i>FLUKA input</i> .....	25
4.1.2	<i>Scoring options</i> .....	28
4.1.3	<i>Simulation and graphical representation</i> .....	31
4.1.4	<i>Simulation with different water phantom thickness</i> .....	31
4.1.5	<i>Uncertainties</i> .....	31
4.2	PATIENT SIMULATIONS.....	32
4.2.1	<i>FLUKA input</i> .....	32
4.2.2	<i>Data analysis and visualization</i> .....	36
<b>5.</b>	<b>RESULTS</b> .....	<b>38</b>
5.1	WATER PHANTOM SIMULATIONS .....	38
5.1.1	<i>Dose distribution</i> .....	38
5.1.2	<i>Particle production in the water phantom</i> .....	40
5.1.3	<i>Particle fluence</i> .....	44
5.1.4	<i>Particle distribution at the converter</i> .....	51
5.1.5	<i>Particle rate comparison in the water phantom and at the detector surface</i> .....	54
5.1.6	<i>Geometry variation of the water phantom</i> .....	55
5.2	PATIENT SIMULATIONS.....	57
5.2.1	<i>Dose distribution</i> .....	57

5.2.2	<i>Particle production in the patient</i> .....	57
5.2.3	<i>Particle fluence</i> .....	60
5.2.4	<i>Particle distribution at the converter</i> .....	63
5.2.5	<i>Particle rate comparison in the patient and at the detector surface</i> .....	64
<b>6.</b>	<b>SUMMARY AND DISCUSSION</b> .....	<b>65</b>
6.1	WATER PHANTOM SIMULATIONS .....	65
6.2	PATIENT TREATMENT PLAN SIMULATIONS .....	67
6.3	COMPARISON BETWEEN THE THW WATER PHANTOM AND PATIENT PLAN SIMULATIONS .....	68
6.4	SUGGESTION FOR REDUCITON OF SECONDARY RADIATION NOISE .....	70
<b>7.</b>	<b>CONCLUSION AND FURTHER WORK</b> .....	<b>71</b>
	<b>BIBLIOGRAPHY</b> .....	<b>72</b>
	<b>APPENDIX A – FLUKA INPUT FILE</b> .....	<b>76</b>
	<b>APPENDIX B – TRACKING CODE</b> .....	<b>79</b>
	B.1 BXDRAW_RANGEVERIF.....	79
	B.2 QUANTITIES RESTORED .....	87
	<b>APPENDIX C – RESULTS FROM MC SIMUALTIONS</b> .....	<b>88</b>

## List of abbreviations

<b>3D-CRT</b>	<b>3D Conformal Radiation Therapy</b>
<b>BP</b>	<b>Bragg Peak</b>
<b>CPU</b>	<b>Central Processing Unit</b>
<b>CT</b>	<b>Computed Tomography</b>
<b>CTV</b>	<b>Clinical Target Volume</b>
<b>DICOM</b>	<b>Digital Imaging and COmmunications in Medicine</b>
<b>ENDF</b>	<b>Evaluated Nuclear Data File</b>
<b>FLUKA</b>	<b>FLUktuierende KAskade</b>
<b>FWHM</b>	<b>Full Width Half Maximum</b>
<b>GTV</b>	<b>Gross Tumour Volume</b>
<b>HU</b>	<b>Hounsfield Unit</b>
<b>ICRU</b>	<b>International Commission on Radiological Units and Measurements</b>
<b>IMPT</b>	<b>Intensity-Modulated Proton Therapy</b>
<b>IMRT</b>	<b>Intensity-Modulated Radiotherapy</b>
<b>LET</b>	<b>Linear Energy Transfer</b>
<b>LINAC</b>	<b>Linear Accelerator</b>
<b>MC</b>	<b>Monte Carlo</b>
<b>MCS</b>	<b>Multiple Coulomb Scattering</b>
<b>MLC</b>	<b>Multi Leaf Collimator</b>
<b>MRI</b>	<b>Magnetic Resonance Imaging</b>
<b>NIST</b>	<b>National Institute of Standards and Technology</b>
<b>NOVO</b>	<b>NeutrOn detection for real-time range VerificatiOn</b>
<b>OAR</b>	<b>Organ At Risk</b>
<b>PBS</b>	<b>Pencil Beam Scanning</b>
<b>PET</b>	<b>Positron Emission Tomography</b>
<b>PG</b>	<b>Prompt Gamma</b>
<b>PTV</b>	<b>Planning Target Volume</b>
<b>RBE</b>	<b>Relative Biological Effectiveness</b>
<b>SNR</b>	<b>Signal-to-Noise Ratio</b>
<b>SOBP</b>	<b>Spread-Out Bragg Peak</b>

**TPS**      **Treatment Planning System**  
**VMAT**    **Volumetric Modulated Arc Therapy**

# 1. Introduction

In 2018 there were 18.1 million new cases of cancer worldwide, where 9.6 million of these cases ended in death [1]. Cancer is one of the leading causes of death worldwide, therefore finding the best treatments and thereby reducing mortality is essential. Common cancer treatments are surgery, chemotherapy, immunotherapy and radiotherapy. The patients are often treated with a combination of these methods. Approximately 50 % of all cancer patients receive radiotherapy as a part of the treatment, making radiotherapy an important treatment modality within cancer treatment [2]. Radiotherapy is therefore an area in continuous development towards the best possible treatments. In radiotherapy, ionizing radiation is delivered to tumour cells with the aim to kill the cells by depositing energy. The main goal in radiotherapy is to deliver a high dose to the tumour while sparing and minimizing the dose to surrounding healthy tissue.

## 1.1 Radiotherapy

In 1895 X-rays were discovered by Wilhelm Conrad Röntgen. This had a huge impact on cancer treatment. Further, Antoine Henri Becquerel studied the phenomenon called radioactivity and started his research after natural radioactive sources. Marie and Pierre Curie discovered radium as a radioactive source in 1898. In the early 1900s there was an increase in the number of studies that reported use of X-ray and radium in medicine [3]. Since then, the use of and the technological advancements in radiotherapy have had a colossal growth, especially when Computed Tomography (CT) was introduced in 1971 by Godfrey Newbold Hounsfield. This had a big impact on radiotherapy as radiation treatment planning shifted from 2D to 3D.

In today's radiotherapy, the most common method is to deliver external beams of X-rays generated with a linear accelerator (LINAC) [4]. A LINAC is a particle accelerator that accelerates electrons to higher energies, from 4 to 25 MeV. For photon therapy, electrons are

accelerated and guided onto a target of high  $Z^1$  material to generate X-rays via bremsstrahlung interaction [5]. During the process of bremsstrahlung, electromagnetic radiation is created as a result of high-speed electrons being deflected and decelerated by a nucleus [6]. In the 1990s, multileaf collimators (MLC) driven by computerized algorithms were developed, resulting in accurate dose delivery with 3D dose sculpting [7]. This gave rise to 3D conformal radiotherapy (3D-CRT). The next big step forward in radiotherapy was in the mid-90s when intensity modulated radiotherapy (IMRT) was introduced. IMRT made it possible to modulate the intensity of the photon beam, allowing even more accurate sculpting of the dose field in 3D [7]. In 2007, volumetric modulated arc therapy (VMAT) was introduced, which is a type of IMRT technique where the gantry rotates around the patient while the beam is on, leading to an even better sparing of healthy tissue [8].

Definition of the tumour and target volumes in radiotherapy is essential for a successful treatment execution. In radiotherapy planning, there are three main volumes. The first is gross tumour volume (GTV), defined as the visible extent and location of tumour from diagnostic imaging. Surrounding tissue near the GTV may include sub-clinical spread (e.g. individual malignant cells) that cannot be fully clinical detected by medical imaging. The second volume, clinical target volume (CTV), includes additional margins to account for this spread. Lastly, the planning target volume (PTV) covers uncertainties within planning or treatment delivery [9]. The three main volumes for defining the target volume can be seen in Figure 1.

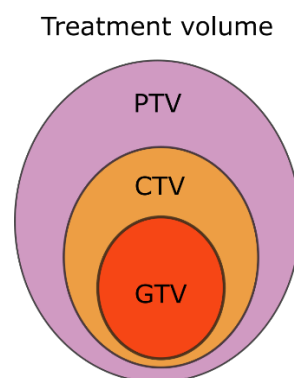


Figure 1: Illustration of the main volumes (GTV, CTV and PTV) related to define the target volume.

---

<sup>1</sup>  $Z$  is the atomic number of an element, representing the number of protons in the nucleus.

Photon therapy has improved significantly over the last decades, yet there are still limitations in the dose conformity of photon therapy due to the basic photon interactions and the dose deposition mechanism. The use of and interest in protons in radiation therapy has therefore increased worldwide as protons have clear dosimetric benefits compared to conventional radiotherapy using photons. Charged particles, like protons, have the ability to deliver their dose more accurately to the tumour with less integral dose to the surrounding tissues. This can reduce side effects and may improve the survival rates, motivating further development and improvement [10].

## 1.2 Proton therapy

The beginning of proton therapy was in 1946 when Robert Wilson published a paper where he proposed using a beam of accelerated protons to treat tumours deep inside the patient. Eight years later, in 1954, the first human was treated with proton beams at Lawrence Berkeley Laboratory [11]. One of the greatest advantages of using proton beams, compared to conventional photon beams, is how they deposit dose through matter. Photons will deposit maximum dose a few centimetres into the tissue, before the dose deposition decreases exponentially with depth. This results in a considerable amount of healthy tissue receiving dose, especially if the target of interest is located deep inside the patient. For protons on the other hand, the energy loss per unit length increases as the velocity of the proton decreases, giving rise to the so-called Bragg peak (see Figure 2). This results in maximum dose deposition at the end of the proton beam range, followed by a steep decline as the proton has stopped. Figure 2 shows typical depth-dose distributions for a proton and a photon beam through tissue, along with spread-out Bragg peak (SOBP). SOBP is the sum of several proton beams with different energies and intensities, generated in order to cover the entire target volume [6].

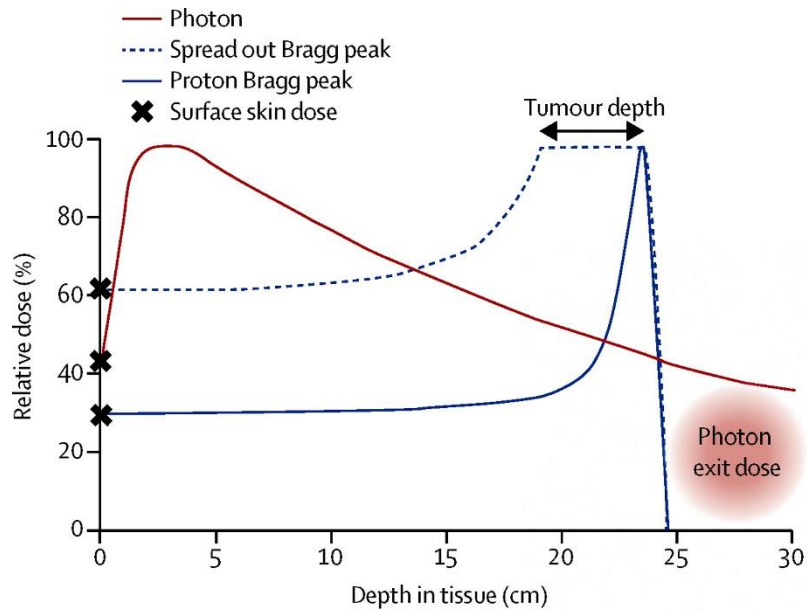


Figure 2: Illustration of depth dose curve for photons (solid red line), protons (solid blue line) and spread-out Bragg peak (SOBP) representing a combination of multiple proton beams (dashed blue line) [12].

Figure 3 shows the dose distribution for cranio-spinal irradiation with proton and photon beams. For conventional radiotherapy with photons a larger amount of integral dose is deposited throughout the patient, as the photons have no finite range, while for proton therapy the benefit of the Bragg peak is shown as a reduction in the integral dose and sparing of critical organs to a much better extent.

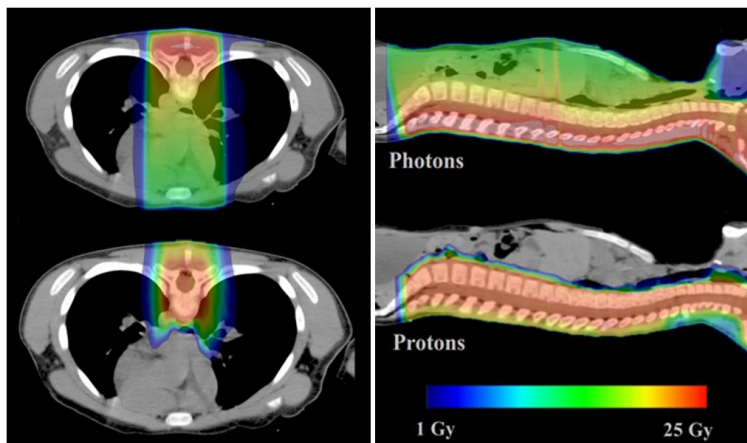


Figure 3: Illustration of the dose distribution for cranio-spinal radiation with proton and photon beams in the transverse and sagittal plane. The radiation fields enter the patient from the back. Irradiation with proton beams shows the significant dose reduction in healthy tissue and critical organs (e.g. lungs and heart) [13].



Protons for therapy are accelerated in a cyclotron or a synchrotron. The accelerated protons can be delivered through passive scattering or pencil beam scanning (PBS). With passive scattering, mechanical devices are inserted to widen and shape the beam according to the tumour, along with modulating the energy. However, new facilities make use of PBS. This is a method where dipole scanning magnets are used to steer the proton beam directly at the target, while changing the proton energy in order to irradiate multiple depths [4]. A sketch of the PBS principle is shown in Figure 4.

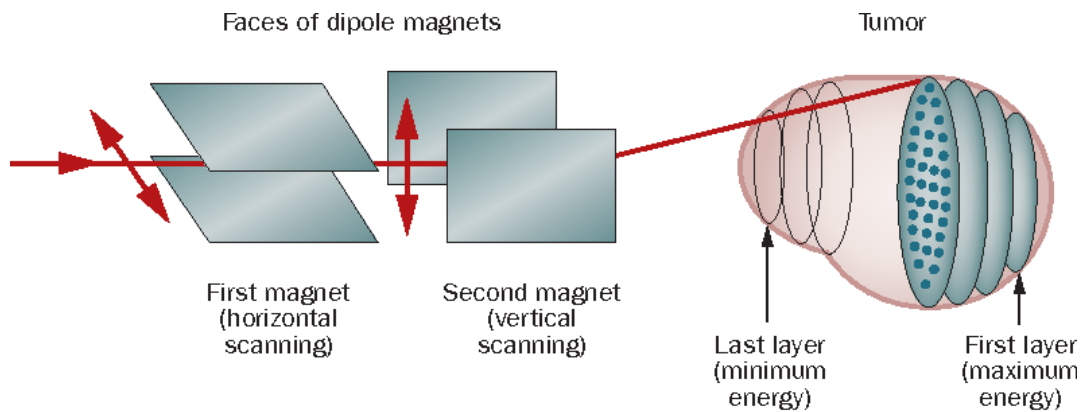


Figure 4: Illustration of pencil beam scanning. The proton beam is steered by dipole magnets, both horizontal and vertical. The target volume is divided into layers where each layer is covered by a grid of pixels to be irradiated. Required beam energy increases with depth [14].

Even though proton therapy provides superior dose distribution compared to conventional radiotherapy, there are some challenges which are not present in photon therapy. Range uncertainties is one example of this. As most of the dose is deposited at the end of the proton beam range, it is critical to know the necessary initial beam energy, how far the beam will penetrate and that it stops as predicted. Uncertainties in the proton beam range can lead to severe errors in dose deposition within the patient, and currently, uncertainties in the proton range makes it very challenging to treat patient groups where organ motion or large variation in tissue density (e.g. in the lungs and abdominal region) is present.

### 1.3 Proton range uncertainties

The depth-dose curve in Figure 5a illustrates the ideal situation of dose delivery in proton therapy. Here the Bragg peak is accurately positioned at the distal part of the tumour tissue. However, if one miscalculates the range, the result can be a much higher dose to healthy tissue

and an underdosage of the tumour. Range uncertainties are especially critical in cases where organs at risk (OAR) are located close to the target volume. Figure 5b illustrates how range uncertainties may have more severe adverse effects in proton therapy compared to conventional radiotherapy with photons.

One of the main sources of uncertainty in the proton beam range in tissue is the sensitivity to motion, which is inevitable due to e.g. respiratory motion and internal organ motion [15]. To minimize the adverse effects of range uncertainties, in-vivo beam range monitoring can be used. Different ways to do this is PET (Positron Emission Tomography), prompt gamma-ray (PG) imaging, direct dose measurement, MRI (Magnetic Resonance Imaging) and use of iono-acoustic signals [4, 16]. Some of these methods will be described later in chapter 3.

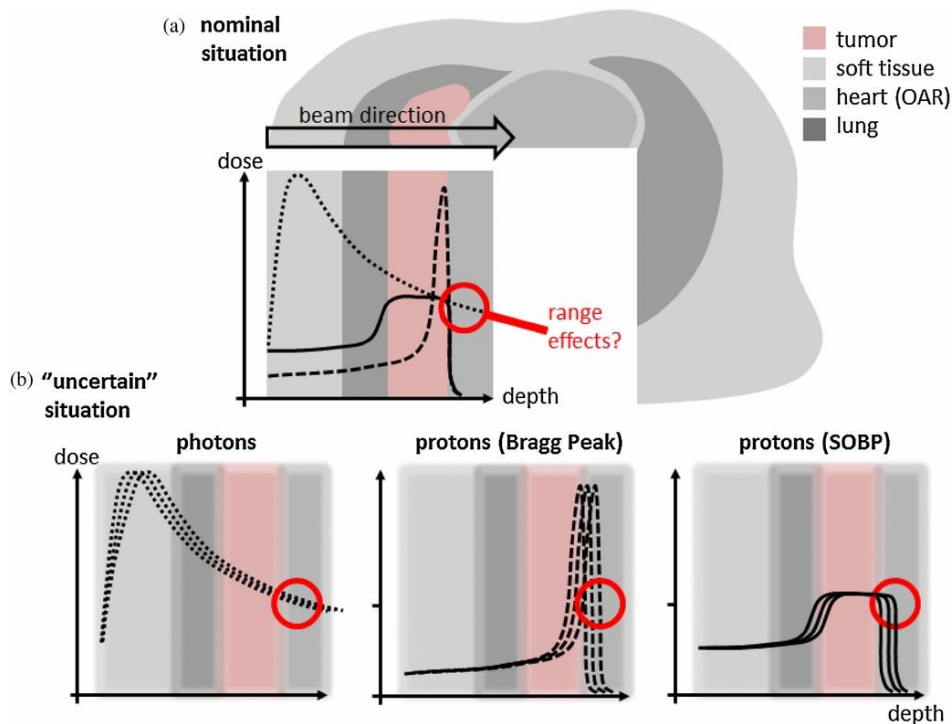


Figure 5: (a) Illustrates the benefits of proton therapy compared to photon therapy in an ideal situation. The dotted line represents depth dose curve for photon, dashed line for mono-energetic proton (Bragg peak) and solid line for SOBP. (b) The impact of range uncertainties, making photon therapy more robust towards uncertainties in radiation treatment [17].

When a proton beam propagates through a medium, many secondary particles are produced in nuclear interactions, such as gamma-rays, neutrons and protons. Detection of these secondary particles may contribute to reduce range uncertainties during treatment. Both gamma-rays and

large angle scattered protons have been suggested and investigated as range probes in proton therapy whereas detection of secondary neutrons as a range probe has until recently remained unexplored. Use of secondary neutrons as range probes has recently been suggested [18] and will be further investigated in this thesis.

## 1.4 Project objectives

Detection of secondary neutrons is a proposed method to monitor the range of the primary proton beam in the patient. By detecting secondary neutrons that are produced along the beam path, range verification for the proton beam may be accomplished as there is a correlation between neutron production yields and the proton beam range [18]. However, as mentioned above, other secondaries such as protons and gamma-rays are also produced during treatment and may interfere with the detection of neutrons. The main objective of this thesis is therefore to quantify the production of secondary radiation in proton therapy using Monte Carlo simulations. This includes estimation of production yields and energy distribution for neutrons, gamma-rays and alpha particles. In addition, the transport of these particles towards the proposed neutron detector system will be simulated to estimate the radiation field present at the detector surface during treatment. The secondary radiation will first be examined for monoenergetic proton beams on a water phantom to determine the general dependencies of secondary particle production, e.g. on the primary proton energy. Further a clinical treatment plan for prostate cancer will be simulated to estimate particle yields in a clinically realistic scenario. These data form the basis for further development of the proposed detector concept and may be used to assess if shielding of secondaries apart for neutrons is needed to reduce the potential interference from these particle species.

## **2. Physics of proton therapy**

When ionizing radiation passes through a medium and interacts with matter, energy from the incident particles is deposited in the medium. Energy transfer occurs when an electron from the atoms of the medium gets ejected. This happens if the particle beam has enough energy to knock off electrons. The ejected electrons can further transfer their energy by ionizing and exciting atoms along their path. There are two types of ionization: direct and indirect ionization. In direct ionization, charged particles (protons, electrons, heavier ions) have sufficient energy to produce ionization by collision. The initial particle will lose its energy through multiple interactions. In indirect ionization, on the other hand, uncharged particles (photons, neutrons) first interact with matter in order to liberate directly ionizing particles. If the charged particles excite the atoms, there was not enough energy to eject the electron. Instead, the electrons are raised to a higher electron shell with higher energy level.

In proton therapy, proton beams are sent through a patient with the aim of irradiating and killing cancer cells. As the beam traverses through tissue, different interactions can occur. This chapter will briefly describe the fundamental concepts on how charged particles, like protons, interact with matter, as well as how secondary radiation may be produced and further interact with tissue [6].

### **2.1 Charged particle interactions with matter**

There are mainly three ways charged particles interact with matter: inelastic interactions with atomic electrons (a), elastic interaction due to the Coulomb field of atomic nuclei (b) and interaction directly with nuclei, i.e. nuclear interactions (c) [4]. These interactions are illustrated in Figure 6.

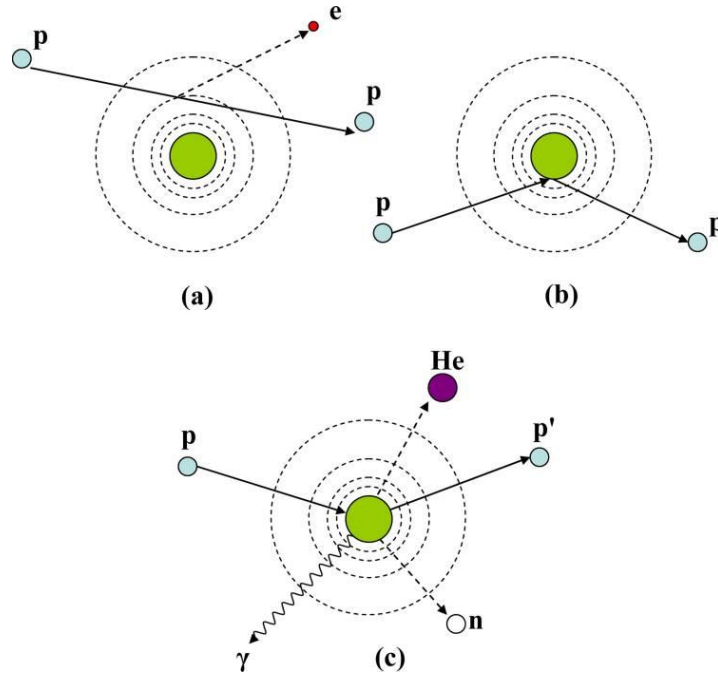


Figure 6: Illustration of the three main charged particle interactions [11].

### 2.1.1 Stopping power

The stopping power describes the energy loss per unit path length when charged particles, such as protons, propagate through matter [4, 11]. Charged particles lose their energy mainly through collisions with atomic electrons of the traversed medium. As a result of these collisions, the electrons can be raised to a higher shell (excitation) or ejected from the atom (ionization). The range of the proton is determined by the inelastic interactions with atomic electrons. The stopping power,  $S$ , can be described by the Bethe-Bloch formula, Equation (2.1) [4, 19]:

$$S = -\frac{dE}{dx} = 2\pi N_A r_e^2 m_e c^2 \rho \frac{Z z^2}{A \beta^2} \left[ \ln \left( \frac{2m_e \gamma^2 v^2 W_{max}}{I^2} \right) - 2\beta^2 - \delta - 2\frac{C}{Z} \right] \quad (2.1)$$

The formula describes the particle energy loss,  $dE$ , per unit path length,  $dx$ , of the traversed matter. Definition of the variables in the Bethe-Bloch equation can be found in Table 1.

Table 1: Definition of the variables in the Bethe-Bloch equation [19].

Symbol	Definition	Value and/or unit
$N_A$	Avogadro's number	$6.022 \cdot 10^{23} \text{ mol}^{-1}$
$r_e$	Classical electron radius	2.818 fm
$m_e$	Electron mass	0.51 MeV/c
$c$	Speed of light in vacuum	$2.998 \cdot 10^8 \text{ m/s}$
$\rho$	Density	$\text{g/cm}^3$
$Z$	Atomic number of absorbing material	
$A$	Atomic mass of absorbing material	
$z$	Charge number of incident particle	
$\beta$	$v/c$ of incident particle	
$v$	Speed of incident particle	m/s
$\gamma$	Lorentz factor $1/(1-\beta)^2$	
$W_{\max}$	Maximum energy transfer in a single collision	
$I$	Mean excitation potential	eV
$\delta$	Density correction	
$C$	Shell correction	

The density and shell correction involve relativistic theory and quantum mechanics, and are only included when dealing with very high or very low proton energies [11]. From the Bethe-Bloch equation one can see that the energy loss is proportional to the square of ion charge and inversely proportional to the square to the particle velocity. This means that the higher the ion charge and the lower the velocity, the higher the energy loss. Thus, when the particle slows down, the energy loss will increase and be at its maximum when the particle has stopped (Bragg peak position).

The mean range is the depth at which half of the protons in the medium have come to rest. Due to statistical variations in energy loss mechanisms from all the interactions charged particles can undergo, protons with the same initial energy may have different range. The

statistical variation is illustrated with a straggling at the end of range, which can be seen in Figure 7. The range straggling can impact the results in the finite dose gradient at the end of range, so in clinical practise, the beam range is usually defined at the distal 80 % of the maximum dose, which coincides with the mean range [4, 11].

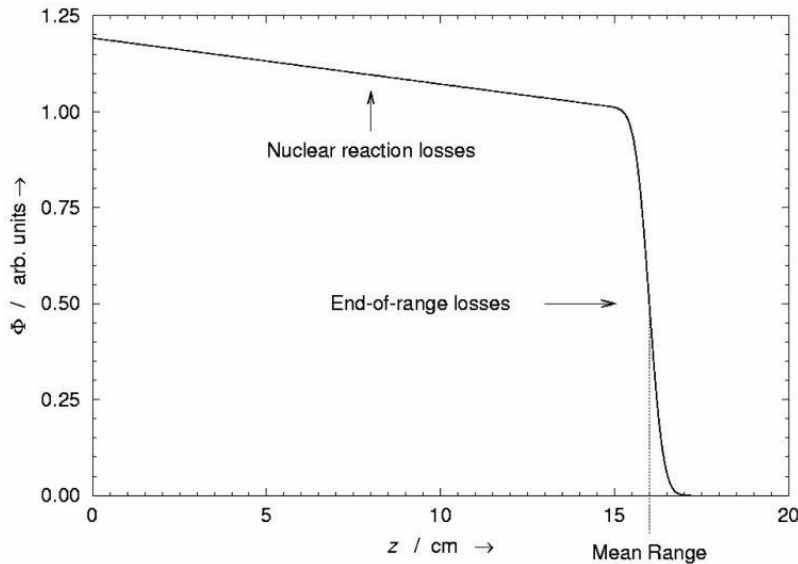


Figure 7: Illustration of a relative fraction of the fluence in a beam of protons as a function of depth  $z$  in water. The figure shows a gradual reduction in fluence from the entrance to near the end due to protons being removed from the incident beam by nuclear reactions. The rapid falloff at the end of the range is caused by protons running out of energy and being absorbed in the medium. The straggling can be seen at the end as a sigmoid shape [11].

### 2.1.2 Coulomb scattering

When protons are sent through a medium, they can experience elastic interaction with the nuclei. This results in deflections due to interactions with the Coulomb field of the atomic nucleus. A Coulomb field is an electrostatic field that arise around electrically charged particles. Protons that pass close to the nuclei are therefore repelled and deflected as a result of the positive charge of the proton and the positive nucleus [17]. Deflection from one single scatter can be negligible, but many deflections together may result in noticeable lateral scattering in the proton beam [4]. This process is known as the Multiple Coulomb Scattering (MCS). Scattering due to interactions with electrons can be ignored as protons are much heavier than electrons [17].

### 2.1.3 Nuclear interactions

There is a possibility that protons interact directly with the nucleus in a “head-on” collision. Interactions that may occur are elastic or non-elastic collision. An elastic collision gives a recoiled nucleus that is left intact, while the primary proton is deflected. For an inelastic interaction the protons need to have sufficient amount of energy in order to enter the nucleus, above a few MeV [4, 17]. Figure 8 illustrates the cross section for non-elastic nuclear reaction from incident protons on the atomic nuclei of O-16, as a function of proton energy. The human body consists of 65 % oxygen, where most are bound to hydrogen, creating water molecules [20]. The cross section is a measure of the probability of the interaction to occur and is measured in units of barn<sup>1</sup>. The figure shows that the threshold for penetrating the Coulomb barrier corresponds to approximately 6 MeV of energy. Protons with higher energies may undergo non-elastic interaction and the probability of the reaction taking place reaches its maximum value at around 20 MeV. Further, the cross section decreases to approximately half of the maximum value at 100 MeV [11]. The nuclear data and graphics in Figure 8 are obtained from the Evaluated Nuclear Data File (ENDF) database [21].

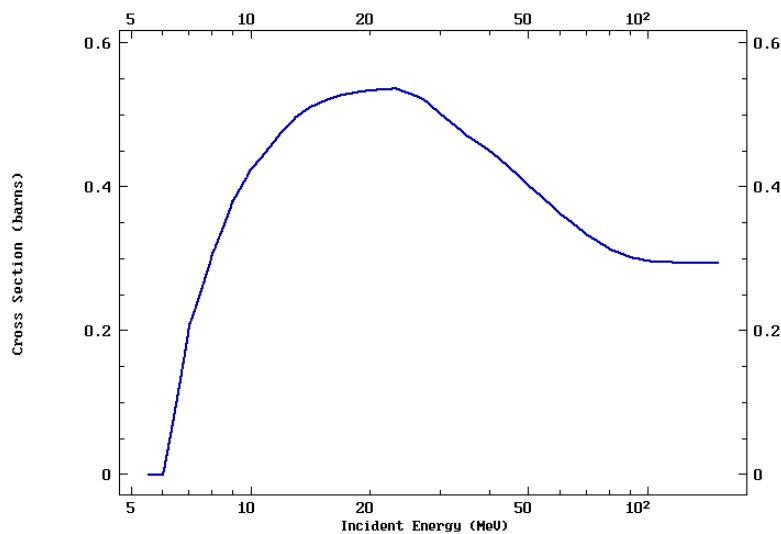


Figure 8: illustration of the cross section for non-elastic nuclear interactions induced by protons on a O-16 nucleus as a function of the incident proton energy [11].

---

<sup>1</sup> 1 barn =  $10^{-28}\text{m}^2$



Non-elastic interactions with protons and nuclei occur along almost the entire beam penetration path, until about 2-3 mm proximal to the Bragg peak. Here the cross section for the reaction falls as the energy of the primary protons declines. In a non-elastic collision, the primary protons are lost from the beam, which reduces the proton fluence as a function of depth. The energy of the proton is absorbed by the nucleus, causing nuclear fragmentation and emission of secondary radiation, i.e. gamma-rays, neutrons, protons and heavier ions [4, 17, 22].

### **Production of secondary charged particles**

In non-elastic collisions between primary protons and target nuclei, secondary charged radiation can be generated. These are typically secondary protons, as well as heavier fragments like alpha particles. Since these secondaries are charged, they will continuously react with the charged nuclei in the traversed matter.

### **Interactions of secondary charged particles**

Charged secondaries can further react with matter through the interaction types described in this chapter, i.e. elastic interaction with atomic electrons and elastic/inelastic reaction with atomic nuclei. Charged particles normally have a shorter range in matter than non-charged particles, as they are continuously slowed down when traversing through matter. The energy loss for charged particles increases with higher ion charge, as presented in the Bethe-Bloch equation. Thus, alpha particles with an ion charge of +2 will have a shorter range and a smaller possibility of escaping the patient, than protons with an ion charge of +1. The range of the charged secondaries increases with higher initial energy [23].

#### **2.1.4 Linear energy transfer**

When a charged particle travels through a medium and deposit energy, not all of the energy is absorbed by the medium. Some of the deposited energy may be carried away by delta electrons, neutrons or prompt gamma-rays, and some by radiative losses or bremsstrahlung. The term linear energy transfer (LET) was implemented to describe this difference. LET is defined as the average energy that is transmitted to the medium by a charged particle traveling a distance in the medium. If a charged particle has high LET it will deposit more energy and thereby inflict more biological damage [24].

There are two approaches to evaluate LET. Restricted linear energy transfer ( $LET_{\Delta}$ ) only focuses on the energy deposited in the matter locally along the particle path, and disregards the kinetic energy transferred to delta electrons with an energy larger than  $\Delta$ . The other approach is unrestricted linear energy transfer ( $LET_{\infty}$ ), where all the energy delivered in the medium is accounted for.  $LET_{\infty}$  equals the stopping power [25].

## 2.2 Gamma-rays in proton therapy

### Production of prompt gamma-rays

Secondary prompt gamma-rays can be produced from non-elastic collisions between a primary proton and a nucleus and will interact differently with the medium compared to charged particles. The energies of prompt gamma-rays produced during proton therapy are mainly in the range between 2-15 MeV [17]. Since gamma-rays have no charge, they can travel longer distances from the point of origin in the tissue and deposit their energy in other organs or escape the patient [23].

### Interactions of prompt gamma-rays

If prompt gamma-rays undergo interactions with the medium, they transfer their energy through indirect ionization. Incident gamma-rays are then either absorbed or scattered, and the energy deposition results in ejection of atomic electrons. The reduction in the number of photons in a beam follows an exponential decay law, i.e. the Beer-Lambert law, and is a function of the linear attenuation coefficient,  $\mu$  [ $\text{cm}^{-1}$ ] and the absorber thickness. This can be written in terms of intensity, resulting in Equation (2.2):

$$I(x) = I_0 e^{-\mu x}, \quad (2.2)$$

where  $I(x)$  is the intensity transmitted through an absorber with thickness  $x$  [cm],  $I_0$  is initial intensity and  $\mu$  is the linear attenuation coefficient describing the probability of interaction per unit path length.

There are three main interactions through which photons deposit energy to matter. The first interaction is photoelectric effect, a phenomenon in which the photon is completely absorbed by the atom, resulting in the ejection of an inner shell electron. The second interaction is the

Compton effect where the incident photon interacts and emits an atomic electron from an outer shell. The photon is not completely absorbed but is scattered with reduced energy. The last interaction is pair production, where photons are able to produce an electron-positron pair if their energy is higher than 1.022 MeV (the energy corresponding to the rest mass of an electron-positron pair). The photon gets absorbed in this process [6].

## 2.3 Neutrons in proton therapy

### Production of secondary neutrons

When a primary proton overcomes the Coulomb barrier of an atomic nuclei, the proton gets absorbed by the nucleus in a nuclear interaction. As a result, secondary particles like neutrons can be ejected. Secondary neutrons are produced within the patient as the protons travel through the patient to reach the tumour. However, production of secondary neutrons may also occur outside the patient when the proton beam is delivered through passive scattering. Passive scattering, unlike pencil beam scanning (PBS), uses mechanical devices to widen and form the beam. Protons from the beam can interact with these mechanical devices and create secondary neutrons outside that may deposit unwanted dose in the patient [4, 11].

Previous performed Monte Carlo (MC) studies using PBS on water phantoms, show that most neutrons, especially neutrons with highest average energy, are produced at shallow depths of the water phantom, where the energy of the primary proton beam is high. With beam energies of 160, 200 and 230 MeV, secondary neutrons with energies up to 200 MeV are generated. However, energies above 10 MeV are predominant for all proton beam energies. The number and energy of the secondary neutrons increase with increasing beam energies, and the majority of the neutrons are produced along the beam path [18, 26].

Neutrons have no charge and may travel longer distances in the medium without being absorbed. If a neutron undergoes an interaction, it is with the atomic nucleus of the medium [27]. The interaction takes place when a neutron and nucleus are close enough and interact due to the attractive nuclear potential at short range. Neutrons can transfer energy to the medium through an intermediate process where the energy is transmitted to a charged particle, such as protons or heavier nuclei [28].

## **Interactions of secondary neutrons**

Secondary neutrons that are produced through nuclear interactions may have a broad variety in energy, depending on the energy of the primary proton. The neutron energy determines the nature of the interaction that may occur if a neutron gets close to a nucleus and reacts. Neutrons with a kinetic energy above a few hundred keV are considered fast neutrons [27, 28]. Fast neutrons will generally lose their energy and slow down through elastic collisions with nuclei. If neutrons undergo elastic scattering the kinetic energy is conserved, but the energy is redistributed. The energy transfer from the neutron to the nucleus is most efficient if the colliding particles have the same mass. For instance, if a fast neutron collides head-on with a hydrogen, all the energy can be transferred to the nucleus. This results in the nucleus being knocked out and becoming a proton that can further ionize and excite the medium. Thus, hydrogenous materials are the most efficient if the aim is to moderate and absorb the neutron [6, 29].

If the energy of the fast neutron is high enough, inelastic scattering with the nuclei can occur [27]. The neutron is then captured by the nucleus and further re-emitted with lower energy. This leaves the nucleus in an excited state. The excess energy is emitted as gamma rays when the nucleus de-excites [28, 29]. When neutrons are slowed down and approach thermal energy (equal kinetic energy distribution as the gas molecules in the environment), the likelihood of them being captured by a nucleus increases [29]. Neutron capture is a type of interaction that can lead to the nucleus emitting protons or gamma rays [28]. Fast neutrons have stronger ability to penetrate through matter, and thereby escape the patient.

## **2.4 Dosimetry and depth dose curves**

### **2.4.1 Absorbed dose**

The radiation damage due to ionizing particles (both charged and uncharged) depends on how much energy is absorbed from the incident radiation. In order to quantify the biological effect caused by ionizing radiation the term absorbed dose was defined. The formula for absorbed dose is presented in Equation (2.3):

$$D = \frac{\Delta E}{\Delta m} , \quad (2.3)$$

where  $\Delta E$  is the absorbed energy and  $\Delta m$  is the unit mass of the tissue [6, 29]. The unit for absorbed dose is gray (Gy) which equals the absorbed energy of one joule per kilogram.

#### 2.4.2 Relative biological effectiveness

Relative Biological Effectiveness (RBE) is used to compare biological effectiveness between different types of radiation. It is defined as the ratio between the photon dose (reference radiation) and the dose from another particle species. In proton therapy, clinical treatment planning is performed using an RBE value of 1.1, i.e. protons are assumed to be 10 % more efficient than photons in delivering the same amount of dose [30, 31]. The unit of RBE is Gy (RBE) which equals 1.1 x dose in Gy [32]. However, it has been shown in in-vivo and in-vitro studies that the RBE value can vary. Experiments show that RBE increases with LET and variable RBE models have been developed, although these models are still not used clinically due to the present uncertainties and disagreements between different RBE models [33].

#### 2.4.3 Spread-out Bragg peak

A proton beam has essential beneficial characteristics when traversing through matter. With a proton beam less healthy tissue will be irradiated and the maximum dose can be deposited within the target volume, compared to conventional radiotherapy. For patient treatments, the Bragg peak is spread out, as the peak corresponding to a single monoenergetic proton beam only covers a narrow fragment of the tumour. By creating multiple proton beams with different energies and intensities, the Bragg peak can be spread over a larger depth, and the entire target volume can be covered uniformly [6, 34].

The protons are accelerated to desired energies through a cyclotron or synchrotron and guided to the gantry for delivery to the patient. With a cyclotron the protons are accelerated by a constant voltage differential and magnetic field that steers the protons in a spiral path, and as they gain energy, they gradually move outwards until they are extracted. For synchrotrons,

both the magnetic field and voltage rate are continuously modulated as the protons are accelerated, in order to keep the protons moving in a fixed loop. Hence, the synchrotrons can produce protons at various energies, whereas cyclotrons produce protons at fixed energies and need beam degrader to alter the energy [34]. When protons at different desired energies are generated, a spread-out Bragg peak (SOBP) can be achieved by passive scattering or pencil beam scanning. Figure 9 illustrates the numerous proton beams with different energies giving rise to the desired SOBP.

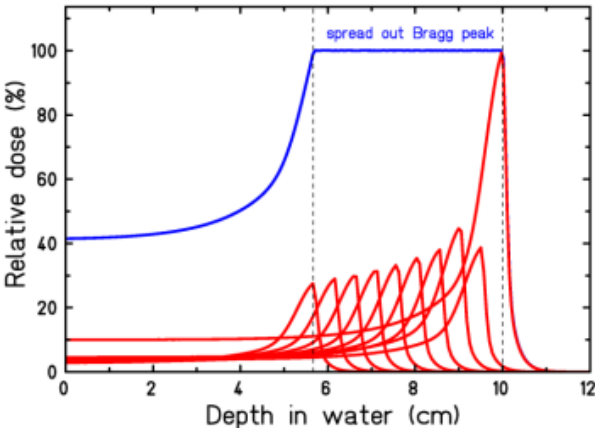


Figure 9: The red curves illustrates the multiple proton beams at different energies, that forms the blue line representing SOBP of the prescribed dose in the planning target volume [35].

## 3. In-vivo range verification in proton therapy

### 3.1 Range uncertainties

Protons are more ideal than traditional X-rays when it comes to sparing healthy tissue surrounding the tumour. However, there are uncertainties when delivering the proton beam to the patient and there are several origins to these uncertainties. The range of the proton beam will depend on the initial proton energy and physical properties of the medium, which is normally calculated from a CT scan [18]. A conversion algorithm is used to establish the proton stopping power from the measurements of CT X-ray attenuation, and this conversion may result in increased uncertainties. Other sources of uncertainties from the CT images can be limitations in spatial resolution, image noise and calibration error [4]. There may also be uncertainties related to patient motion, error in positioning, inter- and intra-fractional organ motion, anatomical changes and uncertainties regarding interfaces between tissues with different density [4, 18].

To take all of these uncertainties into account, a reasonable estimate of the total magnitude has been made and margins are determined to ensure that the treatment goals are accomplished. These treatment margins make the plan more robust towards range uncertainties. Typical range margins when delivering uniform doses are a distance from the target of  $1.5\sigma$  (standard deviation) of expected range distribution. If an organ at risk is located along the beam path, an additional  $2\sigma$  should be added, making it a separation of  $3.5\sigma$  from the target. This is shown in Figure 10. If the organ at risk is closer to the target than  $3.5\sigma$ , this beam direction may not be possible and other beam directions needs to be considered. This may not give the most ideal field arrangements and can lead to more healthy tissue being irradiated in order to spare organs at risk [4].

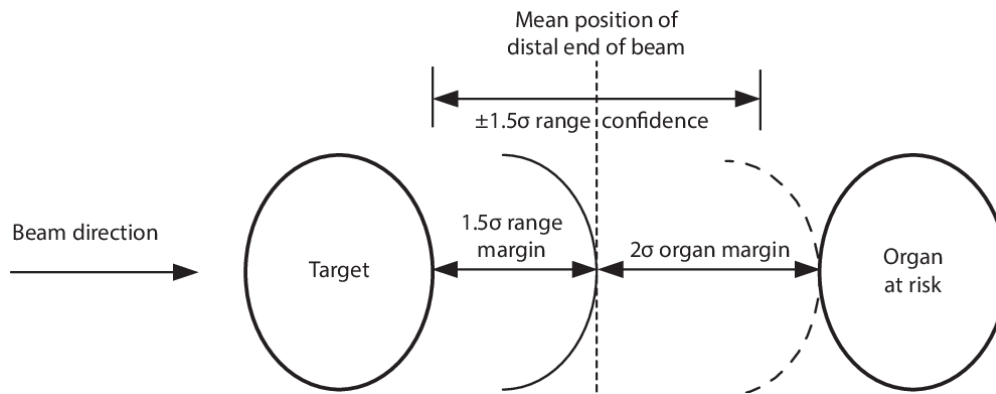


Figure 10: Illustration of the typical range margins for a robust delivering against range uncertainties [4].

A range margin of 3.5 % of the range in water can be used which estimates  $1.5\sigma$  of the range distribution. To take account for errors in patient set up, like patient motion and random error, an additional 1mm is added. For a separation of  $3.5\sigma$  between the target and organ at risk, an estimation of 8 % of the range in water can be applied [4]. For instance, if the beam range in water is 20 cm, the range margin for 3.5 % and 8 % equals 0.7 cm and 1.6 cm respectively. With in-vivo range verification these range margins can be reduced, which is very beneficial in cancer treatments. First of all, reduced range uncertainties allow a reduction of the treatment volume and more healthy tissue being spared. Secondly, reduced range margins can provide the most ideal field directions, especially when organs at risk are close to the target [18, 36].

## 3.2 In-vivo range verification methods

Methods for verifying range in vivo can be divided into two groups: direct and indirect. For direct measurements the proton range is measured directly by dose or fluence measurements, while with indirect measurements the particle range is implied from another signal such as secondary particles produced during proton irradiation [14].

### 3.2.1 Direct methods

Proton radiography (2D) and tomography (3D) uses protons to create anatomical images, instead of conventional X-ray images in CT. High energy protons pass through the patient's body and are detected at the exit of the patient. Proton transmission imaging also provides directly values for stopping power of the tissue, compared to traditional X-ray CT where



measured electron densities need to be converted into stopping power, resulting in increased uncertainties [17, 37]. Proton transmission imaging can therefore be used for both treatment planning and/or in-vivo range verification. However, there are some disadvantages like the fact that MCS can occur, which will give limited spatial resolution. Protons that transverse through matter can undergo multiple deflections with small angles, as a result of interactions with the Coulomb field of nucleus in matter. This results in considerable uncertainties in the predicted proton trajectories through the patient. The spatial resolution can be improved with higher energy protons as higher energetic protons will travel in a straighter line and be less affected by the Coulomb field of nuclei in the medium [17].

### 3.2.2 Indirect methods

When protons traverse matter, nuclear reactions can take place, and a fraction of these reactions may result in gamma-ray emissions. There are two types of techniques where gamma-rays can be used for range verification. The first one is prompt gamma (PG) imaging that exploits the emission of prompt gamma-rays when excited nuclei return to ground state. Nuclei can jump to a higher energy state when protons interact inelastically with the nuclei. These reactions will happen almost the whole path of the proton up to 2-3 mm before Bragg peak [17]. There is therefore a correlation between prompt gamma-ray emission profiles and the proton beam range. The emission of prompt gamma-rays has a time scale smaller than  $10^{-11}$  s and can enable real-time range verification. Most of the gamma-rays escapes the patient and can be detected externally. The detection system needs to meet several requirements in order to be successful for clinical application, such as high detection rate, and accurately correlate of the measured prompt gamma-rays and the proton dose deposition [38].

Another type of gamma radiation used for in-vivo range verification is gamma-rays that originate from positrons emitted from isotopes with residual radioactivity. When a proton passes through matter, some of the protons will undergo nuclear reactions and thereby create isotopes (e.g.  $^{11}\text{C}$ ,  $^{13}\text{N}$  and  $^{15}\text{O}$ ) that decays through  $\beta^+$  decay. The emitted positrons will annihilate with electrons, creating two back-to-back gammas-rays (each with energy of 511 keV) that get detected by a suitable PET camera. With this method range verification can be performed using conventional PET imaging systems. PET imaging can be carried out during the irradiation, so-called in-beam PET (“on line”) or after the treatment (“off line”) [17, 39].

Both PG- and PET imaging have been applied in clinical proton therapy, and the techniques do not result in any additional dose. However, there are challenges and limitations for both methods. PET monitoring for proton therapy is a good approach, that still needs improvement. The PET imaging performance has primarily been offline, due to background radiation and limitations in statistics achievable for in-beam PET. Still, there are also challenges that may occur when performing measurements offline, e.g. rapid signal decrease due to decay and biological washout [18, 39].

For PG imaging, the technique has been seen to be promising for real-time range verification, as the measurements are performed in real-time as prompt gamma-rays are emitted promptly, i.e. during irradiation. PG imaging has also distinct advantages compared to PET, such as a higher count rate at production and lack of biological wash-out. Additionally, the highest nuclear interaction cross section that leads to prompt gamma-ray appears at lower energy than for positron emitters, i.e. the prompt gamma-ray fall-off is closer to the Bragg peak compared to the fall-off for positron emitters [39]. However, with use of collimated detector systems, background neutron radiation and stray gammas becomes an issue as it blurs the location of the distal dose fall-off. There may also be challenges due to statistical uncertainties and sensitivity with detector positioning. With an optimal detection system and fast response, the use of prompt gamma-rays can be advantageous and very accurate for real-time in-vivo range verification [17, 18].

### **3.3 Secondary neutron detection for in-vivo range verification**

Along with gamma-rays and positrons emitters, secondary neutrons are also produced in nuclear interactions between primary protons and nuclei of the irradiated medium. Detection of the created secondary neutrons is a proposed and promising method for real-time monitoring of the primary proton beam range, that yet needs to be further explored [18, 40]. Beneficial aspects of using secondary neutron for range verification is their ability to travel long distance and escape the patient, and secondly, results from the NOVO (NeutrOn detection for real-time range VerificatiOn) project demonstrated a distinct correlation between neutron production yields and the primary proton beam range [18]. However, there can be some

difficulties using secondary neutron signal for proton beam range verification modality, e.g. to find the optimal way of detecting the neutrons and locate the point of creation, the size and placement of the detector and how to account for other secondary particles.

The model for neutron detection used in the NOVO project, included a hydrogen rich organic scintillator for conversion of neutrons to protons (mainly through elastic scattering), followed by two charged particle detectors to determine the position and direction of the recoiling protons. The information can further be used to reconstruct the path and estimate the production depth distribution for the neutrons, and in the end give an estimate of the primary proton beam range. Thus, the produced secondary neutrons are measured indirectly. The concept of the neutron detection model can be seen in Figure 11.

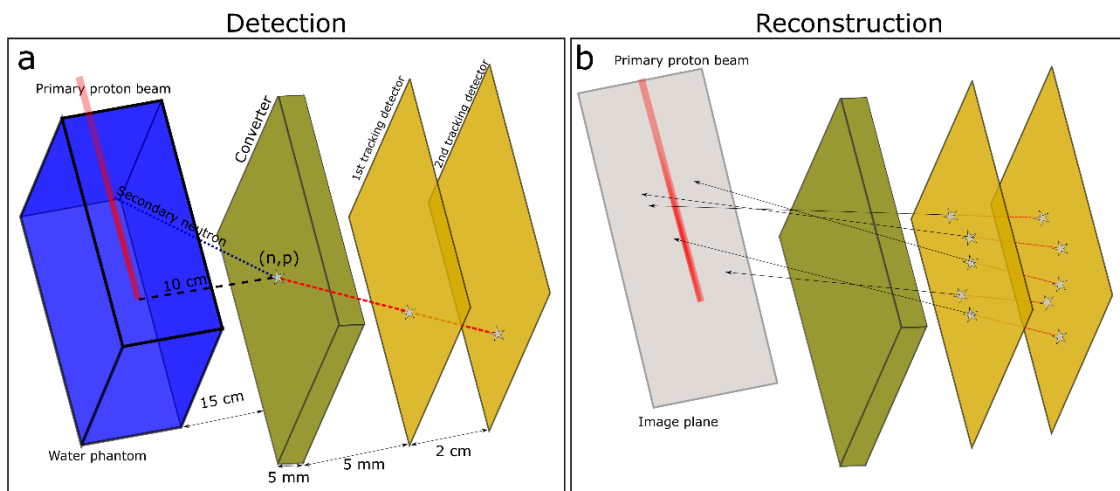


Figure 11: Conceptual design of the model for neutron detection from the NOVO project. **(a)** Secondary neutrons created along the proton beam path may reach the converter and be converted to protons. **(b)** The protons reaching both detectors give potential signal used to trace the origin of the neutron production. The dimensions given in the figure are not to scale [18].

From the NOVO results, the neutron production was relatively stable in the entrance region, followed by a steep fall-off proximal to the Bragg peak (see Figure 12), illustrating the correlation between proton beam range and production of secondary neutrons. The production rate and energy distribution of secondary neutrons showed strong dependence of the primary proton beam energy. The study also observed that secondary neutrons of higher energies were produced at the entrance region, and most neutrons were generated close to the traversing

beam. Hence, finding the optimal size and positioning of the detector is essential as it may have an effect on the distribution of the secondary neutrons that are detected [18].

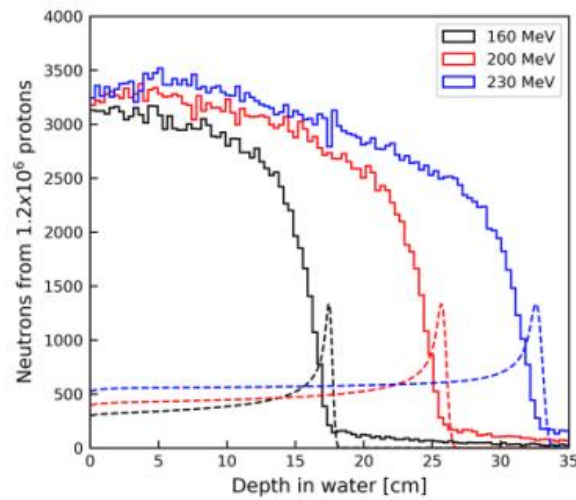


Figure 12: Neutron production in a water phantom as a function of depth for 160, 200 and 230 MeV. Relative depth dose curves are shown with dashed lines. The figure illustrates the correlation between produced secondary neutrons and the proton beam range, as the production decreases steeply proximal to the Bragg peak [18].

Although detection of secondary neutrons seems promising for range verification, there are still many questions remaining, such as secondary radiations significance on the neutron detection. Secondary particles, like large angle scattered protons and prompt gamma-rays, may interfere and have an impact on the neutron measurements. This concern will be investigated in this thesis.

## 4. Materials and methods

In this thesis Monte Carlo (MC) simulations have been performed using FLUKA (version 2011.2x.7) [41, 42], a tool used for calculations of particle transport and their interaction with matter. With MC simulations, an algorithmic generation process is performed to estimate stochastic results by using repeated random sampling and statistical analysis, based on probability distributions [43]. FLUKA covers a wide range of applications such as dosimetry, detector design, radiation protection, radiotherapy, along with many other applications [44]. MC simulations have been used to collect detailed information about secondary particles generated from the primary proton beam. This included secondary neutrons for the purpose of range verification measurements during treatment, along with secondary radiation that may interfere with the neutron-based measurements. The MC simulations involved a simple proton beam incident on a water phantom as well as simulations of a clinical proton treatment plan.

FLUKA MC simulations are based upon so-called input files which specify properties of the simulations, including geometry, beam properties, material definitions, physics settings and scoring options. Input files for the water phantom and the patient plan were adopted from previous projects files [18] and modified for the purpose and objectives of this thesis. The modified FLUKA input file for the water phantom can be seen in Appendix A.

### 4.1 Water phantom simulations

#### 4.1.1 FLUKA input

A setup with a water phantom ( $35 \times 20 \times 20 \text{ cm}^3$ ) irradiated with monoenergetic proton beams of 100, 160, 200 and 230 MeV were simulated. The proton pencil beams had no momentum spread. The neutron detection concept from the NOVO project was used in this thesis, involving a 5 mm thick converter of EJ-309 scintillator material placed 15 cm from the water phantom, followed by two detection planes, mimicking position sensitive charged particle detectors. EJ-309 is an organic scintillator material rich in hydrogen with a H:C ratio of 1.25 and a density of  $0.959 \text{ g/cm}^3$ . The size of the converter and the detectors were  $20 \times 20 \text{ cm}^2$ , and the media around the design was defined as air in the simulations. The relevant simulation geometry is shown in Figure 13.

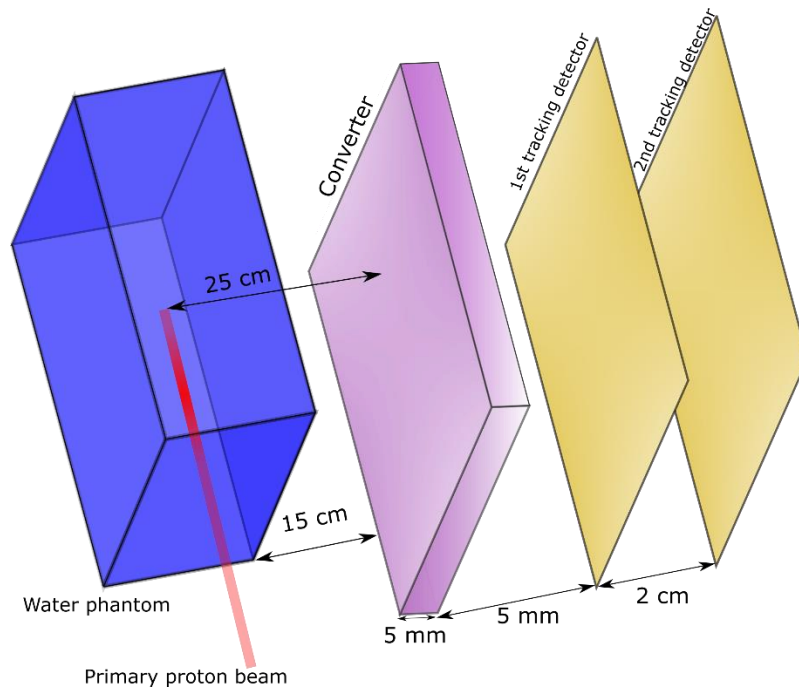


Figure 13: The conceptual design for the water phantom that was implemented in MC simulations. The dimensions setup is similar to the NOVO project, but with thicker water phantom and greater distance from the phantom to the converter.

In the FLUKA input file, proton beams with the different energies were inserted with a Gaussian profile of 1 cm full width at half maximum (FWHM). The number of primary protons sent through the water phantom was specified to  $1 \times 10^8$  for each of the energies, and 12 independent simulations were simulated at the same time. This was executed with two cycles; thus, the MC simulation were performed with  $2.4 \times 10^9$  primary proton histories <sup>1</sup> for each energy.

FLUKA provides a set of default setting, making it simpler when choosing the best settings for a specific simulation case. The defaults for the water simulations were set to precision in the input. Precision provide detailed production data for simulated particles [45]. Most relevant for this work is the transport of low energy neutrons, down to thermal energies

---

<sup>1</sup> A particle history means the trajectory of one primary proton and its potential secondary particles.

(threshold for high energy neutron is 20 MeV), and a general particle threshold of 100 keV for all particles (except for neutrons).

Two physics cards were implemented in the input file, one for coalescence and one for evaporation. Heavy particle evaporation and coalescence should be activated, as these physics cards give the best available particle calculation and results for residual nuclei production and/or fragment production from ion beams. The iontrans card was also included where the selected type of transport was heavy ion, which include full transportation of all light and heavy ions. All these cards gives a more precise estimation for the produced secondaries [45]. Table 2 presents an overview of the FLUKA input settings for the water phantom simulations.

Table 2: FLUKA input settings for the water phantom.

<b>Proton beam energy</b>	100 MeV, 160 MeV, 200 MeV and 230 MeV
<b>Number of primary histories</b>	$2.4 \times 10^9$
<b>Default</b>	PRECISIO
<b>Physics processes</b>	COALESCE, on EVAPORAT, new evap with heavy frag
<b>Transport cut</b>	IONTRANS, heavyion
<b>Scoring card</b>	<b>USRBIN</b> (dose and fluence) <b>USRBDX</b> (energy converter boundary) <b>USRDUMP</b> complete, all (activates calls to the user routine BXDRAW)

For each proton beam energy, the converter and the detectors were aligned with the Bragg peak depth at the lateral distance of  $x$  (see Figure 14). In order to do so, the position of the Bragg peak for each energy was found from depth dose curves results (Figure 19), and the distance the converter and the detector needed to be moved for each energy was calculated

and implemented in input file. When selecting a proton beam energy, the converter and detector will thereby move according to the Bragg peak depth for the given beam energy.

Figure 14 demonstrates how the geometry was visualized in FLUKA in the xz-plane. The different rooms were filled with air with the intention of separating the different components in the neutron detector design.

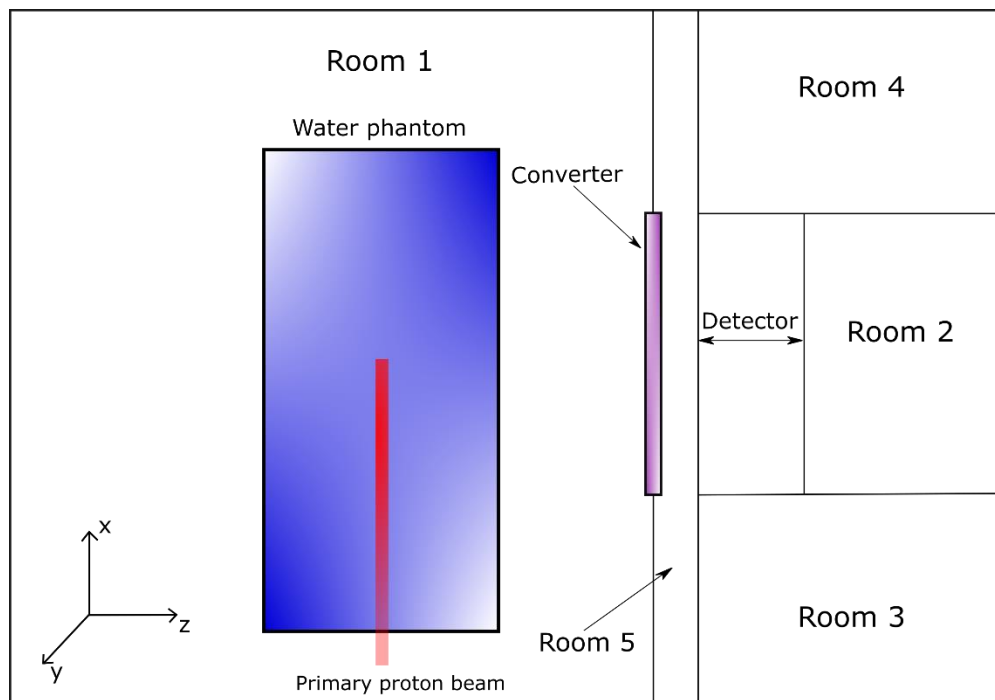


Figure 14: Illustration of the geometry used in the MC simulations for the water phantom.

#### 4.1.2 Scoring options

The FLUKA software has numerous estimators that can be activated and used in the simulations. These estimators are normally referred to as “scoring” options. The scoring options used in this thesis were USRBIN and USRBDX. In addition, custom scoring file for particle tracking was supplemented for the simulation.

#### **USRBIN**

The USRBIN function in FLUKA scores the spatial distributions of various quantities, independent of the geometry [45]. Quantities scored in this thesis were absorbed dose and the fluence of protons, gamma-rays, neutrons and alpha particles. The USRBIN scoring card for



proton fluence included both primary and secondary protons. Figure 15 shows an example of a USRBIN scoring card for neutron fluence. USRBIN cards for particle fluence and dose were added in the input file, with suitable geometry borders and an appropriate number of spatial bins<sup>1</sup>. For graphical presentation of the simulated dose results, the dose was normalized to relative dose with 100 % dose in the Bragg peak. The USRBIN card for one-dimensional dose had a selected geometry border of 35 cm in depth (x) direction and 700 bins. This gave 20 bins per centimetre and provided consequently a very good resolution. The chosen number of bins and geometry borders for both the two-dimensional dose and fluence resulted in a bin size of 2.5 mm. The number of bins were chosen after a couple of test runs in order to find a suitable number that would give good resolution when plotting.



Figure 15: USRBIN scoring card for neutron.

## USRBDX

USRBDX is a function that estimates the fluence or current for a given particle crossing a boundary between two geometry regions [45]. In this thesis the boundary between room 1 (air) and the converter has been examined (see Figure 14). The quantities scored in this boundary were the fluence and energy distributions for protons, gamma-rays, neutrons and alpha particles. The USRBDX scoring card for proton includes both primary and secondary protons. So-called one-way scoring was studied, which accounted for particles going into the converter from the room 1 region [45].

A converter area of 400 cm<sup>2</sup> was implemented in USRBDX card, in addition to a suitable number of energy bins and fitting maximum kinetic energy for the scoring. Figure 16 presents an example of a USRBDX scoring card for neutron. The maximum kinetic energy for scoring was set to 250 MeV for all particles, except for gamma-rays where the maximum energy was set to 25 MeV. With a maximum energy of 250 MeV, the energy distribution for all the

---

<sup>1</sup> Bins are equally divided intervals used to arrange data.

secondaries are included, as the highest applied proton beam energy was 230 MeV. After running initial test runs, it was evident that prompt gamma-rays generated energies below 25 MeV at the converter. The maximum kinetic energy was for that reason set to 25 MeV for photons. The number of energy bins were set to 300 for neutrons and 250 for the other particles.

For neutrons, FLUKA has an own cross section library for low-energy neutrons (energy lower than 20 MeV), that includes an expansion of 260 neutron energy groups. So, when scoring the neutron fluence, the requested energy bin overlaps with the low energy neutron groups, and the bin boundaries are forced to coincide with the group boundaries. No bin can be smaller than the corresponding group, hence the number of bins chosen was 300. The program uses the energy limits and the number of bins to estimate the desired bin width [45].

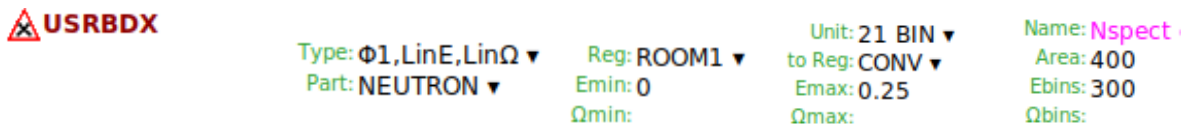


Figure 16: USRBDX scoring card for neutron. The  $E_{\max}$  unit is in GeV and the area unit is  $\text{cm}^2$ .

### Custom scoring file for particle tracking

In addition to the fluence and energy (at the converter boundary), the production coordinates, initial kinetic energy and angular distribution for the secondaries were studied. To determine these quantities, a custom tracking code [18] was modified to include all the selected secondary particles for this thesis. The code (Appendix B.1) wrote out the position, the kinetic energy and the recorded emission angles for the secondaries created in the water phantom, if an inelastic interaction occurred. The quantities were written to files for every hundred hits (to limit the output file size), except for secondary alphas where every hit was written due to the low production rate leading to poorer statistics for alpha particles. Additionally, the code was programmed to follow the secondaries and score the desired quantities at the crossing region between room 1 and the converter. The scoring file was compiled in FLUKA before simulation.

### 4.1.3 Simulation and graphical representation

After applying necessary information in FLUKA, including the different scoring options and compiled file, the final simulation with  $2.4 \times 10^9$  primary proton histories was executed for each primary proton beam energy. The total CPU (Central Processing Unit) time used to follow the primary protons in one cycle was approximately 25 hours for 100 MeV proton beam energy, and up to 73 hours for 230 MeV. In order to visualize the data files generated in the MC simulations, the plot option in FLUKA was used for 2D USRBIN scoring, while the programs Matplotlib and python (version 2.7) were used to illustrate 1D USRBIN and USRBDX scoring, as well as data generated from the compiled files. The numerous python scripts created were based on scripts found on Matplotlib website <sup>1</sup> and altered for this thesis.

### 4.1.4 Simulation with different water phantom thickness

All patients have different size and shapes, and a tumour can be localized in various places in the body. For that reason, it may be interesting to see how different quantities like the particle fluence and energy distribution change as a function of thickness. In order to do so, the geometry for the water phantom was changed symmetrically in y- and z-direction and the new dimensions simulated were  $10 \times 10 \text{ cm}^2$  and  $30 \times 30 \text{ cm}^2$ . The simulations were examined for primary proton beam energies at 160 MeV. The number of primary histories was set to  $1.2 \times 10^9$ .

### 4.1.5 Uncertainties

The statistical precision of the MC results depends on the number of histories,  $N$ , as the statistical uncertainty is proportional to  $1/\sqrt{N}$  [46]. Therefore, simulations with higher number of primary particles will reduce the statistical uncertainties of the MC estimates. The statistical uncertainties can also vary with beam properties and the geometry used in the simulation, e.g. longer distance between the water phantom and converter requires a higher number of primary histories. Thus, a suitable number of primary histories to achieve reasonable low uncertainties needs to be evaluated for each scenario. From the files generated with the USRBIN and

---

<sup>1</sup> <https://matplotlib.org/>

USRBDX cards, a column containing the uncertainty for the quantity scored, expressed in percentage, was included and used to control appropriate uncertainty numbers for the MC simulations. These uncertainties are calculated from build-in scorings in FLUKA. The FLUKA software can also experience uncertainties in the simulations, which was seen in the results and will be discussed later in this thesis.

In order to find the uncertainties for the production rate and particle rate at the converter, obtained from the tracking files, calculations with standard deviation was performed. The formula for standard deviation ( $\sigma$ ) can be seen in Equation (4.1) [47]:

$$\sigma = \sqrt{\frac{\sum_{i=1}^n (x_i - \bar{x})^2}{n-1}}, \quad (4.1)$$

where  $x_i$  is the number of particles per primary proton from each individual simulation, ( $\bar{x}$ ) is the mean value and  $n$  is the number of individual simulations (e.g. 24 simulations for the original water phantom size).

## 4.2 Patient simulations

### 4.2.1 FLUKA input

The patient data used in this thesis was from a proton treatment plan for prostate cancer. The treatment plan consisted of two treatment fields, both contributing to the prescribed dose to the prostate PTV of 67.5 Gy(RBE), while each field separately irradiating lymph nodes on their respective sides with 55 Gy(RBE). This thesis only examined treatment field 1. The patient data was provided as DICOM (Digital Imaging and Communications in Medicine) <sup>1</sup> files. Information from the DICOM files about the treatment plan was imported into FLUKA. In order to do so, a python script (sort\_dicoms.py) created by Lars Fredrik Fjæra [48] was used to extract information from the DICOM files and set up a FLUKA simulation

---

<sup>1</sup> Medical images saved in DICOM format, e.g. CT scans.

environment. The purpose of this script was to import the DICOM files, identify the type of each file (image, plan, structure, dose), and create FLUKA input files [48].

The python script provided two so-called user-routines (in fortran code, which is the language used in FLUKA) which were compiled in FLUKA: The source user-routine (source.f) for the treatment field was used to sample primary particle information from the treatments field (Beam.dat), that are too complicated to describe with input cards alone [45]. The other user-routine (fluscw\_IFT.f) was implemented for the purpose of plotting the 2D dose distribution with the DICOM files.

An additional python script (set\_HU.py) from Fjæra was performed to set vacuum in the regions outside the patient, which saves computation time. From these images, a voxelized patient geometry was generated in FLUKA and a so-called voxel file was created and applied in the FLUKA input. CT numbers of the images were also converted into materials with correlating density, and each voxel was assigned a type of tissue material, which was implemented in FLUKA. The workflow of implementing necessary information into FLUKA before simulation can be seen in Figure 17.

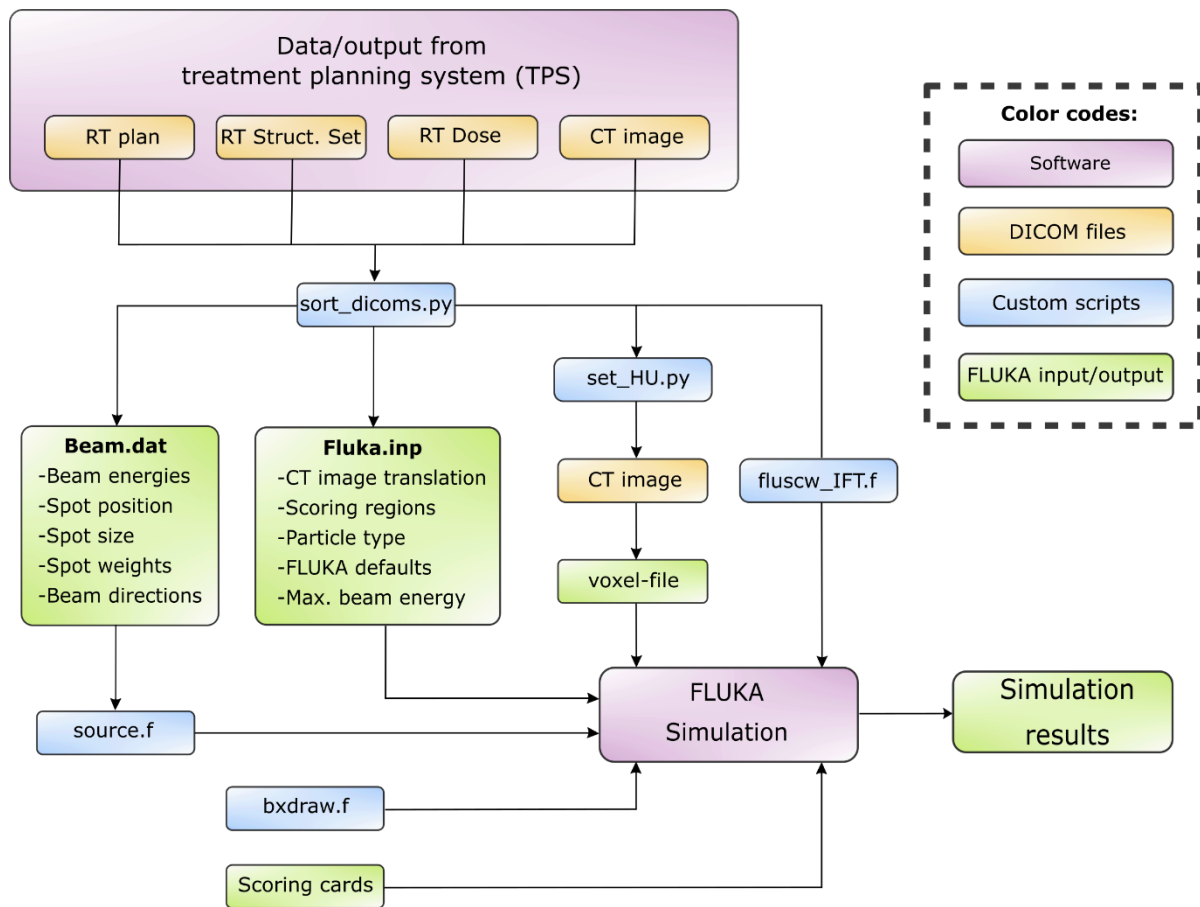


Figure 17: Workflow for the process of assembling the information from the TPS and implementing it to FLUKA. The flowchart also includes the process of implementing the tracking code (`bxdraw.f`) and scoring cards (USRBIN and USRBDX).

The proton beam energy in the simulated field had primary proton beam energies ranging from 93 MeV to 197 MeV. The geometry around the patient was created, similar to the geometry for the water phantom simulations. The relevant simulation geometry for the patient is shown in Figure 18. The size of the converter was set to  $20 \times 20 \times 0.5 \text{ cm}^3$  with EJ-309 as the material. The converter and detector were aligned with the centre of SOBP. The total number of primary histories were  $1.2 \times 10^9$ . The distance between the voxel cage and the converter was 5 mm, and the distance from the patient structure and the converter was approximately 14 cm. Figure 19 illustrates how the geometry was visualized in the xy-plane in FLUKA.

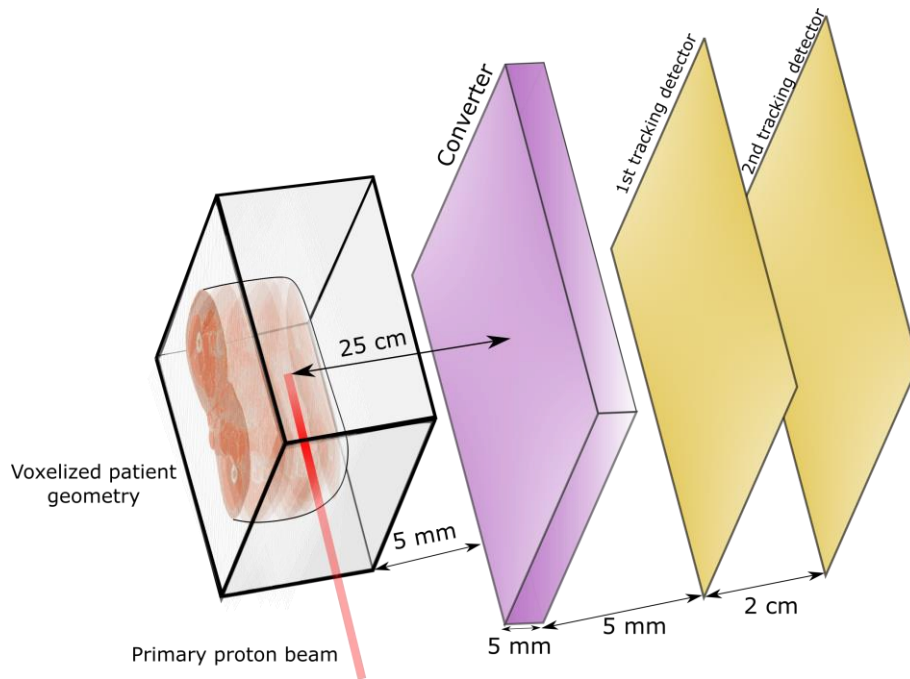


Figure 18: Design of the set-up for the patient simulation geometry. The dimensions given in the figure are not to scale. The box around the patient is so-called voxel cage. Other components/geometry must be placed outside this box.

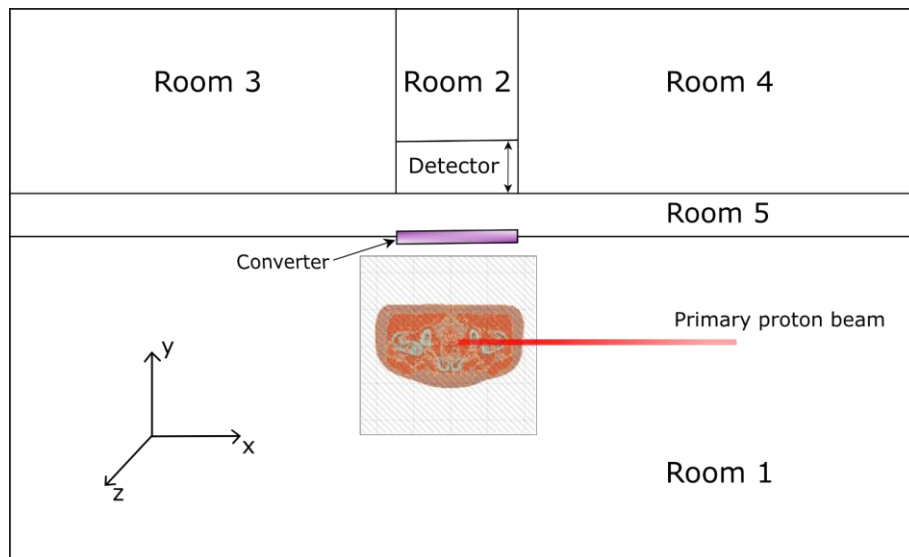


Figure 19: Illustration of the geometry for the patient simulation. The figure shows a section of the patient in the transverse plane.

The FLUKA input setting can be found in Table 3. Similar to the water phantom, the default for the patient simulations was set to precision, providing detailed production data for the simulated particles. The two physics cards for coalescence and evaporation were also included in the FLUKA input, along with iontrans card. These input cards had equal settings as used in the water phantom.

Table 3: FLUKA input settings for the patient simulation.

<b>Proton beam energy</b>	93-197 MeV
<b>Number of primary histories</b>	$1.2 \times 10^9$
<b>Default</b>	PRECISIO
<b>Physics processes</b>	COALESCE, on EVAPORAT, new evap with heavy frag
<b>Transport cut</b>	IONTRANS, heavyion
<b>Scoring card</b>	<b>USRBIN</b> (dose/all part and fluence) <b>USRBDX</b> (energy converter boundary) <b>USRDUMP</b> complete, all (activates calls to the user routine BXDRAW) <b>USERWEIG</b> FLUSCW+ (needed for dose scoring)

#### 4.2.2 Data analysis and visualization

The quantities scored were the same as for the water phantom. The fluence for the different particles was scored with USRBIN cards and were given a bin size of 2.5 mm, equivalent to the water phantom. The USRBDX cards scored the fluence and energy distribution for the particles crossing the converter boundary. The number of energy bins in the USRBDX cards



was also set equal to the water phantom simulations and the converter area of 400 cm<sup>2</sup> was applied to the USRBDX scoring cards. A modified tracking code for this patient case was compiled in FLUKA, which generated files with information used to plot angular distribution in the patient and at the converter, as well as the production and energy distribution in the patient. An additional USRBIN card was implemented in the input file, in order to plot the 2D dose distribution with the DICOM files.

With all the necessary information applied in FLUKA, the patient simulation was executed. The total CPU time for the patient simulation was around 105 hours. For graphical presentation of the data, the 2D fluence plots were generated through the FLUKA plotting option and all the 1D plots were created with python scripts and Matplotlib. The 2D dose distribution was plotted with python scripts created by Fjæra [48]. Two python scripts were carried out, one for converting the FLUKA simulation into DICOM files, followed by one to plot the final dose distribution.

In order to mark the SOBP area in the plots, two simulations with  $2 \times 10^6$  primary histories and a USRBIN dose scoring card were executed for the minimum and maximum proton beam energy. This gave the location of the most proximal and distal Bragg peaks in the SOBP. The depth dose curves for these two energies are presented in Figure C-1 and Figure C-2 in Appendix C. The methods for evaluating and finding the statistical uncertainties in the simulations were similar as for the water phantom.

## 5. Results

### 5.1 Water phantom simulations

#### 5.1.1 Dose distribution

The depth dose curve for all the monoenergetic proton beams simulated in this work are illustrated in Figure 20. For each proton beam energy, the relative dose increased with depth until the protons stopped. This resulted in the characteristic Bragg peak where the relative dose was 100 %, followed by a sharp fall distal to the peak. The Bragg peak depth for the different beam energies can be seen in Table 4. The small bin sizes (1 mm step) gave negligible uncertainties in the Bragg peak positions.

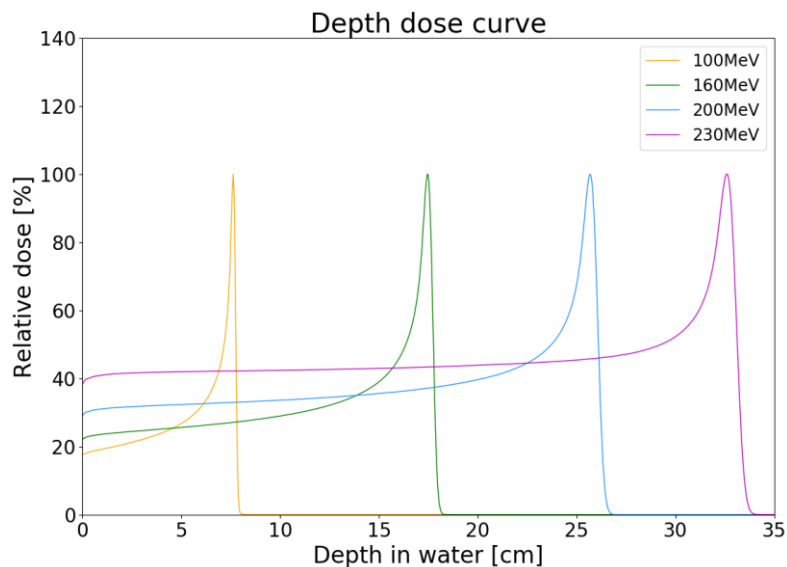


Figure 20: The depth dose curve for different monoenergetic proton beam energies, illustrating the characteristic Bragg peak for each energy. The scoring area was confined to  $2 \times 2 \text{ cm}^2$  in the transverse plane.

Table 4: Table of the Bragg peak depths for the different primary proton beam energies.

	100 MeV	160 MeV	200 MeV	230 MeV
<b>Bragg peak</b>				
<b>depth [cm]</b>	7.6	17.5	25.7	32.6

Figure 21 illustrates two-dimensional plots of the dose distribution in the water phantom for different proton beam energies. The absorbed dose distribution as a function of depth and the lateral spread can be seen in the figure, both increasing with higher proton beam energy. The relative dose level shown is from 0.1 % to maximum (100 %).

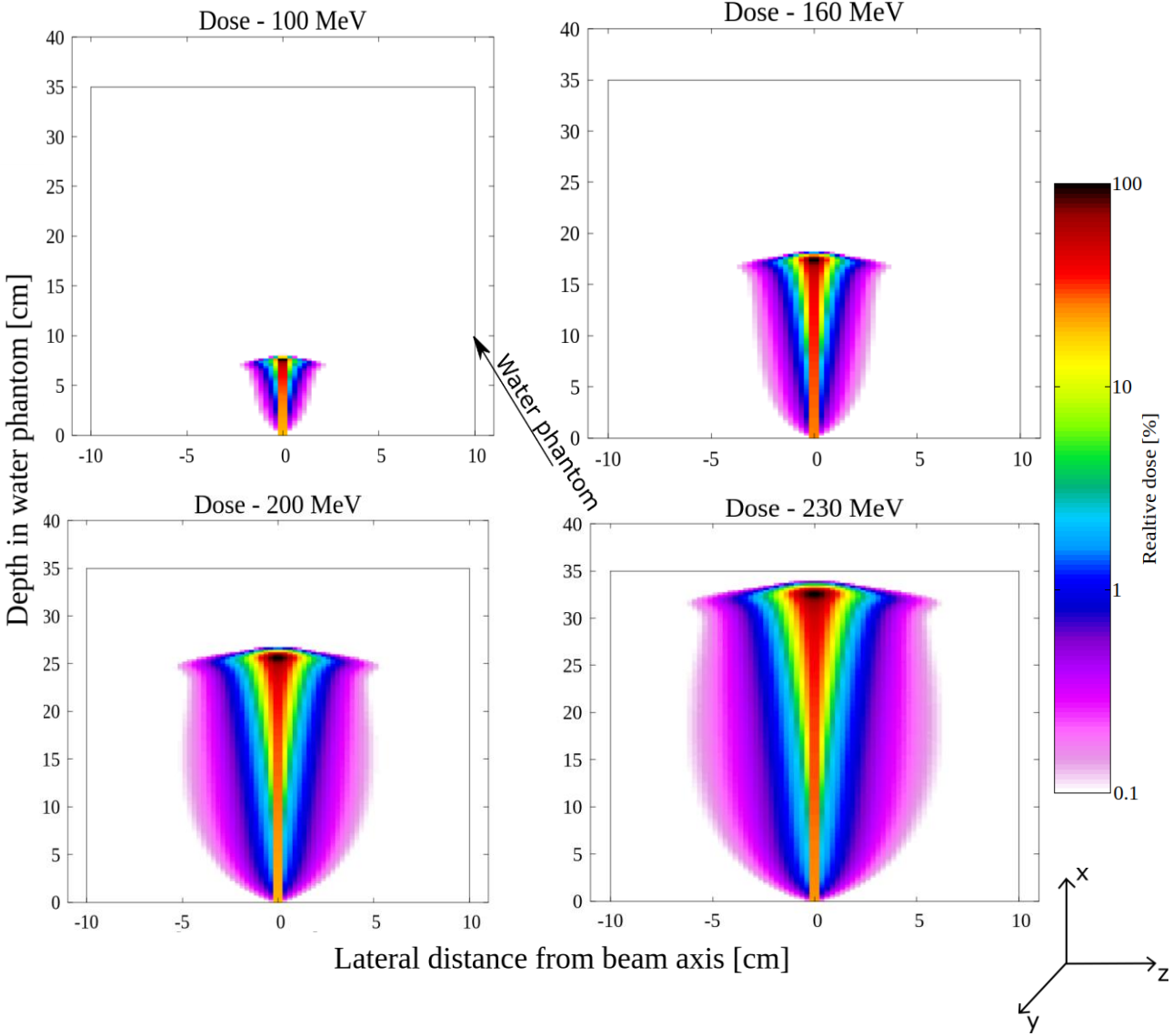


Figure 21: The figure illustrates the 2D dose distribution in the water phantom for different proton beam energies. The colour map is logarithmically scaled and illustrates relative dose levels with 100 % dose in Bragg peak. The dose distribution was narrowed close to the beam in y-direction (1 cm). Geometric sketch of the water phantom is shown in the figure.

### 5.1.2 Particle production in the water phantom

The production distribution as a function of depth for the produced secondaries, obtained from the tracking code, can be seen in Figure 22. Figure 22a shows the produced secondary protons, illustrating a high production of protons at the beginning, followed by a steady decrease for all beam energies, except for 100 MeV. For 100 MeV protons, the secondary proton production was relatively stable in the entrance region. The number of secondary protons peaked right before the Bragg peak for all beam energies, followed by a rapid decrease. The production for prompt gamma-rays can be seen in Figure 22b, showing a rapid growth in the number of prompt gamma-rays up until the Bragg peak, followed by a steep decline.

The secondary neutron production was relatively stable in the entrance region before it rapidly declined proximal to the Bragg peak. This trend was seen for all beam energies, except for 100 MeV, where neutron production decreased instantly. Figure 22d illustrates the production distribution for secondary alpha particles produced, showing a steady growth in number of alpha particles from the entrance to its maximum, pursued by a fast decline proximal to the Bragg peak. Similar to the neutrons, the beam energy of 100 MeV was an exception as the number of alpha particles decreased immediately in the entrance region.

In Figure 22e, the production distribution for all the examined secondary particles are presented for primary proton beam energy of 160 MeV. Secondary protons were observed as the most abundant secondary radiation species from the entrance of the water phantom to the Bragg peak depth, followed by a drop below the prompt gamma-ray and neutron production rate. Secondary neutrons had mainly the second highest production number in the entire water phantom depth, except around the area prior to the Bragg peak, where prompt gamma-rays had a higher production. Distal to the Bragg peak, secondary neutrons had the highest production. Alpha particles had the lowest production number of all the secondaries.

## Production distribution in the water phantom

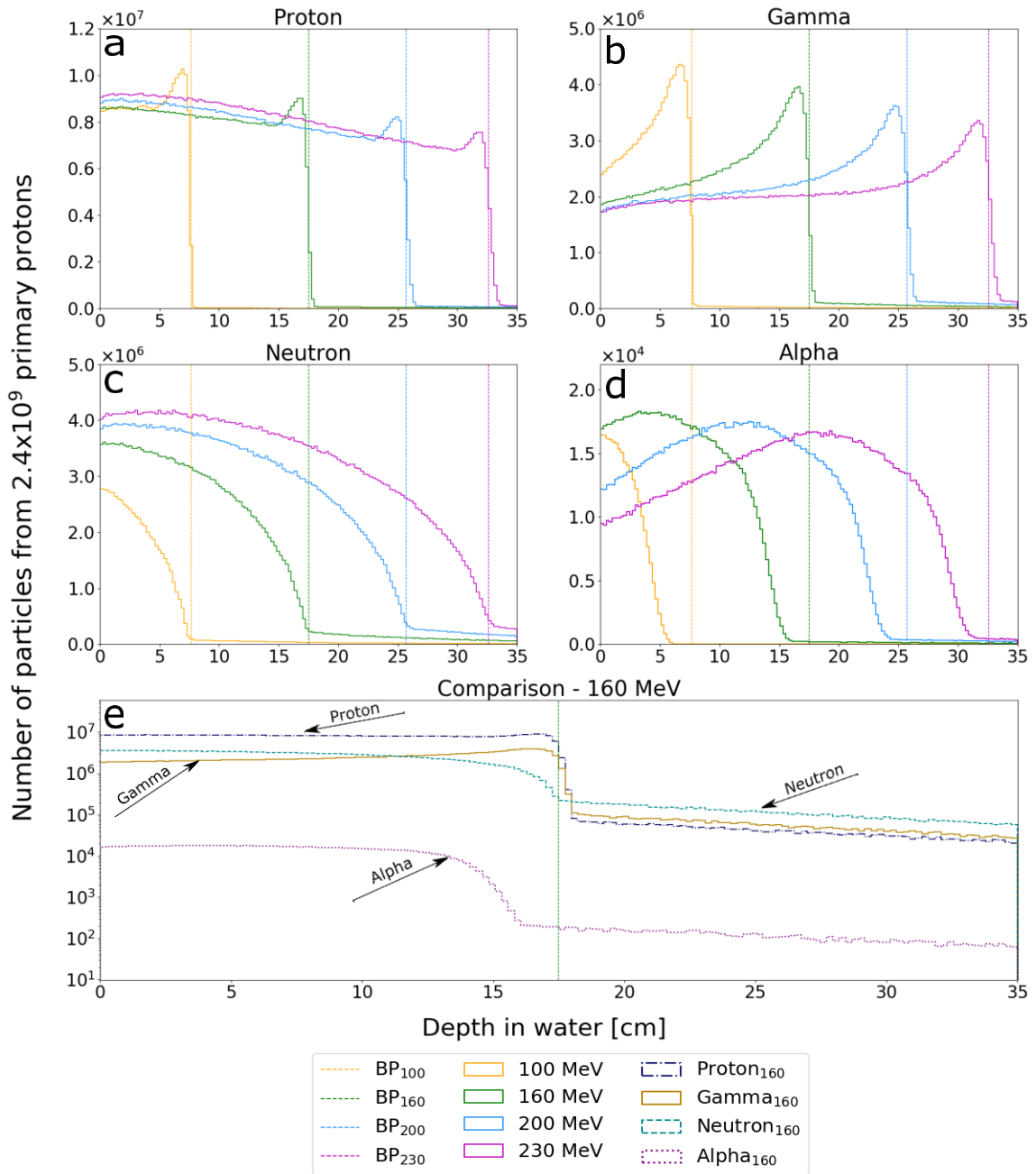


Figure 22: Illustration of the production distributions as a function of water phantom depth for the secondary particles created. The figure shows the particle production (solid histogram) for secondary protons (a), prompt gamma-rays (b), neutrons (c) and alpha particles (d), and the position of the Bragg peak depth for each beam energy (vertical dashed line). A comparison of the production distributions of the secondaries for primary protons of 160 MeV is presented in the figure (e) with a logarithmic ordinate axis.

Distribution of the initial kinetic energy for the secondaries created in the water phantom can be seen in Figure 23. The energy spectra were dominated by particles energies above 1-10 MeV for both secondary protons (Figure 23a) and secondary neutrons (Figure 23c), for all primary beam energies. A peak around 20 MeV in the neutron energy spectra can be observed, representing discrepancies between the models for low energy and high energy (> 20 MeV) neutron in FLUKA. This illustrates some of the uncertainties present in the MC simulation of neutron production from proton beams.

For prompt gamma-rays, the energy spectra showed numerous peaks, and were dominated by energies of 1-10 MeV (Figure 23b). The dominant prompt gamma-ray energies were 4.4 MeV and 5.3 MeV. The 4.4 MeV and 5.3 MeV PG emission energies originate from de-excitation of  $^{16}\text{O}$  nuclei, originating from proton-induced nuclear interaction in the water phantom [4, 49]. Secondary alpha particles were dominated by energies above 10 MeV for all proton beam energies (Figure 23d). The maximum particle energy increased with increasing proton beam energy for all secondary particles, except for prompt gamma-rays, where the energy spectra had fixed energy peaks. This is because prompt gamma radiation is emitted from excited nuclei after proton-induced nuclear reactions, that subsequently decays to the lower state. Thus, the prompt gamma-ray energy reflects the energy difference between the excited and the ground state of the nuclei.

### Energy distribution in the water phantom

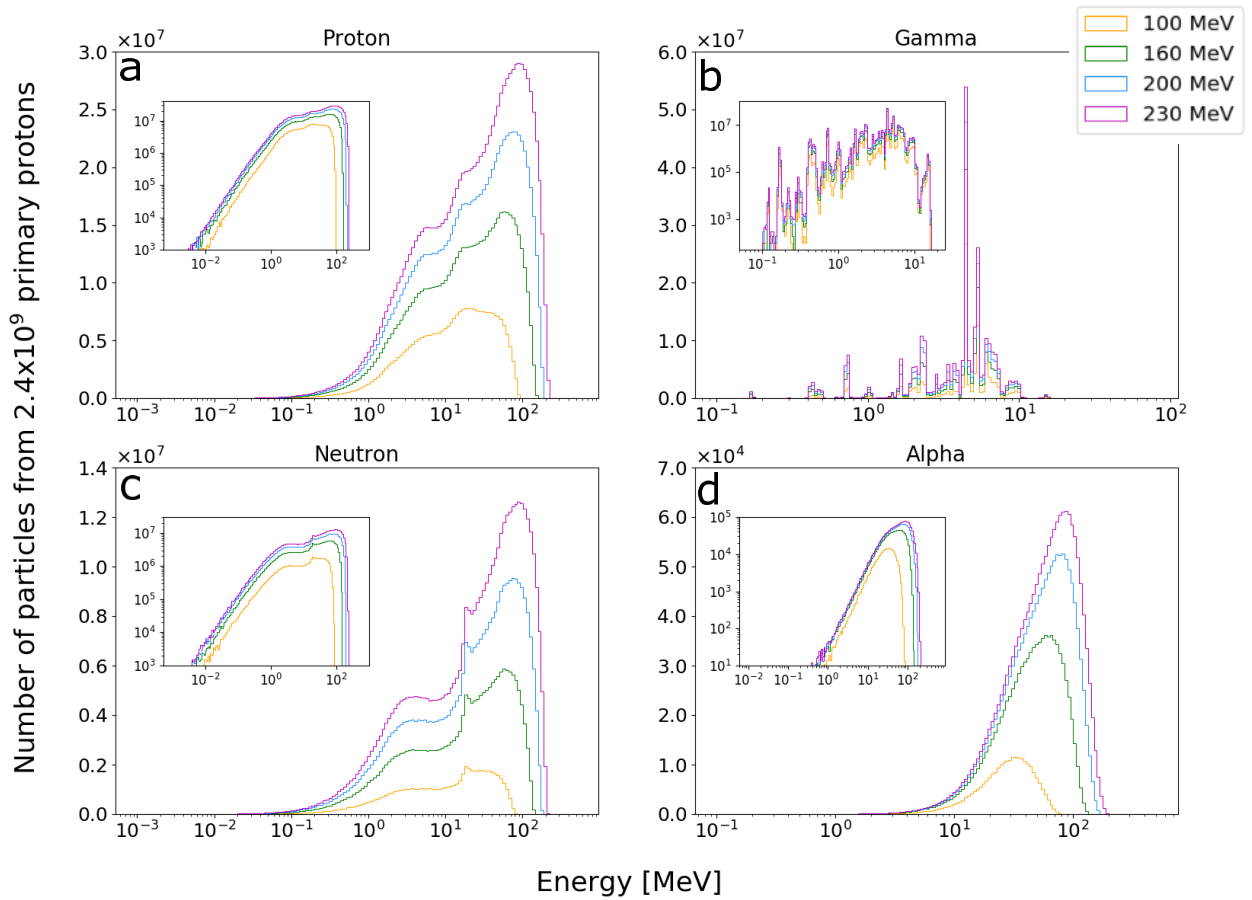


Figure 23: The distribution of the initial kinetic energy for the secondaries created in the water phantom from the different proton beam energies. The energy spectra are shown with logarithmic bins and linear ordinate axis in the main plots for all particles. The inlay plot shows a logarithmic ordinate axis.

In Figure 24, the angular distribution for the secondaries created in the water phantom can be seen. Secondary protons (a), neutrons (c) and alpha particles (d) were observed to be predominantly emitted in the forward direction, i.e. along the direction of the incident primary proton beam. The angular distributions for the directions perpendicular to the proton beam were symmetric, and the lines for the y and z direction therefore overlap and appears as single symmetric lines in the figure. Figure 24b illustrates the angular distributions of prompt gamma-rays in the water phantom, showing an isotropic emission profile at all primary proton energies.

## Angular distribution in the water phantom

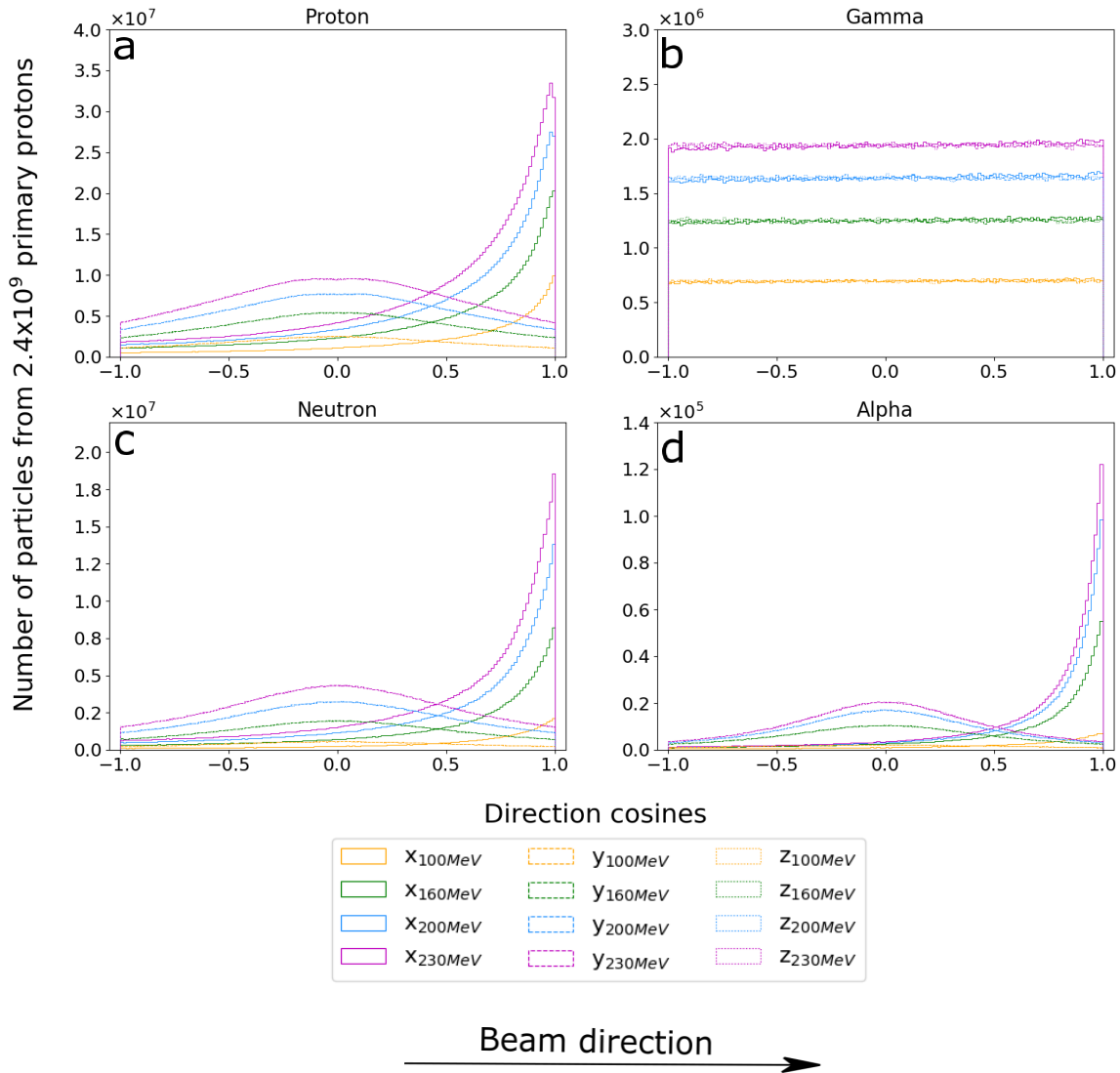


Figure 24: Angular distributions of secondary particles produced in the water phantom. The direction cosines illustrate the direction along the beam axis (x, solid line) and the direction perpendicular to the beam axis (y and z, dashed and dotted line, respectively).

### 5.1.3 Particle fluence

Due to non-elastic reactions, the proton fluence was reduced with increasing depth, as observed in Figure 25a. The proton fluence from the USBIN card include both primary and secondary protons. The proton fluence had a rapid falloff at the end of the range, where most protons stop. The proton straggling can also be seen in the figure as a sigmoid shape at the end of the range. The fluence of prompt gamma-rays and neutrons increased gradually from the entrance of the phantom, up until reaching a maximum, followed by a slow decrease. For



secondary alpha particles, the behaviour predicted by FLUKA simulations was similar; the fluence showed an initial increase up until a maximum, followed by a decrease for all primary proton energies. Further, the fluence had a final peak before it dropped prior to the Bragg peak. This can be seen in Figure 25d. For higher beam energies, the alpha fluence was lower at the entrance, but this changed further into the phantom.

As expected, the particle fluence remained high deeper into the water phantom with increasing primary proton beam energy. Additionally, a much higher production of prompt gamma-rays and neutrons, than that of alpha particles can be observed in Figure 25e. With 2.5 mm bin size and  $2.4 \times 10^9$  primary histories, the statistical uncertainties for the particle fluence were below  $\pm 0.5$  % for all particles, except for alpha particles with an uncertainty of up to 2 % for the lowest primary proton beam energy. Higher primary proton beam energy provided lower statistical uncertainties. From Figure 25e we can also observe that when the proton fluence drops at the Bragg peak, it falls below gamma-ray and neutron fluence, making these particles dominant. The neutron and gamma fluence are very similar, with some higher gamma fluence at the entrance of the phantom and higher neutron fluence distal to the Bragg peak. The alpha fluence was consistently the lowest.

## Fluence distribution in the water phantom

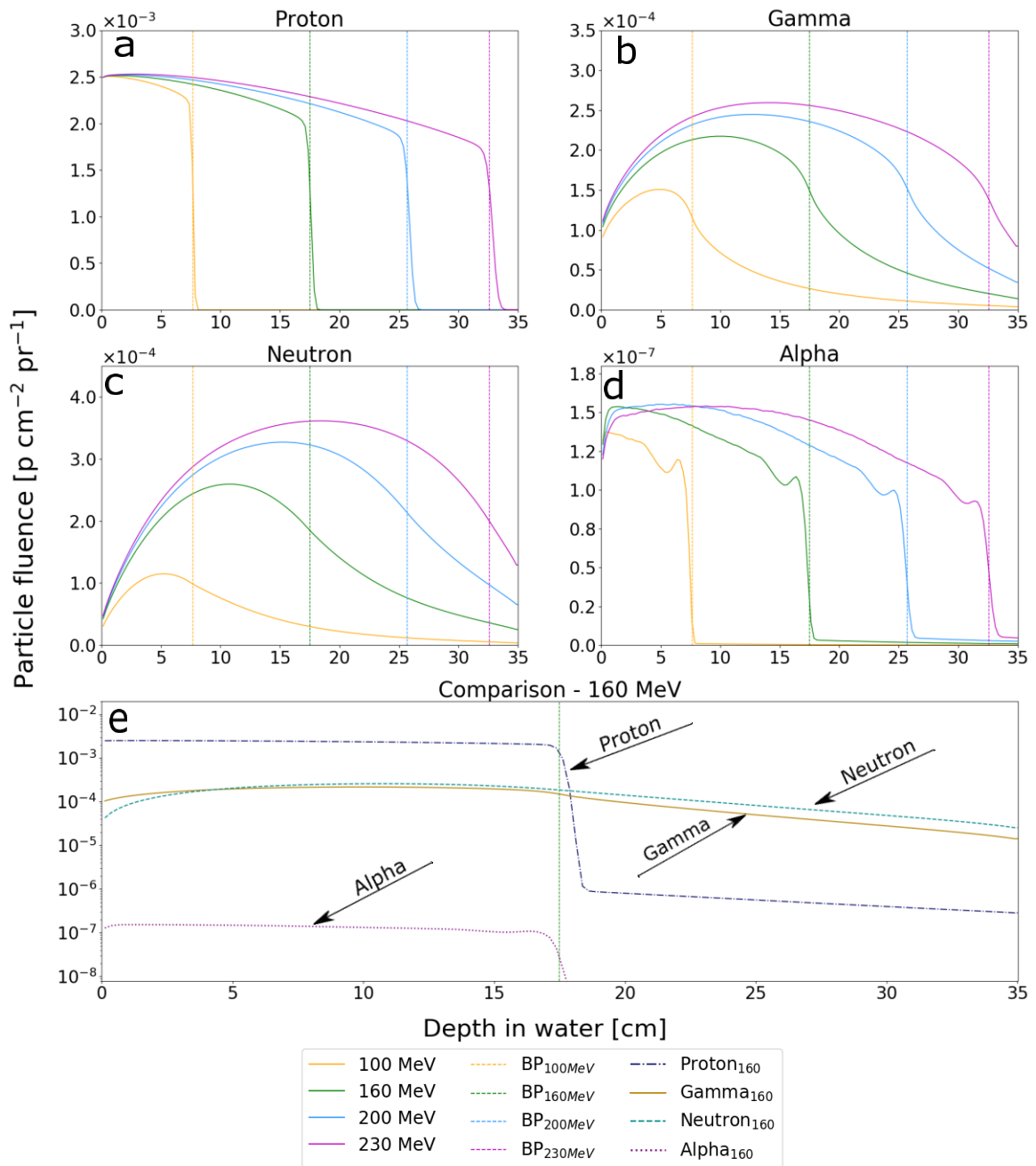


Figure 25: The figure illustrates the proton (a), gamma (b), neutron (c) and alpha (d) fluence as a function of depth in the water phantom. The position of the Bragg peak for the various proton beam energies can also be seen in the figure (vertical dashed line). Comparison of the particle fluences for a 160 MeV proton beam can be seen in the figure (e) with a logarithmic ordinate axis. The fluence was confined to the water phantom.

The following two-dimensional fluence plots for protons, neutrons, gamma-rays and alpha particles (Figure 26, 27, 28 and 29) were confined to the height (y-direction) of the converter and the water phantom. The two-dimensional plots in Figure 26 illustrate the lateral distribution of the proton fluence per primary proton, including the geometry of the water phantom and converter. As observed in the figure, the converter moves along with the Bragg peak and the centre of the detector is aligned with the Bragg peak in depth direction for each energy. The proton fluence can be seen at its maximum at the lateral centre of the water phantom, as this is where the primary proton beam traversed, and quickly reduced at the Bragg peak depth. The proton fluence also decreased rapidly in the lateral direction and was reduced by a factor  $10^7$  at the converter for 100 MeV proton, and approximately four orders of magnitude for 230 MeV protons. Thus, the proton fluence at the converter per primary proton increased with increasing beam energy at a fixed lateral distance to the water phantom, as expected.

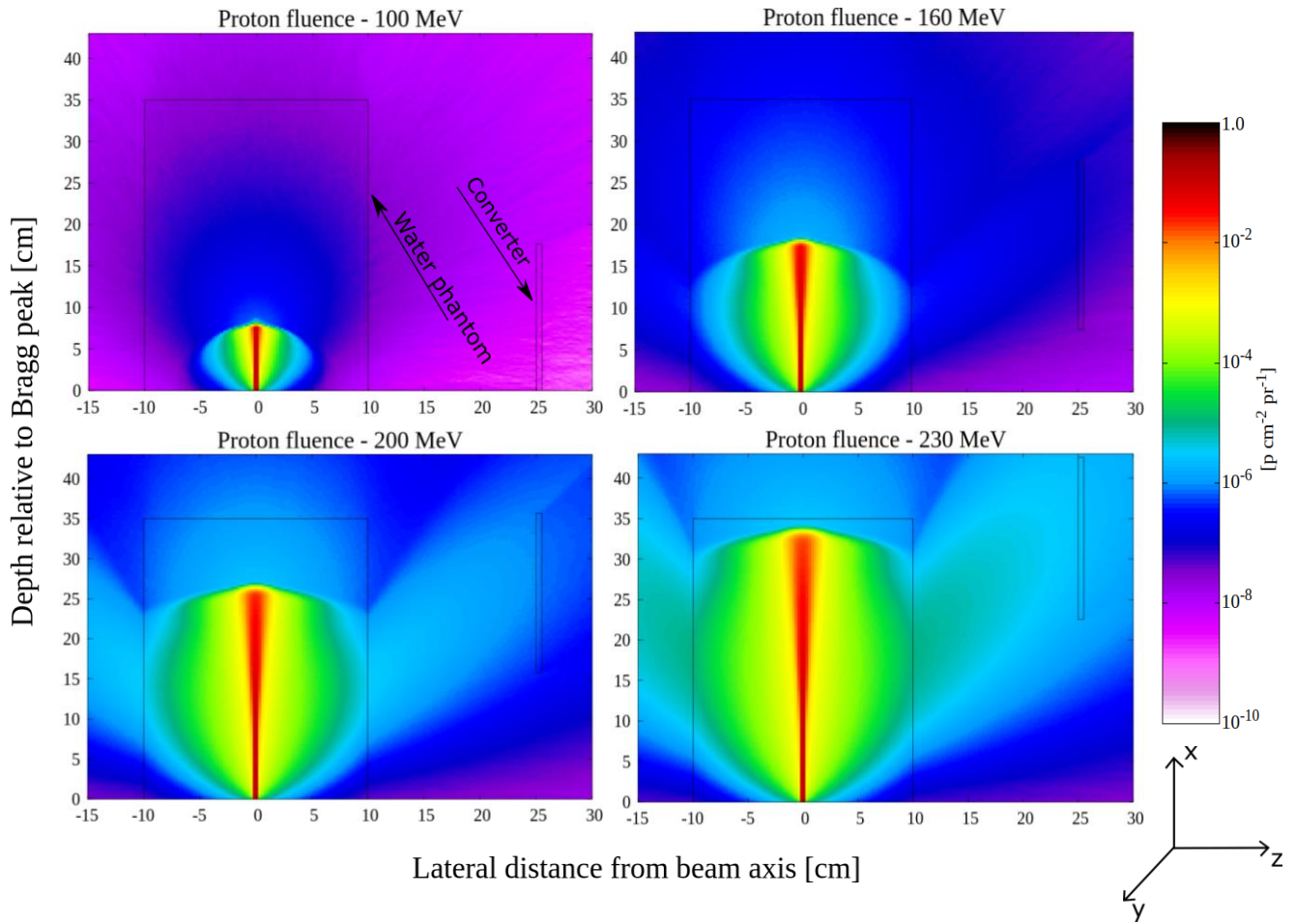


Figure 26: Proton fluence per primary proton for the different beam energies. The proton fluence decreases rapidly at the Bragg peak and is reduced with  $10^4$ - $10^7$  orders of magnitude from the primary beam axis to the converter. The colour bar is logarithmically scaled.

The prompt gamma-ray fluence per primary proton can be seen in Figure 27. The prompt gamma-ray fluences was highest along the primary proton beam axis and showed a lateral decrease by approximately two orders of magnitude from the beam axis to the converter. There was some increase in the gamma-ray fluence by the converter with higher primary beam energies.

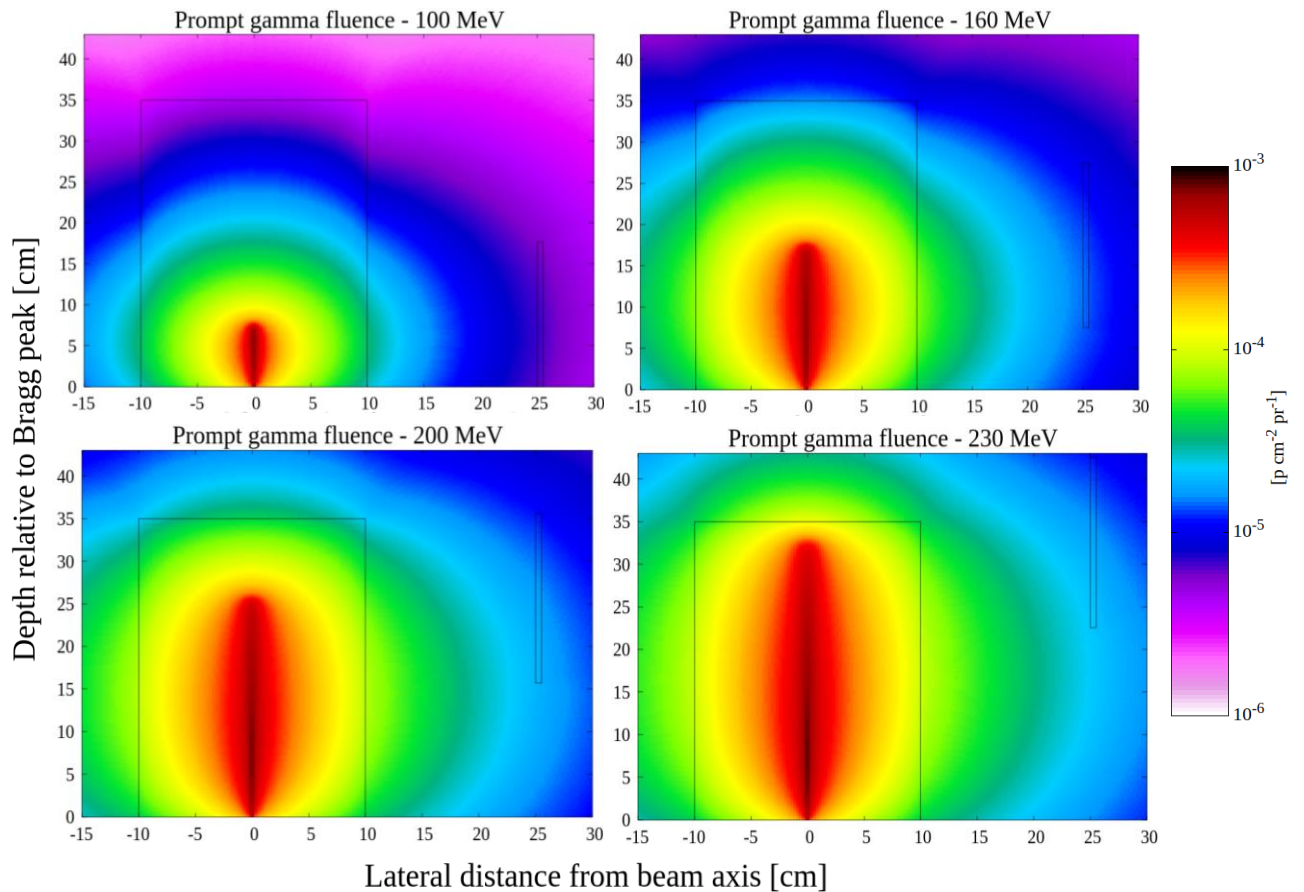


Figure 27: Illustration of the prompt gamma-ray fluence per primary proton for the various proton beam energies. The gamma fluence is reduced by approximately two orders of magnitude from the primary beam axis to the converter. The colour bar is logarithmically scaled.

Two-dimensional plots of the neutron fluence per primary proton are presented in Figure 28. The neutron fluence was highest along the beam axis. As also seen for the other particles, the neutron fluence was reduced laterally from the beam axis, as it dropped approximately two orders of magnitude from the Bragg peak area to the converter. The neutron fluence in the water phantom and in the converter increased with higher primary proton beam energy. As in the case of prompt gamma-rays, the lateral distribution of secondary neutrons was more uniform than for the charged particles.

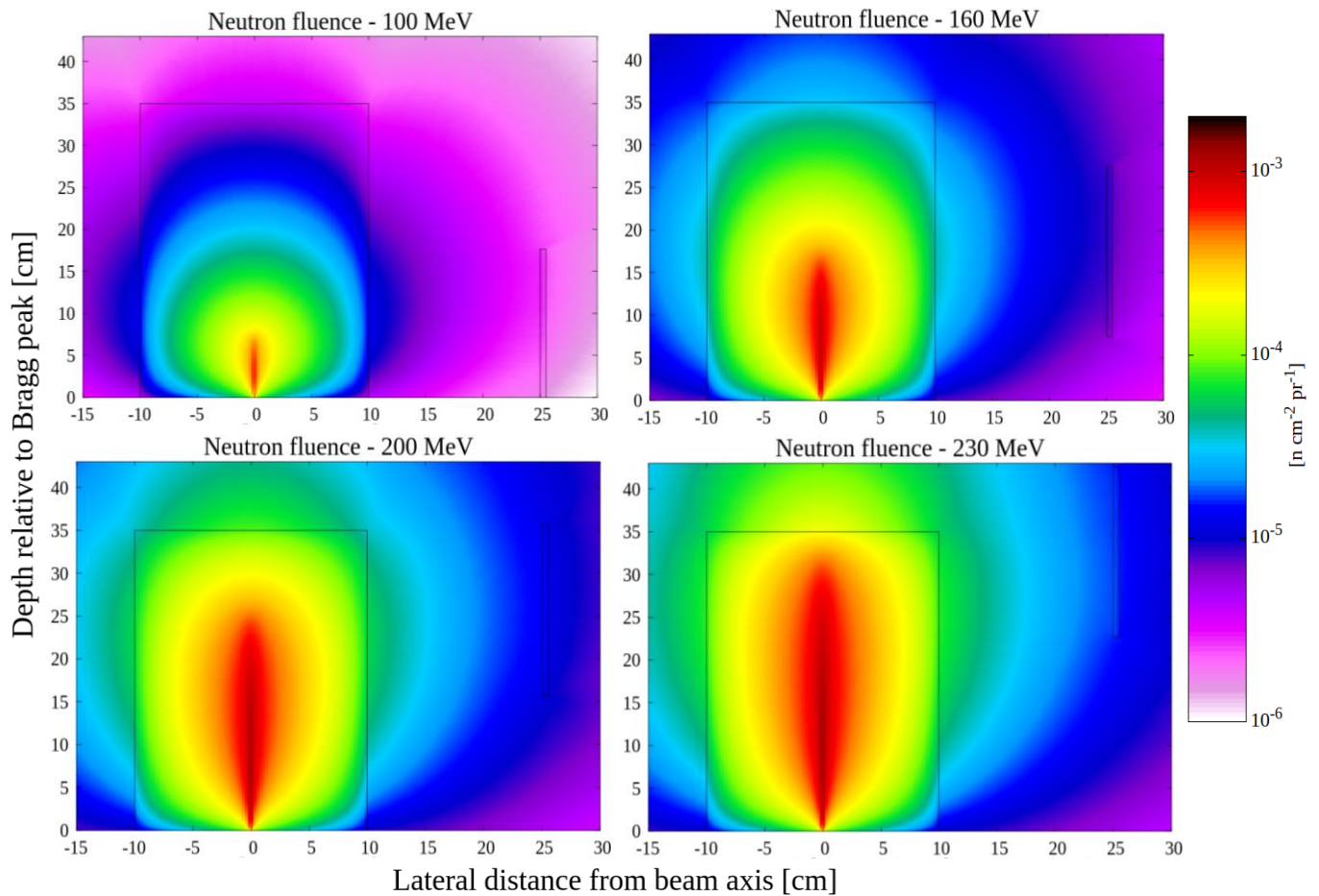


Figure 28: Neutron fluence per primary proton from the water phantom for all proton beam energies. The neutron fluence ranges approximately two orders of magnitude from the primary beam to the converter. The colour bar is logarithmically scaled.

Figure 29 presents the lateral distribution of alpha fluence per primary proton, for the different primary proton beam energies. In Figure 29, the alpha fluence can be observed at its highest along the beam axis before dropping rapidly at the Bragg peak. The alpha fluence was reduced laterally to the converter by a factor of  $10^5$  from the primary beam axis for 100 MeV protons, and by approximately four orders of magnitude for 230 MeV protons. As seen in Figure 29, the alpha fluence was clearly lowest among all secondary particle species examined in this work. Additionally, the statistics for alpha particles were poorer (approximately ten times higher statistical uncertainties), particularly for the lower initial proton beam energies.

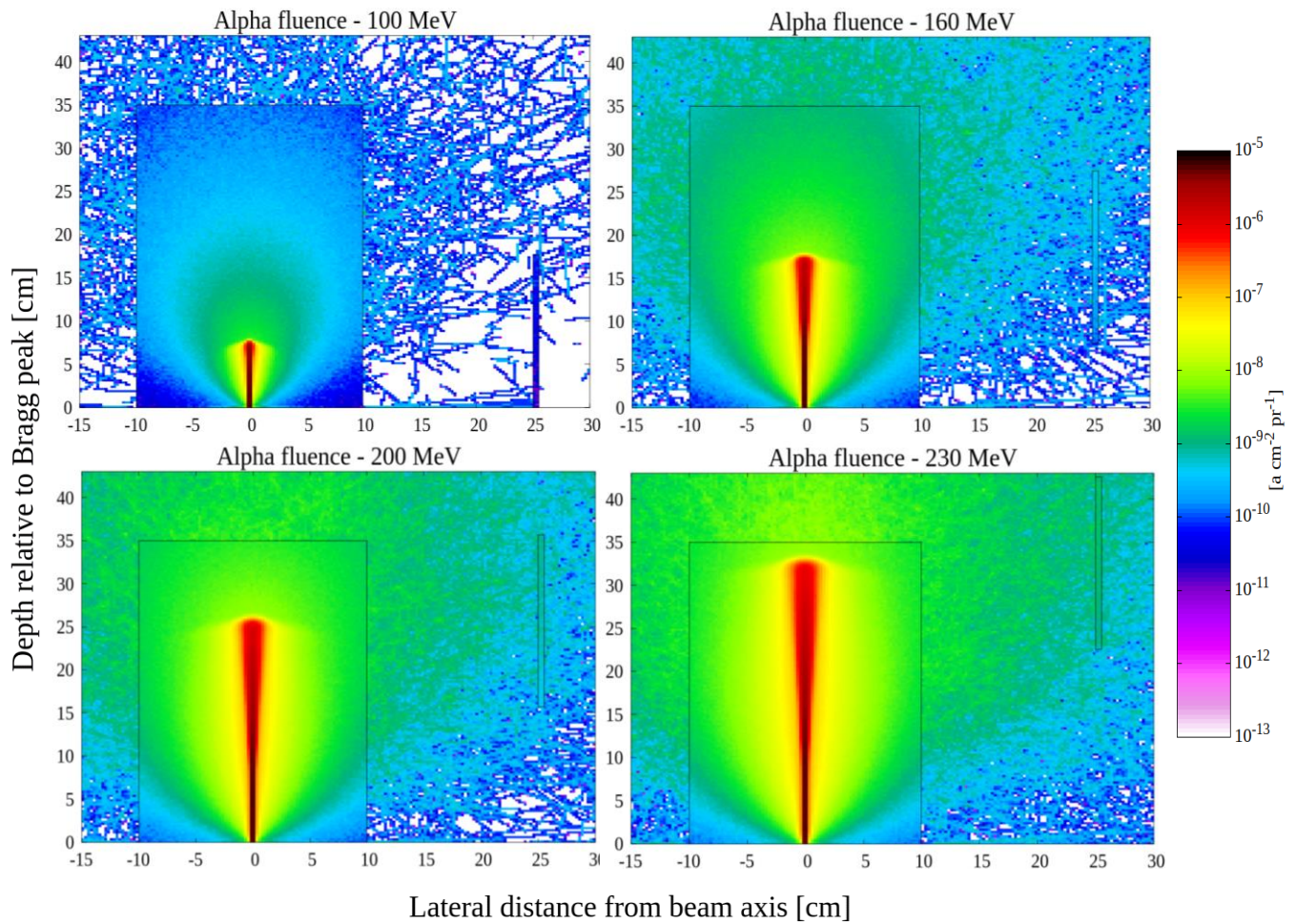


Figure 29: Two-dimensional illustration of the alpha fluence per primary proton for the different beam energies. The alpha fluence decreases fast at the Bragg peak and is highly reduced at the converter. Higher beam energy provides increased alpha fluence, both in the water phantom and in the converter. The colour bar is logarithmically scaled.

#### 5.1.4 Particle distribution at the converter

The energy distribution for particles reaching the detector, i.e. crossing the region between the room and the converter, can be seen in Figure 30. The energy spectra for protons (a) showed mainly energies above 10 MeV for all primary beam energies, and the maximum proton energy increased with higher beam energy. For prompt gamma-rays at the converter boundary, the energy spectra (b) consisted of multiple peaks, with dominant energies of 4.4 MeV and 5.3 MeV, similar to initial energy seen for prompt gamma-rays in the water phantom (Figure 23), indicating that many gamma-rays have reached the detector without losing energy in the water

phantom. In addition, gamma-rays with energy of 2.2 MeV can also be seen dominating at the converter boundary. The 2.2 MeV peak results from capture of secondary thermal neutrons by hydrogen nuclei [49].

It can be observed that the predominant neutron energies (c) were above 1 MeV, ranging up to 200 MeV for the highest proton beam energies. Additionally, a lower energy peak is shown in Figure 30c, representing thermal neutrons. The energy spectra for alpha particles (d) fluctuates fairly, caused by insufficient statistics, which makes it difficult to draw quantitative conclusions. However, the results strongly indicate that alpha particles will have a minor impact on the neutron detector, compared to the other secondaries considered in this work.

The statistical uncertainties for protons, neutrons and prompt gamma-rays are generally under 3 % for the energy bins, whereas higher beam energies provide lower uncertainties. Protons from 100 MeV primary proton beam deviate, as the statistical uncertainties are up to 10 %. For secondary alpha particles, the uncertainty is exceptionally higher with greatly fluctuating uncertainties around 40 %.



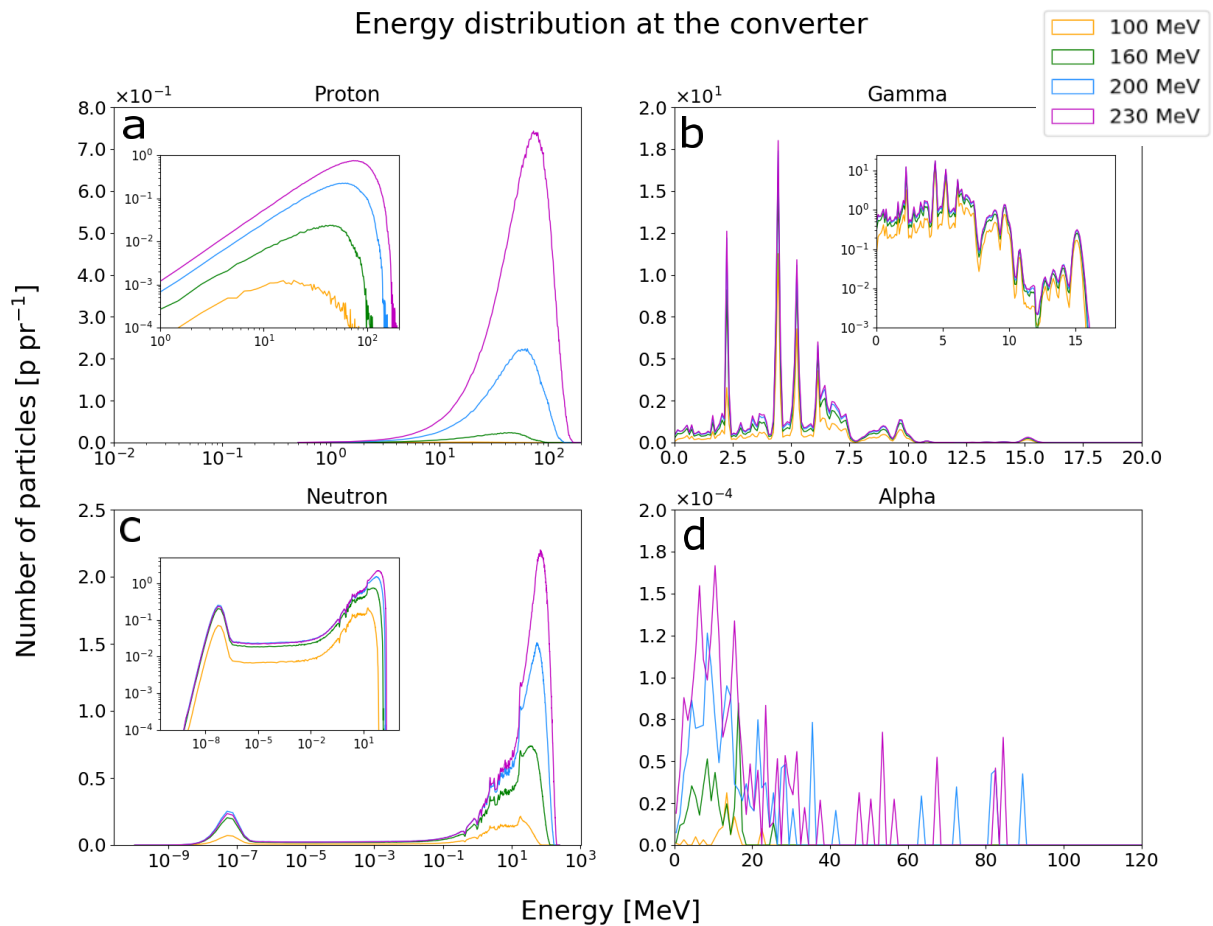


Figure 30: Energy distribution of particles per primary proton at the crossing region between room 1 and the converter, obtained from USRBDX scoring cards. The proton and neutron energy spectra are shown with logarithmic abscissa axis, and both linear (main plot) and logarithmic (inlay) ordinate axis. The prompt gamma-ray energy spectra are shown with linear (main plot) and logarithmic (inlay) ordinate axis.

### 5.1.5 Particle rate comparison in the water phantom and at the detector surface

Figure 31 present the total number of secondaries (i.e. secondary protons, neutrons and prompt gamma-rays) per primary proton created in the water phantom and the total number of secondaries incident on the converter, i.e. the detector surface. Secondary alpha particles have been excluded due to their poor statistics and overall low production rates. It can be observed in Figure 31a, that secondary protons are the dominating secondary particle species in the water phantom for all primary proton beam energies. The number of secondary neutrons per primary proton increases more with increasing primary proton beam energies, than the number of prompt gamma-rays. This trend was seen both in the water phantom and the converter boundary.

The total number of secondaries crossing the converter was only a small fraction of all the produced secondaries, as seen in Figure 31b, and had the greatest reduction of the secondaries. Gamma-rays were the dominant secondaries at the converter boundary, followed by secondary neutrons. The quantitative results for the total number of secondaries per primary proton created in the water phantom and the ones seen at the converter surface can be seen in Table C-1 in Appendix C. The statistical uncertainty for the overall production rates of secondaries (i.e. protons, prompt gamma-rays and neutrons) in the water phantom, were all below 0.6 %, and at the converter the statistical uncertainties were below 5 %.

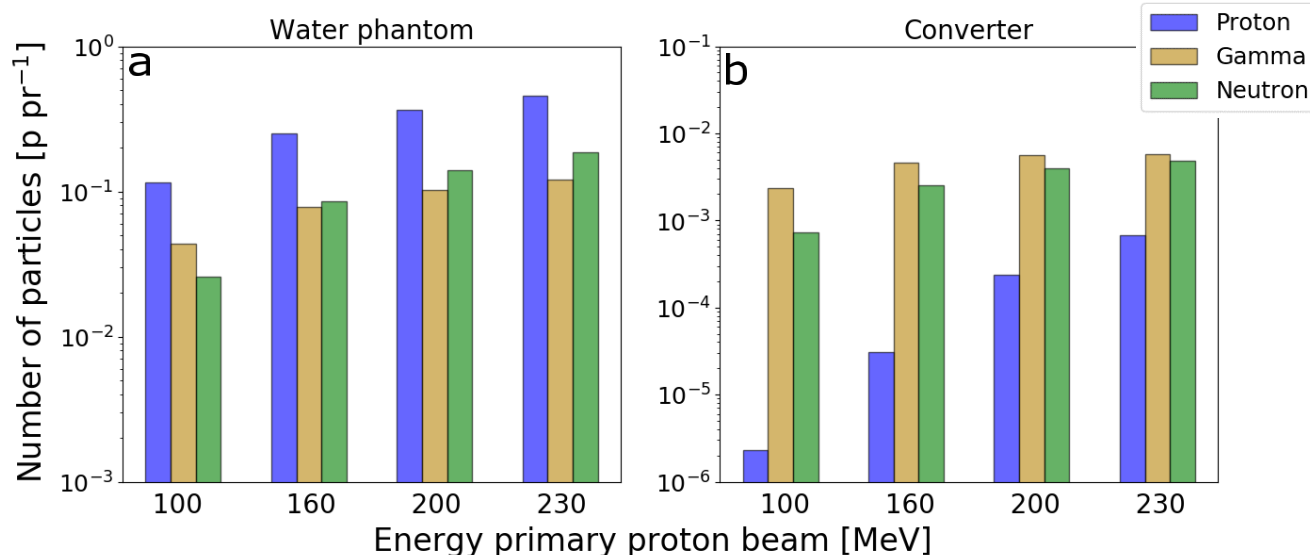


Figure 31: Comparison of the number of secondaries per primary protons created in the water phantom (a) and at the converter surface (b). The figure is illustrated with a logarithmic ordinate axis. Alpha particles are not shown due to their overall low production rates.

### 5.1.6 Geometry variation of the water phantom

The examined water phantom dimensions were 10x10 cm<sup>2</sup>, 20x20 cm<sup>2</sup> and 30x30 cm<sup>2</sup>, and the quantity studied was the energy at the converter surface. The distance from the water phantom to the converter decreased with 5 cm for increasing phantom thickness, while the distance between the primary proton beam and converter were constantly 25 cm. The alteration in fluence and energy distribution with changing phantom thicknesses for the particles at the converter surface can be seen in Figure 32.

It can be observed that smaller phantom dimensions increased the number of protons per primary proton reaching the detector, and that the difference for the phantoms is as high as approximately a factor ten (Fig. 33a). For the dominant gamma-ray energies of 4.4 MeV and 5.3 MeV, it was seen that the number of gamma-rays per primary proton slightly increased with smaller water phantom dimensions (Fig. 33b). For 2.2 MeV, on the other hand, the number of gamma-rays increased with increasing phantom thickness. For secondary neutrons, number of secondary neutrons at the converter increased with smaller phantom dimensions for neutron energies higher than thermal energy, while the opposite can be observed for neutron energies lower than the thermal energy (Fig. 33c). However, this effect was not as pronounced

as for the protons. The proportion of secondary protons reaching the converter are most sensitive to the phantom size of the secondaries. The ratio between the secondaries seen at the converter surface may therefore vary with phantom thickness, indicating a variation for each patient case.

For protons, the maximum particle energy increased with thinner water phantom (Figure 32a), as expected. Figure 32b shows that the prompt gamma-ray energy spectra were virtually independent of the various phantom thickness. The neutron energy spectra were only slightly affected of the various phantom thicknesses, as seen in Figure 32c. The statistics for secondary alpha particles reaching the converter is poor, as the graph fluctuates highly in Figure 32d, making it difficult to draw conclusive results.

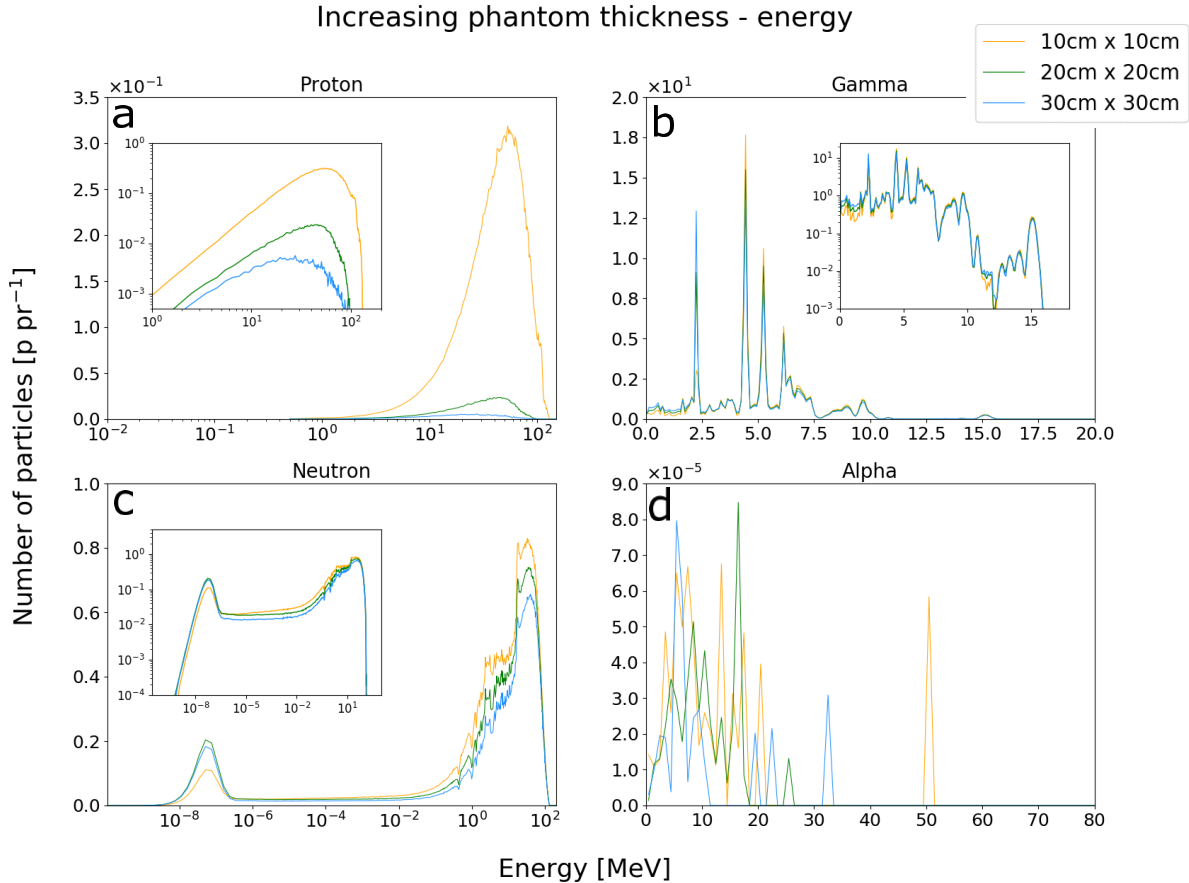


Figure 32: Energy distribution for the particles at the converter, with various phantom dimensions. The standard water phantom dimensions were 20x20 cm<sup>2</sup>.

## 5.2 Patient simulations

### 5.2.1 Dose distribution

Figure 33 shows the  $RBE_{1,1}$  dose distribution in one section of the patient in the transverse plane, with the beam entering the patient from the right. The maximum dose was delivered within the PTV for the prostate. The prescribed dose of 67.5 Gy(RBE) delivered to the PTV was not fully visible in this figure, as only one of the two treatment fields were examined.

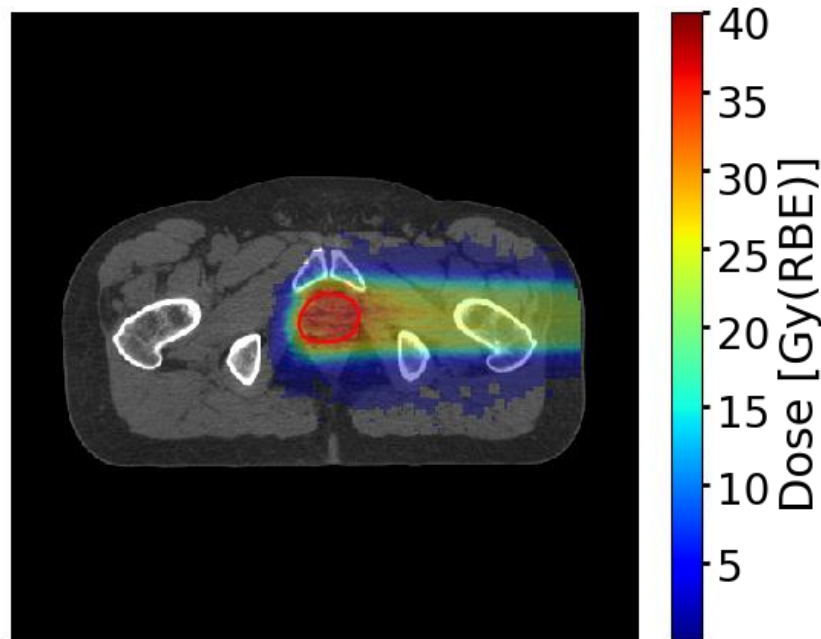


Figure 33: Illustration of the dose distribution in the transverse plane in the patient. The PTV for the prostate is shown with a red contour in the figure.

### 5.2.2 Particle production in the patient

The production distribution for the secondaries are presented in Figure 34. The region covered by the SOBP is also indicated in Figure 34. The most frequently generated particles in the patient were secondary protons. The number of secondary protons increased rapidly as the proton beam entered the patient, followed by a steadier production rate, before it declined in the SOBP area. For secondary neutrons, the growth was also fast from the entrance point, before it stabilized and decreased at the SOBP. The production of prompt gamma-rays

increased unsteadily with depth and further into the SOBP area before declining. For secondary alpha particles, the number increased until its maximum where it stabilized, before falling prior to the SOBP. In line with the expectations and according to the data presented in Figure 34, the least abundant secondary particle species was secondary alpha particles.

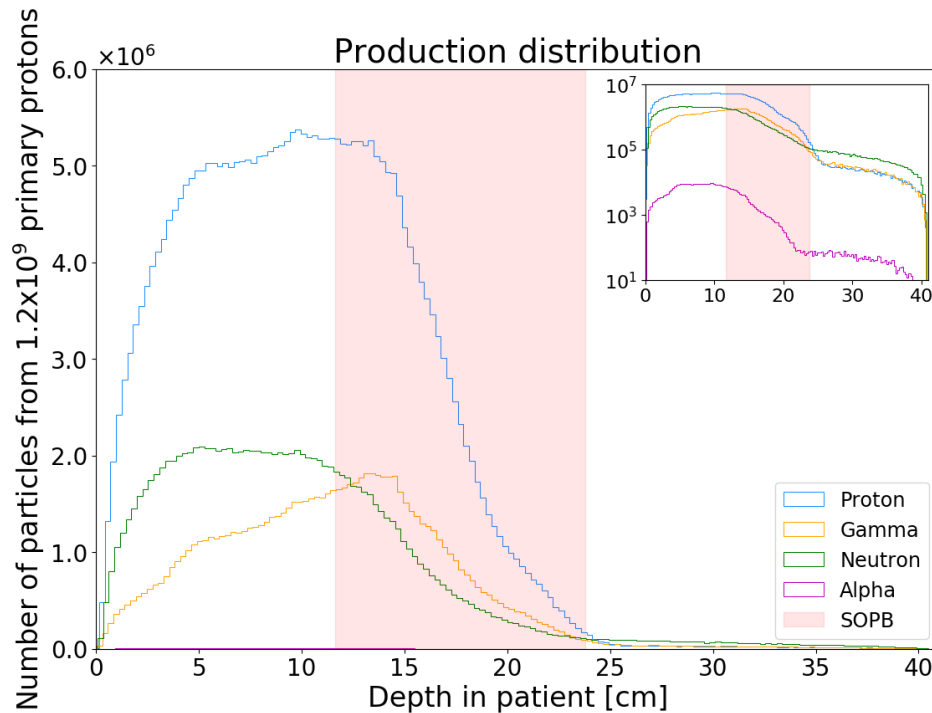


Figure 34: Illustration of the secondary particle production as a function of depth in the patient. The width of the SOBP can also be seen in the plot. The figure is shown with linear (main plot) and logarithmic (inlay) ordinate axis.

Distribution of the initial kinetic energy for the secondaries generated in the patient is illustrated in Figure 35. The figure also indicates the proportions of the secondaries. Similar to the water phantom, the proton and neutron energy spectra were dominated by energies above 1 MeV and up to the maximum primary proton energy, while alpha particles showed mainly energies above 10 MeV. Also, the energy spectra for prompt gamma-rays had numerous energy peaks like in the water phantom simulations, where the dominant energy was 4.4 MeV, that could originating from de-excitation of  $^{12}\text{C}$  or  $^{16}\text{O}$  nuclei [4, 49].

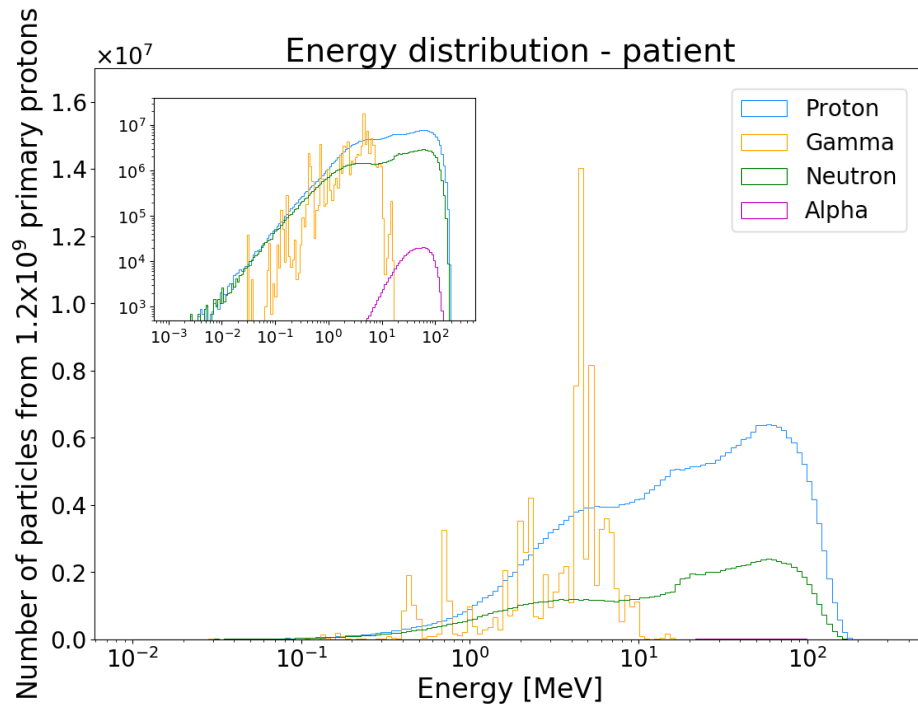


Figure 35: Distribution of the initial kinetic energy for the secondaries created in the patient. The energy spectra are shown with logarithmic bins and with linear (main plot) and logarithmic (inlay) ordinate axis.

The angular distributions for the created secondaries in the patient are presented in Figure 36. As observed for the water phantom, secondary protons (a), neutrons (c) and alpha particles (d) were predominantly emitted in the forward direction. The angular distribution for the directions perpendicular to the proton beam were symmetric. Figure 36b shows how prompt gamma-rays were emitted uniformly in all directions. The angular distributions demonstrate similar emission of secondary particles in both the water phantom and the patient simulation.

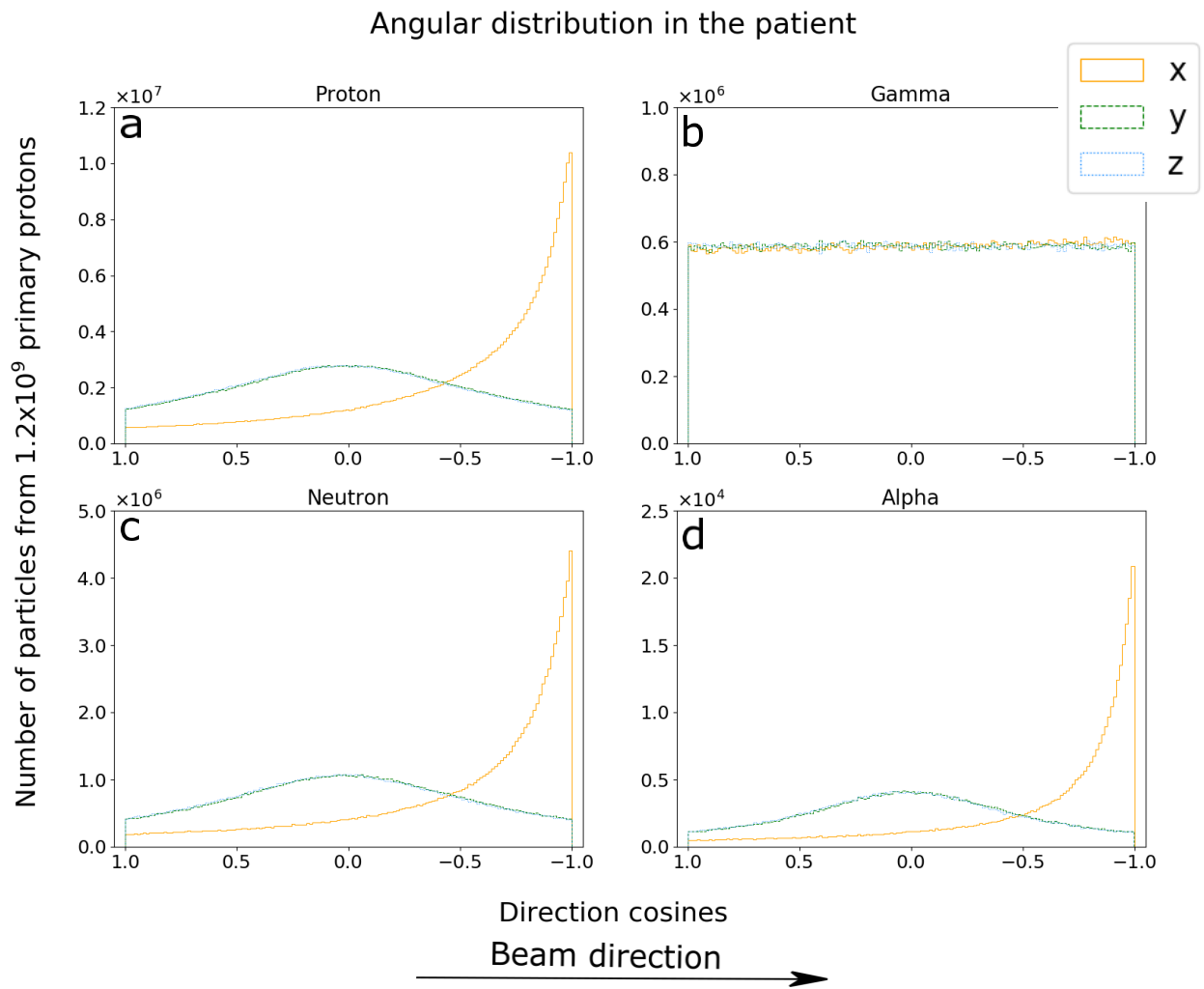


Figure 36: The figure illustrates the angular distribution for the generated secondaries in the patient. The direction cosines illustrate the direction along the beam axis (x, solid histogram) and the y- and z-axes (overlapping dashed and dotted histogram, respectively) perpendicular to the initial beam direction.

### 5.2.3 Particle fluence

The particle fluence as a function of depth in the patient, can be seen in Figure 37. Additionally, the width of the SOBP for the patient plan is shown as a shaded region in the figure. The proton fluence include both primary and secondary protons, in contrast to Figure 34 where only secondary protons are presented. As expected, the proton fluence was the highest of all particles, up until the SOBP, where it started decreasing. At the end of the SOBP and beyond, the proton dropped by approximately three orders of magnitude, far below the neutron and gamma-ray fluence. For prompt gamma-rays and secondary neutrons, the fluence



was somewhat equivalent. Secondary neutrons had a lower fluence prior to the SOBP and increased more than prompt gamma-rays distal to the SOBP. Secondary alpha particles had the lowest fluence compared to the other particles, and the fluence decreased midway in the SOBP, similar to the proton fluence. The statistical uncertainties for proton, gamma and neutron fluence were all below  $\pm 0.2\%$ , and for secondary alpha particles the uncertainty was under  $4\%$ .

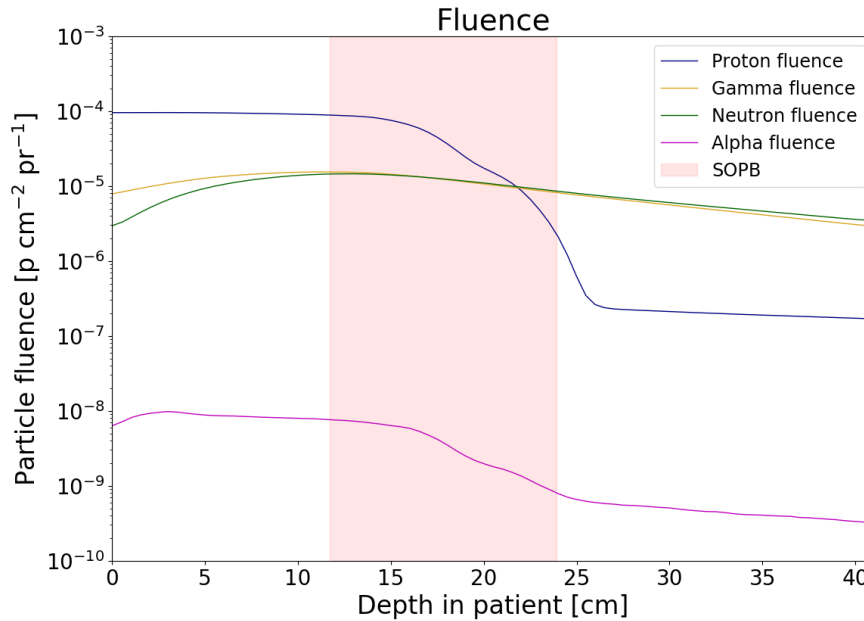


Figure 37: Illustration of the particle fluence as a function of depth in the patient, with a logarithmic ordinate axis. The proton fluence includes both primary and secondary protons. The width of the SOBP is also shown in the figure. The fluence was confined to the patient structure.

Two dimensional plots of the proton, prompt gamma-ray, neutron and alpha fluence are presented in Figure 38. The plots illustrate the particle fluence as a function of depth along the x-axis, and the lateral distribution. As observed in Figure 38a, the proton fluence is rapidly diminished distal to the SOBP, and large angled scattered protons are transmitted towards the converter. The proton fluence dropped by a factor of approximately  $10^4$  from the SOBP area to the converter. The prompt gamma-ray fluence can be seen in Figure 38b, showing how gamma-rays have an isotropic emission and that the fluence drops following the Beer-Lamberts law. The gamma-ray fluence was reduced by about two orders of magnitude from its maximum in the patient to the converter. Likewise, the neutron fluence (Figure 38c) shows a more uniform distribution from the patient with a fluence reduction by the factor of  $10^2$  over

the same area. As seen in Figure 38d, the alpha particles are more scattered from the patient with a reduction of three orders of magnitude at its maximum to the converter.

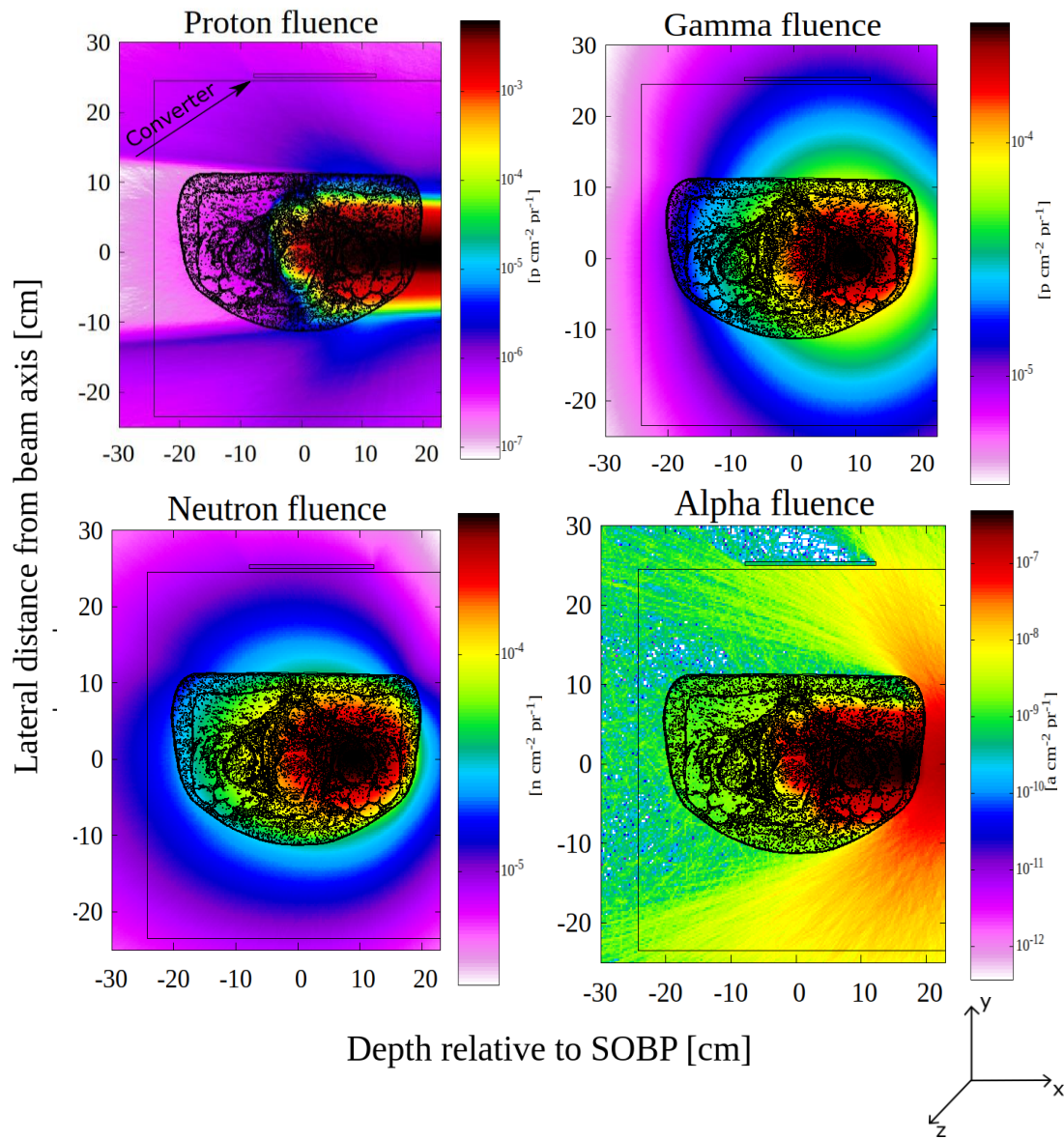


Figure 38: Two-dimensional illustration of the particles fluence per primary proton in a section of the transverse plane in the patient geometry. Geometry of vocalized patient plan and the converter is presented in the plots. The colour bars are logarithmically scaled. The particle fluence were confined to the height of the converter (z direction)

## 5.2.4 Particle distribution at the converter

Figure 39 shows the energy distribution at the converter boundary. As observed in the figure, gamma-rays had the distinctive peak on 4.4 MeV. Similar to the water phantom results, the energy spectra for protons showed mainly energies above 10 MeV and the neutrons were dominated with energies above 1 MeV. Additionally, the peak for thermal neutrons is shown in the figure. Secondary alpha particles appeared to be dominated with energies of 10 MeV, however the statistical uncertainties were high. For protons, neutrons and gamma-rays, the statistical uncertainties were mainly below 5 %.

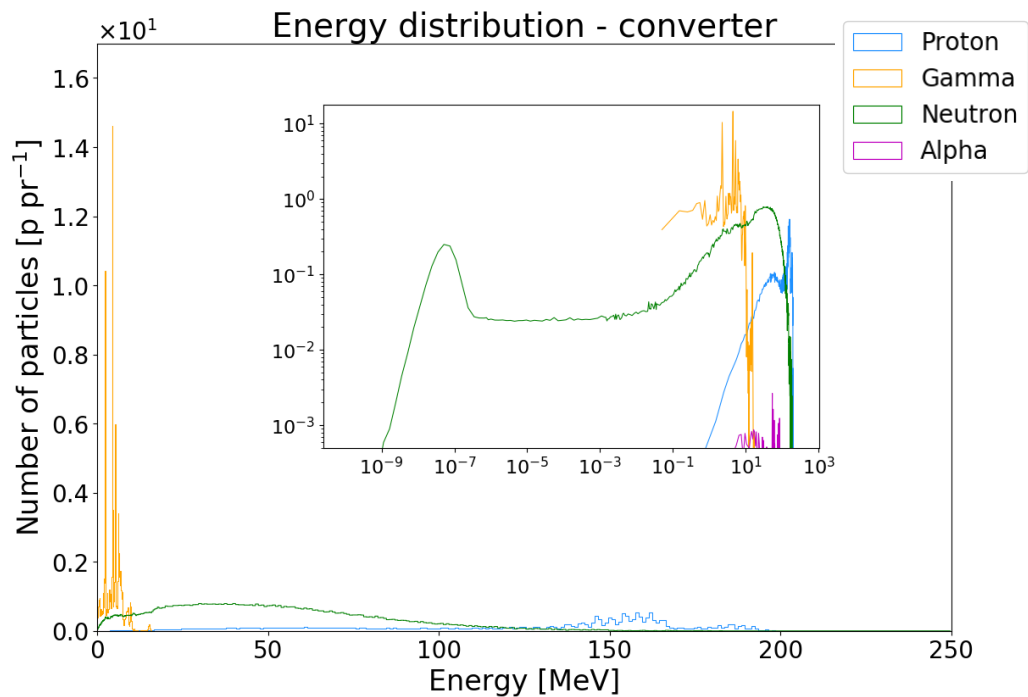


Figure 39: Distribution of kinetic energy for the number of secondaries per primary, reaching the converter. The energy spectra are shown with both linear (main plot) and logarithmic (inlay) ordinate axis.

### 5.2.5 Particle rate comparison in the patient and at the detector surface

Figure 40 presents the total number of secondary protons, neutrons and prompt gamma-rays per primary protons produced in the patient and the number of secondaries per primary proton at the converter boundary ( $20 \times 20 \text{ cm}^2$ ). The secondary alpha particles have been omitted due to poor statistics and lower probability of impact on neutron detection. Similar as for the water phantom, secondary protons were most frequently generated secondary in the patient and were highly attenuated at the converter with only 0.05 % reaching the converter. The secondary neutrons yield was higher than that of prompt gamma-rays in the patient, respectively 0.09 and 0.07 particles per primary proton. At the converter surface, the highest number of secondaries were gamma-rays, with 6.5 % of the generated gamma-rays reaching the converter. For secondary neutrons, the reduction from the ones generated in the patient to the number of neutrons crossing the converter were reduced with 3.1 %. The quantitative results can be found in Table C-2 in Appendix C. The statistical uncertainty for production rates of secondaries in the patient were below 0.5 %, and at the converter the statistical uncertainties were below 4 %.

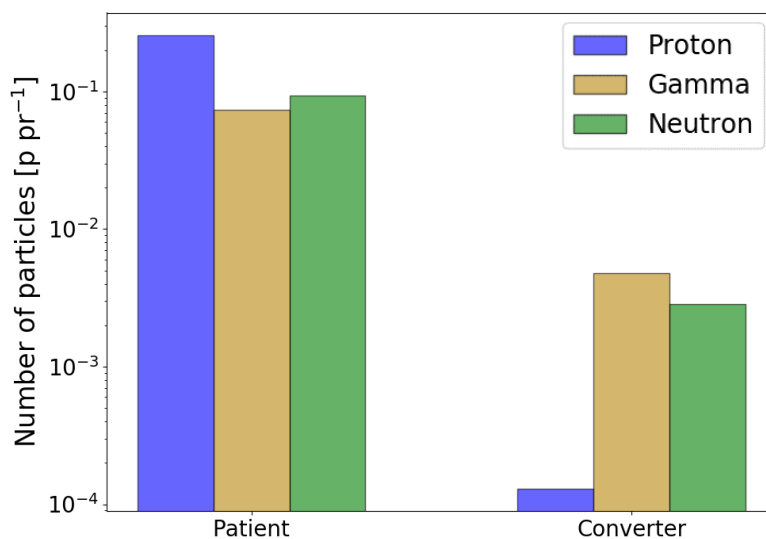


Figure 40: Comparison between the number of secondaries per primary created in the patient against the number of particles at the converter. The figure is illustrated with a logarithmic ordinate axis.

## 6. Summary and discussion

The main objective in this thesis has been to study the secondary radiation (i.e. neutron, proton, gamma-rays and alpha particles) field generated by therapeutically relevant proton beams impinging on a generic water phantom, as well as a realistic patient treatment plan (for a case of prostate cancer). The energy, angular, fluence and spatial distributions of the pertinent secondaries were quantified both at the time of production and at the converter surface. The thesis provides therefore estimates on the characteristics of the secondary particle field which will prove to be essential in the further development on the proposed neutron detector concept for proton beam range verification. The results in this thesis have been obtained from MC simulations performed with the FLUKA software, and results from both the water phantom and patient treatment plan indicate that neutrons and gamma-rays reach the detector with comparable rates, while a somewhat lower proton rate was observed. Alpha particles were shown to be of little relevance compared to the other particles. Hence, secondary protons and prompt gamma-rays were the particles with highest potential to interfere with the secondary neutron detection.

### 6.1 Water phantom simulations

As seen in Figure 31a, secondary protons produced in the water phantom had the highest production rate per primary proton for all the proton beam energies, with 0.12 and 0.45 for proton beam energies of 100 and 230 MeV, respectively. Secondary neutrons had the second highest production rate per primary proton for the two lower proton beam energies; 0.04 and 0.085 against 0.03 and 0.078 for prompt gamma rays. For the two higher proton beam energies, prompt gamma-rays had the second highest production rate in the water phantom; 0.13 and 0.18 for against 0.10 and 0.12 for secondary neutrons.

For secondary protons and neutrons, the energy spectra were dominated by energies above 1 MeV and up to 200 MeV for the highest primary proton beam energy. The energies of 4.4 MeV and 5.3 MeV were the two most distinct and pronounced gamma-ray lines, but gamma-rays of up to 16 MeV were also observed. For prompt gamma-rays, the dominant energies observed in this study agree with previous studies [4, 49]. The energy distribution of secondary protons and neutrons were observed to depend greatly on the primary proton beam.

The maximum particle energies for secondary protons and neutrons increased in proportion with the primary beam energy. Secondary protons and neutrons were predominantly emitted in the forward direction (i.e. along the direction of the incident primary proton beam), whereas prompt gamma-rays, as expected, had an isotropic emission profile.

The particle fluence as a function of water phantom depth (Figure 25) illustrated how the proton fluence were predominant up to the Bragg peak. It should be noted that the MC estimated proton fluence consisted of both primary and secondary protons. At the Bragg peak and distal to it, the proton fluence dropped by approximately three orders of magnitude and was observed to be significantly attenuated. The neutron and gamma fluences were similar as a function of depth in the water phantom, whereas the prompt gamma-ray fluence was observed to be somewhat larger than the neutron fluence at shallow depths, as well as distal to the Bragg peak position in the water phantom.

From the two-dimensional fluence plots for the water phantom, it was observed that the protons fluence was strongly attenuated in the lateral direction with an overall attenuation by a factor of  $10^4$ - $10^7$  at the converter surface. The gamma and neutron fluence on the other hand, were reduced laterally by approximately two orders of the magnitude over the same distance. The fluence for all secondaries increased with increasing primary proton beam energies. This may be expected as the number of incident protons that undergo non-elastic interaction with the nuclei increases with higher initial energy [11].

Due to the limited solid angle covered by the converter and the strong attenuation of secondary protons in the water phantom, only 0.06 % on average of all generated secondary protons reached the converter surface at all primary proton energies considered in this work. For secondary prompt gamma-rays and neutron, a higher fraction of the generated particles, on average, was observed to reach the converter surface. For secondary prompt gamma-rays, this was calculated to be 5 % of all generated secondary prompt gamma-rays, whereas that for secondary neutrons was calculated to be 3 %. At the converter surface, secondary protons and neutrons mostly had energies above 10 MeV and 1 MeV, respectively, while the distinct dominating energy of 4.4 MeV was seen in the gamma-rays energy spectra.

In this thesis, water phantom with different dimensions (10x10 cm<sup>2</sup>, 20x20 cm<sup>2</sup> and 30x30 cm<sup>2</sup>) have been simulated. The different water phantom simulations may be representative for

different patients and tumour sites as the patient geometry and lateral distance from the tumour to the patient surface will vary considerably between patients. Looking at the patient plan in this thesis it is probable that the water phantom of 20x20 cm<sup>2</sup> size is the best match.

## 6.2 Patient treatment plan simulations

The results from the patient treatment plan were similar as the water phantom results. This indicates that water phantom simulations can be a valuable tool to assess different aspects of the detector concept used in this work, as well as exploration of other detection methods using secondary particles from proton therapy. As seen in Figure 40, the production rate per primary proton were highest for secondary protons with 0.26, against 0.07 and 0.09 for prompt gamma-ray and neutrons, respectively. The energy distribution of secondary neutrons and protons were dominated by energies above 1 MeV, and the prompt gamma-ray energy spectra had the same prominent emission line at 4.4 MeV. The angular distributions of the created secondaries were consistent with the water phantom, with neutrons and protons predominantly emitted in the forward direction along the direction of the beam path, and prompt gamma-rays with an isotropic emission.

In Figure 37, the particle fluence as a function of depth in the patient can be seen, illustrating how the proton fluence were predominant up until 2 cm before the end of the SOBP. The proton fluence dropped almost three orders magnitude, below the neutron and gamma-ray fluence. The prompt gamma-ray fluence were second dominating right before the centre of the SOBP where the neutron fluence passed and remained the second dominating particle throughout the patient geometry.

The two-dimensional fluence plots in Figure 38 showed similar reduction in the secondary particle fluence from the patient geometry to the converter surface, as in the case of the water phantom. The proton fluence had the highest lateral reduction corresponding to a factor of about 10<sup>4</sup>, whereas the neutron and gamma fluence had a fluence reduction of two orders of magnitude for the same distance. As seen in Figure 40, secondary protons had the highest reduction rate per primary proton along their path from the patient to the converter, with only 0.05 % secondary protons reaching the converter from the ones generated. Secondary neutrons and gamma-rays had a reduction in their particle rate over the same distance with 3.1 % and

6.5 %, respectively, of all produced secondary neutrons and prompt gamma-rays. Prompt gamma-rays were seen to be the dominating particles at the converter boundary for the patient treatment plan.

### **6.3 Comparison between the water phantom and patient plan simulations**

A clear resemblance between the results from the water phantom and the patient treatment plan was seen. Secondary protons had the highest production rate, but do not contribute significantly to the overall particle incidence rates at the converter surface. The proton fluence, which included contribution from both the primary and secondary protons, had the greatest reduction in both the water phantom and the patient, due to their continuous interaction with matter, and the fact that protons stop following the maximum dose deposition and do not penetrate further distal to the Bragg peak, as seen in the depth dose curves.

With highly reduced number of secondary protons per primary proton at the converter boundary, prompt gamma-rays and secondary neutrons were the dominating particles. Considering that the purpose of the detector concept in neutron-based range verification is to convert neutrons into detectable neutron-induced protons, other protons crossing the converter may be the biggest concern. Hence, a considerably lower number of secondary protons per primary proton is most likely beneficial. However, it is not clear if the signal from secondary protons would increase the uncertainty in the range estimates as also secondary protons may be expected to be correlated to the primary beam range, although Multiple Coulomb Scatter through the phantom/patient geometry and the converter material may have a negative impact on this correlation. In principle, a detector for range verification which could measure, distinguish and make use of signals from all different secondaries would be the optimal, but a technically challenging solution.

For secondary particles crossing the converter, their incidence energies will determine the outcome and most probable reactions that may occur in the converter. Secondary neutrons had energies mainly above 1 MeV, and through head-on collisions between these fast neutrons and nuclei in hydrogenous converter material, protons are knocked out mainly through elastic scattering between the incident fast neutrons and hydrogen-1 nuclei, i.e. (n,p) scattering. A



peak, representing the thermal neutrons, are also seen at the converter boundary that are either absorbed by the converter, or pass through without producing secondary particles. If the thermal neutrons are captured in the converter, prompt gamma-rays can be produced through (n,g) reaction with hydrogen and carbon nuclei in the converter material. This interaction can represent the prominent emission line of 2.2 MeV in the energy spectra at the converter, both for the water phantom and patient.

The proton energy spectra (including both primary and secondary protons) were dominated by proton energies above 10 MeV, and from the PSTAR database program <sup>1</sup> from NIST (National Institute of Standards and Technology) [50], it was found that protons with these energies will traverse through the 5 mm hydrogenous converter. The converter needs to be above 7 mm in order to stop protons with energies of 10 MeV. Gamma-rays at the converter boundary had mainly energies of 4.4 MeV, with the Compton effect as the dominating reaction. Secondary Compton electron produced in Compton scatter events may have sufficient kinetic energies to penetrate the converter and thus contribute to the overall background signal.

The results from this thesis have potential to be improved. For instance, the built-in FLUKA scoring (USRBDX and USRBIN) does not distinguish between primary and secondary protons, while this was done in the tracking code which only included secondary protons from inelastic interactions. Better distinction between primary and secondary protons from the simulations and in the results could give some further insight into the basis for the mixed radiation field at the detector surface. Additionally, even more primary histories for secondary alpha particles could enable more quantitative conclusion. There are also uncertainties within the FLUKA software that cannot be altered. For example, it was observed a poor transition between low- and high energy neutrons (20 MeV), which most likely originate from discrepancies between the neutron models used above and below 20 MeV in FLUKA. This is related to the uncertainties in neutron production due to lack of relevant experimental data and cross sections.

---

<sup>1</sup> <https://physics.nist.gov/PhysRefData/Star/Text/PSTAR.html>

## 6.4 Potential reduction of background contributions

Possible shielding methods in order to reduce potential noise from unwanted secondary radiation in the detector and improvement of the overall signal-to-noise ratio (SNR) for the detection of secondary neutrons is an essential topic to investigate. Secondary protons and prompt gamma-rays reaching the converter material may induce unwanted background contributions distorting the neutron signal, given that the purpose of the pertinent detection system is to detect secondary neutrons and reconstruct their production distributions. By increasing the thickness of the converter, noise from secondary radiation inflicting the secondary neutron detection may be reduced. A thicker converter increases the absorption of secondary protons. However, the converter cannot be too thick as it may affect the conversion detection rates for the neutrons due to self-absorption of neutron-induced protons from (n,p) reactions. Additionally, the prompt gamma-ray energies generated in proton therapy are difficult to absorb through the photoelectric effect, as the converter material has low density and low atomic number.

Another suggestion for possible shielding methods is to add a layer of material on the converter that absorbs and stop the protons, while the secondary neutrons can traverse and convert to detectable protons. For instance, lead or tungsten are materials that can be used to stop protons and also to some degree gamma-rays. With proton energy of 10 MeV, the thickness of the layer needs to be above 0.3 mm for lead, and 0.02 mm for tungsten [50]. Instead of shielding secondary radiation, another interesting approach is to investigate the possibility of a detector system that can utilize several of the generated secondaries for range verification at the same time, i.e. a detector system that could enable a multi-particle range verification technique.

## 7. Conclusion and further work

In this project, the production of secondary radiation in a proposed neutron detector concept for proton beam range verification was quantified. This included estimation of production yields, energy distribution and transport of these particles towards the neutron detector system. Several water phantom scenarios and a treatment plan for prostate cancer were examined for the purpose of this study. From the results performed with Monte Carlo simulations, many similarities between the water phantom and the patient plan were found. Prompt gamma-rays and secondary protons were the particles with highest potential interference on the neutron detection, while alpha particles had little potential relevance. The particle production rate per primary proton were highest for secondary protons, followed by neutrons and prompt gamma-rays. The initial kinetic energy for secondary protons and neutrons were dominated by energies above 1 MeV, and prompt gamma-rays had distinct energy peaks with the most pronounced energy peak at 4.4 MeV. The secondary protons and neutrons were emitted in forward direction, while gamma-rays had an isotropic emission profile. With this and the interaction mechanism for the different particles in mind, the number of prompt gamma-rays reaching the converter were highest, followed by secondary neutrons. The proton fluence had the highest reduction in lateral direction, compared to secondary neutron and prompt gamma-rays. The proportion of protons reaching the converter and their energy was found sensitive to the phantom size, indicating that the ratio between the secondaries can vary for each patient case, with more protons reaching the converter for smaller patients.

Suggestion for further work is to investigate the actual impact secondary particles can have on the neutron detection measurements. This may be accomplished by studying how secondary radiation influences the reconstructed neutron production, based on data from the tracking detectors. Another suggestion for further work is examination and simulation of possible shielding methods in order to reduce potential background contributions from secondary radiation. For instance, a layer with lead or tungsten on the converter could be simulated to see if potential noise from the secondary particles are minimized, providing a better foundation for the design of the neutron detector concept. Lastly, investing the potential for multi particle-based range verification, i.e. analysing the signal from all secondaries could also be a promising alternative to treating the secondaries apart from neutrons as noise.

## Bibliography

- [1] World Health Organization (WHO), "Latest global cancer data: Cancer burden rises to 18.1 million new cases and 9.6 million cancer deaths in 2018," 2018. [online]. Available: [https://www.iarc.fr/wp-content/uploads/2018/09/pr263\\_E.pdf](https://www.iarc.fr/wp-content/uploads/2018/09/pr263_E.pdf)
- [2] R. Baskar, K. A. Lee, R. Yeo, and K. W. Yeoh, "Cancer and radiation therapy: current advances and future directions," *Int J Med Sci*, vol. 9, no. 3, pp. 193-9, Febr. 2012, doi:10.7159/ijms.3635
- [3] S. Gianfaldoni, R. Gianfaldoni, U. Wollina, J. Lotti, G. Tchernev, and T. Lotti, "An Overview on Radiotherapy: From Its History to Its Current Applications in Dermatology," *Open Access Maced J Med Sci*, vol. 5, no. 4, pp. 521-525, Jul. 2017, doi:10.3889/oamjms.2017.122
- [4] J. M. Verburg, "Reducing Range Uncertainty in Proton Therapy," Ph.D. dissertation, Dept. of Applied Physics, Technische Universiteit Eindhoven, Eindhoven, Netherlands, 2015.
- [5] J. D. Bourland, "Radiation Oncology Physics," in *Clinical Radiation Oncology*, 4th Edition, L. L. Gunderson and J. E. Tepper, Eds. Philadelphia: Elsevier, 2016, pp. 93-147.
- [6] J. P. G. Faiz and J.P.Gibbons, *Khan's The Physics of Radiation Therapy*, 5th Edition, Philadelphia, USA: Lippincott Williams & Wilkins, 2014.
- [7] J. Thariat, J.-M. Hannoun-Levi, A. Sun Myint, T. Vuong, and J.-P. Gérard, "Past, present, and future of radiotherapy for the benefit of patients," *Nature Reviews Clinical Oncology*, Perspective vol. 10, p. 52-69, Nov. 2012, doi:10.1038/nrclinonc.2012.203
- [8] D. A. Palma, W. F. A. R. Verbakel, K. Otto, and S. Senan, "New developments in arc radiation therapy: A review," *Cancer Treat Rev*, vol. 36, no. 5, pp. 393-399, Aug. 2010, doi: 10.1016/j.ctrv.2010.01.004
- [9] N. G. Burnet, S. J. Thomas, K. E. Burton, and S. J. Jefferies, "Defining the tumour and target volumes for radiotherapy," *Cancer Imaging*, vol. 4, no. 2, pp. 153-161, 2004, doi: [10.1102/1470-7330.2004.0054](https://doi.org/10.1102/1470-7330.2004.0054)
- [10] X. Tian, K. Liu, Y. Hou, J. Cheng, and J. Zhang, "The evolution of proton beam therapy: Current and future status," *Mol Clin Oncol*, vol. 8, no. 1, pp. 15-21, Jan. 2018, doi: [10.3892/mco.2017.1499](https://doi.org/10.3892/mco.2017.1499)
- [11] D. N. Wayne and Z. Rui, "The physics of proton therapy," *Physics in Medicine and Biology*, vol. 60, no. 8, pp.155-209, Mar. 2015, doi:10.1088/0031-9155/60/8/R155
- [12] J. Leeman *et al.*, "Proton therapy for head and neck cancer: expanding the therapeutic window," *The Lancet Oncology*, vol. 18, no. 5, pp 254-265, Apr. 2017, doi: 10.1016/S1470-2045(17)30179-1
- [13] C. H. Stokkevag *et al.*, "Estimated risk of radiation-induced cancer following paediatric cranio-spinal irradiation with electron, photon and proton therapy," *Acta Oncol*, vol. 53, no. 8, pp. 1048-57, Aug. 2014, <https://doi.org/10.3109/0284186X.2014.928420>
- [14] M. Durante and J. S. Loeffler, "Charged particles in radiation oncology," *Nature Reviews Clinical Oncology*, vol. 7, no. 1, pp. 37-43, Jan. 2010, doi:10.1038/nrclinonc.2009.183

- [15] H. Harada and S. Murayama, "Proton beam therapy in non-small cell lung cancer: state of the art," *Lung Cancer (Auckl)*, vol. 8, pp. 141-145, Aug. 2017, doi:[10.2147/LCTT.S117647](https://doi.org/10.2147/LCTT.S117647)
- [16] S. Lehrack *et al.*, "Submillimeter ionoacoustic range determination for protons in water at a clinical synchrocyclotron," *Physics in Medicine & Biology*, vol. 62, no. 17, pp. 20-30, Aug. 2017, <https://doi.org/10.1088/1361-6560/aa81f8>
- [17] A. C. Knopf and A. Lomax, "In vivo proton range verification: a review," *Phys Med Biol*, vol. 58, no. 15, pp.131-160, Jul. 2013, doi:[10.1088/0031-9155/58/15/R131](https://doi.org/10.1088/0031-9155/58/15/R131)
- [18] K. S. Ytre-Hauge, K. Skjerdal, J. Mattingly, and I. Meric, "A Monte Carlo feasibility study for neutron based real-time range verification in proton therapy," *Scientific Reports*, vol. 9, no. 1, Febr. 2019, Art.no.211, <https://doi.org/10.1038/s41598-019-38611-w>
- [19] W. R. Leo, *Techniques for nuclear and particle physics experiments*, 2nd Edition, New York, USA:Springer-Verlag Berlin Heidelberg, 1994.
- [20] Illustrert vitenskap. *Hvilken miks av grunnstoffer har vi i oss?* [Online]. Available: <https://illvit.no/mennesket/kroppen/hvilken-miks-av-grunnstoffer-har-vi-i-oss>
- [21] Evaluated Nuclear Data File (ENDF) [Online]. Available: <https://www-nds.iaea.org/exfor/endl.htm>
- [22] A. Carnicer, V. Letellier, G. Rucka, G. Angellier, W. Sauerwein, and J. Héroult, "Study of the secondary neutral radiation in proton therapy: Toward an indirect in vivo dosimetry," vol. 39, no. 12, pp. 7303-7316, 2012, doi: 0.1118/1.4765049
- [23] S. B. Jia, M. H. Hadizadeh, A. A. Mowlavi, and M. E. Loushab, "Evaluation of energy deposition and secondary particle production in proton therapy of brain using a slab head phantom," *Reports of practical oncology and radiotherapy*, vol. 19, no. 6, pp. 376-384, 2014, <https://doi.org/10.1016/j.rpor.2014.04.008>
- [24] A. C. Kraan, "Range Verification Methods in Particle Therapy: Underlying Physics and Monte Carlo Modeling," *Front Oncol*, vol. 5, Jul. 2015, Art.no.150, doi:[10.3389/fonc.2015.00150](https://doi.org/10.3389/fonc.2015.00150)
- [25] L. Grzanka, "Modelling beam transport and biological effectiveness to develop treatment planning for ion beam radiotherapy," Ph.D. dissertation, Polish Academy of Sciences, The Henryk Niewodniczański Institute of Nuclear Physics, Krakow, Poland, 2013.
- [26] J. Šolc, V. Vondráček, Z. Vykydal, and M. Králík, "Neutron spectral fluence and dose distribution inside a NYLON 6 phantom irradiated with pencil beam of high energy protons," *Radiation Measurements*, vol. 109, pp. 13-23, 2018, doi:[10.1016/j.radmeas.2017.12.006](https://doi.org/10.1016/j.radmeas.2017.12.006)
- [27] G. F. Knoll, *Radiation detection and measurement*, 4th Edition, New Jersey, USA: John Wiley & Sons, Inc., 2010.
- [28] E. B. Podgorsak, *Radiation physics for medical physicists*, 2nd Edition, Berlin, Germany: Springer, 2010.
- [29] H. Cember and T. E. Johnson, *Introduction to health physics*, 4th Edition, New York, USA: McGraw-Hill Companies, Inc, 2009.
- [30] J. Choi and J. O. Kang, "Basics of particle therapy II: relative biological effectiveness," *Radiation oncology journal*, vol. 30, no. 1, pp. 1-13, Mar. 2012, doi: [10.3857/roj.2012.30.1.1](https://doi.org/10.3857/roj.2012.30.1.1)
- [31] A. L. McNamara, J. Schuemann, and H. Paganetti, "A phenomenological relative biological effectiveness (RBE) model for proton therapy based on all published in

- vitro cell survival data," *Phys Med Biol*, vol. 60, no. 21, pp. 8399-8416, Nov. 2015, [doi:10.1088/0031-9155/60/21/8399](https://doi.org/10.1088/0031-9155/60/21/8399)
- [32] International Commission on Radiation Units & Measurements, "Prescribing, Recording, and Reporting Proton-Beam Therapy (ICRU Report 78)," 2007. [Online]. Available: <https://icru.org/home/reports/prescribing-recording-and-reporting-proton-beam-therapy-icru-report-78>
- [33] B. Jones, "Why RBE must be a variable and not a constant in proton therapy," *Br J Radiol*, vol.89, no.1063, May 2016, [doi: doi.org/10.1259/bjr.20160116](https://doi.org/10.1259/bjr.20160116)
- [34] H. Liu and J. Y. Chang, "Proton therapy in clinical practice," *Chinese journal of cancer*, vol. 30, no. 5, pp. 315-326, May 2011, [doi: 10.5732/cjc.010.10529](https://doi.org/10.5732/cjc.010.10529) H. Liu and J. Y. Chang, "Proton therapy in clinical practice," *Chinese journal of cancer*, vol. 30, no. 5, pp. 315-326, 2011.
- [35] R. A. Grün, "Impact of tissue specific parameters on the prediction of the biological effectiveness for treatment planning in ion beam therapy," Ph.D. dissertation, Dept. of Radiotherapy, Philipps University of Marburg, Marburg, Germany, 2014.
- [36] H. Paganetti, "Range uncertainties in proton therapy and the role of Monte Carlo simulations," *Physics in medicine and biology*, vol. 57, no. 11, pp. 99-117, May 2012, <https://doi.org/10.1088/0031-9155/57/11/R99>
- [37] G. Poludniowski, N. M. Allinson, and P. M. Evans, "Proton radiography and tomography with application to proton therapy," *The British journal of radiology*, vol. 88, no. 1053, Jul. 2015, [doi: 10.1259/bjr.20150134](https://doi.org/10.1259/bjr.20150134)
- [38] F. Hueso-González, M. Rabe, T. A. Ruggieri, T. Bortfeld, and J. M. Verburg, "A full-scale clinical prototype for proton range verification using prompt gamma-ray spectroscopy," *Physics in medicine and biology*, vol. 63, no. 18, Sept. 2018, <https://doi.org/10.1088/1361-6560/aad513>
- [39] H. Paganetti and G. El Fakhri, "Monitoring proton therapy with PET," *The British journal of radiology*, vol. 88, no. 1051, Jun. 2015. <https://doi.org/10.1259/bjr.20150173>
- [40] M. Marafini *et al.*, "MONDO: a neutron tracker for particle therapy secondary emission characterisation," *Phys Med Biol*, vol. 62, no. 8, pp. 3299-3312, Apr. 2017, <https://doi.org/10.1088/1361-6560/aa623a>
- [41] A. Ferrari, P. Sala, A. Fasso, and J. Ranft, "FLUKA: a multi-particle transport code (Program vession 2005)".
- [42] T. T. Bohlen *et al.*, "The FLUKA Code: Developments and Challenges for High Energy and Medical Applications," *Nuclear Data Sheets*, vol. 120, pp. 211-214, Jun. 2014, <https://doi.org/10.1016/j.nds.2014.07.049>
- [43] S. Raychaudhuri, "Introduction to Monte Carlo simulation," *2008 Winter Simulation Conference*, Miami, FL, USA, 2008, pp. 91-100. [doi: 10.1109/WSC.2008.4736059](https://doi.org/10.1109/WSC.2008.4736059)
- [44] A. Ferrari, P. R. Sala, A. Fasso, and J. Ranft, "FLUKA: A multi-particle transport code," in "CERN-2005-10 (2005), INFN/TC\_05/11, SLAC-R-773," 2005.
- [45] A. Fasso, A. Ferrari, J. Ranft, and P. R. Sala. (09.09). *Fluka online manual*. Accessed: Aug. 12, 2019. [Online]. Available: <http://www.fluka.org/content/manuals/fluka2011.manual>
- [46] H. Paganetti, Ed. *Proton therapy physics*. Boca Raton, FLorida, USA: CRC Press - Taylor & Francis Group, 2012

- [47] J. C. Watkins, *An Introduction to the Science of Statistics: From Theory to Implementation*. 2016. [Online]. Available: <https://www.math.arizona.edu/~jwatkins/statbook.pdf>
- [48] L. F. Fjæra, "Development of a Monte Carlo Based Treatment Planning Verification Tool for Particle Therapy," M.S.thesis, Dept. of Physics and Technology, University of Bergen, Bergen, Norway, 2016.
- [49] M. Zarifi, S. Guatelli, D. Bolst, B. Hutton, A. Rosenfeld, and Y. Qi, "Characterization of prompt gamma-ray emission with respect to the Bragg peak for proton beam range verification: A Monte Carlo study," *Physica Medica*, vol. 33, pp. 197-206, Jan. 2017, <https://doi.org/10.1016/j.ejmp.2016.12.011>.
- [50] NIST. (2013, 21.05.2013). *Stopping-Power and Range Tables for Electrons, Protons, and Helium Ions*. [Online]. Available: <http://physics.nist.gov/PhysRefData/Star/Text/PSTAR.html>

# Appendix A – FLUKA input file

#define	230MEV	:			
#define	160MEV	:			
#define	200MEV	:			
#define	100MEV	:			
#define	coal_evap	:			
#define	iontrans	:			
#define	emfcut	:			
TITLE	Master thesis - impact of secondary radiation on neutron based range verification in proton therapy				
Set the defaults for precision simulations					
DEFAULTS	PRECISIO ▾				
#if	100MEV ▾				
Define the beam characteristics 0.8% spread					
BEAM	Beam: Energy ▾	E: 0.1	Part: PROTON ▾		
	Δp: Flat ▾	Δφ: Flat ▾	Δφ:		
	Shape(X): Gauss ▾	x(FWHM): 1.0	Shape(Y): Gauss ▾	y(FWHM): 1.0	
#elif	160MEV ▾				
Define the beam characteristics 0.8% spread					
BEAM	Beam: Energy ▾	E: 0.16	Part: PROTON ▾		
	Δp: Flat ▾	Δφ: Flat ▾	Δφ:		
	Shape(X): Gauss ▾	x(FWHM): 1.0	Shape(Y): Gauss ▾	y(FWHM): 1.0	
#elif	200MEV ▾				
Define the beam characteristics 0.6%spread					
BEAM	Beam: Energy ▾	E: 0.2	Part: PROTON ▾		
	Δp: Flat ▾	Δφ: Flat ▾	Δφ:		
	Shape(X): Gauss ▾	x(FWHM): 1.0	Shape(Y): Gauss ▾	y(FWHM): 1.0	
#elif	230MEV ▾				
Define the beam characteristics 0.3%spread					
BEAM	Beam: Energy ▾	E: 0.23	Part: PROTON ▾		
	Δp: Flat ▾	Δφ: Flat ▾	Δφ:		
	Shape(X): Gauss ▾	x(FWHM): 1.0	Shape(Y): Gauss ▾	y(FWHM): 1.0	
#else					
Define the beam characteristics					
BEAM	Beam: Energy ▾	E: 0.2	Part: PROTON ▾		
	Δp: Flat ▾	Δφ: Flat ▾	Δφ:		
	Shape(X): Gauss ▾	x(FWHM): 1.0	Shape(Y): Gauss ▾	y(FWHM): 1.0	
#endif					
Define the beam position					
BEAMPOS	x: -1	y:	z:	Type: POSITIVE ▾	
	cosx: 1	cosy:			
#if	100MEV ▾				
BP at 7.63					
ROT-DEFI	Axis: X ▾	Id: 0	Name: POS		
	Polar:	Azm:	Δz:		
	Δx: 12.37	Δy:			
#elif	160MEV ▾				
BP at 17.48					
ROT-DEFI	Axis: X ▾	Id: 0	Name: POS		
	Polar:	Azm:	Δz:		
	Δx: 2.52	Δy:			
#elif	200MEV ▾				
BP at 25.68					
ROT-DEFI	Axis: X ▾	Id: 0	Name: POS		
	Polar:	Azm:	Δz:		
	Δx: 5.68	Δy:			
#elif	230MEV ▾				
BP at 32.58					
ROT-DEFI	Axis: X ▾	Id: 0	Name: POS		
	Polar:	Azm:	Δz:		
	Δx: 12.58	Δy:			
#else					
ROT-DEFI	Axis: X ▾	Id: 0	Name: POS		
	Polar:	Azm:	Δz:		
	Δx: 5.6	Δy:			
#endif					
GEOBEGIN	Title:	Log: ▾	Acc: ▾	Opt: ▾	Fmt: COBNAME ▾
		Geometry: ▾	Out: ▾		
Black body					
SPH	blkbody	x: 0	y: 0	z: 0	
		R: 100000			
Void sphere					
SPH	void	x: 0	y: 0	z: 0	
		R: 10000			
RPP	water	Xmin: 0	Xmax: 35		
		Ymin: -10	Ymax: 10		
		Zmin: -10	Zmax: 10		
RPP	room	Xmin: -30	Xmax: 60		
		Ymin: -40	Ymax: 40		
		Zmin: -40	Zmax: 40		
#if	160MEV ▾				
\$start_transform					
		Trans: -POS ▾			
#elif	100MEV ▾				
\$start_transform					
		Trans: -POS ▾			
#else					
\$start_transform					
		Trans: POS ▾			
#endif					
5 mm thickness					
RPP	convert	Xmin: 10	Xmax: 30		
		Ymin: -10	Ymax: 10		
		Zmin: 25	Zmax: 25.5		



	YZP	x1	x: 10	
	VZP	x2	x: 30	
	ROOM7	<b>transform</b>		
	XZP	y1	y: -10	
	XZP	y2	y: 10	
		distance from primary beam to first det. plane		
	XYP	z1	z: 26	
		distance from primary beam to second det. plane		
	XYP	z2	z: 28	
		distance from primary beam to centre conv		
	XYP	z3	z: 25.25	
	END			
	REGION	BLKBODY		Neigh: 5
		expr: +blkbody -void		
	REGION	VOID		Neigh: 5
		expr: +void -room		
	REGION	ROOM1		Neigh: 5
		expr: +room -water-convert +z3		
	REGION	ROOM2		Neigh: 5
		expr: +room -x1 +x2 -z2		
	REGION	ROOM3		Neigh: 5
		expr: +room +x1-z1		
	REGION	ROOM4		Neigh: 5
		expr: +room -x2 -z1		
		two next regions are on the side of PLVOL , but within x bounds of PLVOL , thus not covered by room 3/4		
	REGION	ROOM6		Neigh: 5
		expr: +room -x1 +x2 +y1 -z1 +z2		
	REGION	ROOM7		Neigh: 5
		expr: +room -x1+x2 -y2 -z1 +z2		
	REGION	PLVOL		Neigh: 5
		expr: +x2 +z2 -x1 +y2 -y1 -z1 +z2		
	REGION	WATER		Neigh: 5
		expr: +water		
	REGION	CONV		Neigh: 5
		expr: +convert		
	REGION	ROOM5		Neigh: 5
		expr: +room -convert +z1 -z3		
	END			
	GEOEND			
	COMPOUND	f1: 1.25 f3: Z:	Name: EJ309 M1: HYDROGEN M3: Am: EJ309	Mix: Atom f2: 1.0 # A: p: 0.959 dE/dx:
	MATERIAL	..+...1...+...2...+...3...+...4...+...5...+...6...+...7..	Mat: BLCKHOLE Mat(Decay): Mat: VACUUM Mat(Decay): Mat: AIR Mat(Decay): Mat: EJ309 Mat(Decay): Mat: AIR Mat(Decay): Mat: WATER Mat(Decay): Mat: AIR Mat(Decay):	Reg: BLKBODY Step: Reg: VOID Step: Reg: ROOM1 Step: Reg: CONV Step: Reg: ROOM1 Step: Reg: WATER Step: Reg: ROOM7 Step:
	ASSIGNMA			to Reg: Field: to Reg: Field: to Reg: PLVOL Field: to Reg: Field: to Reg: PLVOL Field: to Reg: Field: to Reg: Field:
	PHYSICS	#if coal_evap	Type: COALESCE Type: EVAPORAT Zmax: 0	Activate: On Model: New Evap with heavy frag Amax: 0
	IONTRANS	#if iontrans	Transport: HEAVYION	
	USERDUMP	#endif	Type: Dump What: Complete	Unit: 70 Score: All Unit: 50 BIN Name: dose
	USRBIN	Type: X-Y-Z Part: DOSE	Xmin: 0 Ymin: -30 Zmin: -30	Unit: 50 BIN NX: 240 NY: 240 NZ: 240
	USRBIN	Type: X-Y-Z Part: PROTON	Xmin: 0 Ymin: -30 Zmin: -30	Unit: 51 BIN NX: 240 NY: 240 NZ: 240
	USRBIN	Type: X-Y-Z Part: NEUTRON	Xmin: 0 Ymin: -30 Zmin: -30	Unit: 52 BIN NX: 240 NY: 240 NZ: 240
	USRBIN	Type: X-Y-Z Part: PHOTON	Xmin: 0 Ymin: -30 Zmin: -30	Unit: 53 BIN NX: 240 NY: 240 NZ: 240

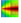
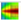







 <b>USRBIN</b>	Type: X-Y-Z ▼ Part: 4-HELIUM ▼	Xmin: 0 Ymin: -30 Zmin: -30	Unit: 54 BIN ▼ Xmax: 60 Ymax: 30 Zmax: 30	Name: <b>alpha flu</b> NX: 240 NY: 240 NZ: 240
 <b>USRBIN</b>	Type: X-Y-Z ▼ Part: DOSE ▼	Xmin: 0 Ymin: -1 Zmin: -1	Unit: 55 BIN ▼ Xmax: 35 Ymax: 1 Zmax: 1	Name: <b>dose1d</b> NX: 700 NY: 1 NZ: 1
 <b>USRBDX</b>	Type: Φ1, LinE, LinΩ ▼ Part: NEUTRON ▼	Reg: ROOM1 ▼ Emin: 0 Ωmin:	Unit: 21 BIN ▼ to Reg: CONV ▼ Emax: 0.25 Ωmax:	Name: <b>Nspect</b> Area: 400 Ebins: 300 Ωbins:
 <b>USRBDX</b>	Type: Φ1, LinE, LinΩ ▼ Part: PROTON ▼	Reg: ROOM1 ▼ Emin: 0 Ωmin:	Unit: 25 BIN ▼ to Reg: CONV ▼ Emax: 0.25 Ωmax:	Name: <b>Pspect</b> Area: 400 Ebins: 250 Ωbins:
 <b>USRBDX</b>	Type: Φ1, LinE, LinΩ ▼ Part: PHOTON ▼	Reg: ROOM1 ▼ Emin: 0 Ωmin:	Unit: 29 BIN ▼ to Reg: CONV ▼ Emax: 0.025 Ωmax:	Name: <b>Phspect</b> Area: 400 Ebins: 250 Ωbins:
 <b>USRBDX</b>	Type: Φ1, LinE, LinΩ ▼ Part: 4-HELIUM ▼	Reg: ROOM1 ▼ Emin: 0 Ωmin:	Unit: 33 BIN ▼ to Reg: CONV ▼ Emax: 0.25 Ωmax:	Name: <b>Aspect</b> Area: 400 Ebins: 250 Ωbins:
<a href="#">Set the random number seed</a>		Unit 01 ▼	Seed:	
 <b>RANDOMIZ</b>		Set the number of primary histories to be simulated in the run		
 <b>START</b>		No.: 100000000 Time:	Core: ▼ Report: default ▼	
 <b>STOP</b>				

Figure A-1: Screenshot of the FLUKA input for 20x20 cm<sup>2</sup> water phantom. The input specifies the properties of the simulation, e.g. geometry, beam properties, material definitions and assignments, scoring and physics cards.

## Appendix B – Tracking code

### B.1 bxdraw\_rangeveri.f

FLUKA user routine, used to store information (i.e. position, energy and angular distribution) about the produced secondaries and information at the converter boundary. The tracking code is from the water phantom simulations.

```
*$ CREATE MGDRAW.FOR
*COPY MGDRAW

*==== mgdraw =====*
*
  SUBROUTINE MGDRAW ( ICODE, MREG )

  INCLUDE ' (DBLPRC) '
  INCLUDE ' (DIMPAR) '
  INCLUDE ' (IOUNIT) '
*
*-----*
*
*   Copyright (C) 1990-2013      by      Alfredo Ferrari
*   All Rights Reserved.
*
*
*   MaGnetic field trajectory DRAWing: actually this entry manages
*                                       all trajectory dumping for
*                                       drawing
*
*   Created on   01 March 1990   by      Alfredo Ferrari
*                                       INFN - Milan
*   Last change  12-Nov-13      by      Alfredo Ferrari
*                                       INFN - Milan
*
*-----*
*
  INCLUDE ' (CASLIM) '
  INCLUDE ' (COMPUT) '
  INCLUDE ' (SOURCM) '
  INCLUDE ' (FHEAVY) '
  INCLUDE ' (FLKSTK) '
  INCLUDE ' (GENSTK) '
  INCLUDE ' (MGDDCM) '
  INCLUDE ' (PAPROP) '
  INCLUDE ' (QUEMGD) '
  INCLUDE ' (SUMCOU) '
  INCLUDE ' (TRACKR) '
*
  DIMENSION DTQUEN ( MXTRCK, MAXQMG )
*
  CHARACTER*20 FILNAM
  LOGICAL LFCOPE
  SAVE LFCOPE
```

```

DATA LFCOPE / .FALSE. /
*-----*
*
* Icode = 1: call from Kaskad
* Icode = 2: call from Emfsco
* Icode = 3: call from Kasneu
* Icode = 4: call from Kashea
* Icode = 5: call from Kasoph
*
*-----*
*
IF ( .NOT. LFCOPE ) THEN
  LFCOPE = .TRUE.
  IF ( KOMPUT .EQ. 2 ) THEN
    FILNAM = '//CFDRAW(1:8)//' DUMP A'
  ELSE
    FILNAM = CFDRAW
  END IF
  OPEN ( UNIT = IODRAW, FILE = FILNAM, STATUS = 'NEW', FORM =
&      'UNFORMATTED' )
  END IF
* +-----*
* | Quenching is activated
* IF ( LQEMGD ) THEN
*   IF ( MTRACK .GT. 0 ) THEN
*     RULLL = ZERZER
*     CALL QUENMG ( ICODE, MREG, RULLL, DTQUEN )
*     WRITE (IODRAW) ( ( SNGL (DTQUEN (I,JBK)), I = 1, MTRACK ),
* &                   JBK = 1, NQEMGD )
*   END IF
* END IF
* | End of quenching
* +-----*
--*
RETURN
*
*=====*
*
* Boundary-(X)crossing DRAWing:
*
* Icode = 1x: call from Kaskad
*           19: boundary crossing
* Icode = 2x: call from Emfsco
*           29: boundary crossing
* Icode = 3x: call from Kasneu
*           39: boundary crossing
* Icode = 4x: call from Kashea
*           49: boundary crossing
* Icode = 5x: call from Kasoph
*           59: boundary crossing
*
*=====*
*
ENTRY BXDRAW ( ICODE, MREG, NEWREG, XSCO, YSCO, ZSCO )
*****Code by Kristian*****
*mreg:region before crossing
*nreg:region after crossing

```

```

*write crossing coords. to file(41) in pairs:
*Add ncase (history number) to make sure it is the same particle
*crossing both planes
*Jtrack=1 means particle is proton (neutrons = 8)

*plane 1: crossing regions 3 to 9
  IF(MREG .EQ. 3 .AND. NEWREG .EQ. 9) THEN
    IF (JTRACK .EQ. 1) THEN
      EKPART=ETRACK-AM(JTRACK)

*      If proton is from converter:
        IF(ISPUSR(1) .EQ. 8) THEN
*      Ek-proton calculated as totale - Emass (0.938272...)
          NCASE1=NCASE
          X1=XSCO
          Y1=YSCO
          Z1=ZSCO
          EK1=EKPART
          ox=SPAUSR(1)
          oy=SPAUSR(2)
          oz=SPAUSR(3)
          ocx=SPAUSR(4)
          ocy=SPAUSR(5)
          ocz=SPAUSR(6)
          EKo=SPAUSR(7)
          id=SPAUSR(8)
          pid=SPAUSR(9)
*dir cos from TRACKR Cx,y,ztrck
          Pcos1x=CXTRCK
          Pcos1y=CYTRCK
          Pcos1z=CZTRCK
*      next step: write to files only if NCASE1=NCASE2

          ENDIF
        ENDIF
      ENDIF
*Plane 2: crossing regions 9 to 4
  IF(MREG .EQ. 9 .AND. NEWREG .EQ. 4) THEN
    IF (JTRACK .EQ. 1 .AND. ISPUSR(1) .EQ. 8) THEN
      EKPART=ETRACK-AM(JTRACK)

* Write new file with all info if Ncase matches for plane
* one and two
      IF(NCASE .EQ. NCASE1) THEN
        WRITE(46,*) X1,Y1,Z1,EK1,NCASE1,
          &          ox,oy,oz,ocx,ocy,ocz,EKo,
          &          Pcos1x,Pcos1y,Pcos1z,ISPUSR(2),id, pid
*      WRITE(46,*) XSCO,YSCO,ZSCO,EKPART,NCASE,
          &          SPAUSR(1), SPAUSR(2), SPAUSR(3),
          &          SPAUSR(4), SPAUSR(5), SPAUSR(6), SPAUSR(7),
          &          CXTRCK,CYTRCK,CZTRCK,ISPUSR(2),SPAUSR(8),SPAUSR(9)
        ENDIF
      ENDIF
    ENDIF
  ENDIF
*****END OF CODE MODIFIED BY KRISTIAN*****
*****Code by Eidi*****
*PHOTON

```

```

*plane 1: crossing regions 3 to 9
  IF(MREG .EQ. 3 .AND. NEWREG .EQ. 9) THEN
    IF (JTRACK .EQ. 7) THEN
      EKPART=ETRACK-AM(JTRACK)
      WRITE(47,*) XSCO,YSCO,ZSCO,EKPART,NCASE,
&      CXTRCK,CYTRCK,CZTRCK
      ENDIF
    ENDIF
  ENDIF

*****
*PROTON

*plane 1: crossing regions 3 to 9
  IF(MREG .EQ. 3 .AND. NEWREG .EQ. 9) THEN
    IF (JTRACK .EQ. 1) THEN
      EKPART=ETRACK-AM(JTRACK)
      WRITE(48,*) XSCO,YSCO,ZSCO,EKPART,NCASE,
&      CXTRCK,CYTRCK,CZTRCK
      ENDIF
    ENDIF
  ENDIF

*****
*ALPHA

*plane 1: crossing regions 3 to 9
  IF(MREG .EQ. 3 .AND. NEWREG .EQ. 9) THEN
    IF (JTRACK .EQ. -6) THEN
      EKPART=ETRACK-AM(JTRACK)
      WRITE(49,*) XSCO,YSCO,ZSCO,EKPART,NCASE,
&      CXTRCK,CYTRCK,CZTRCK
      ENDIF
    ENDIF
  ENDIF

*****
*NEUTRON

*plane 1: crossing regions 3 to 9
  IF(MREG .EQ. 3 .AND. NEWREG .EQ. 9) THEN
    IF (JTRACK .EQ. 8) THEN
      EKPART=ETRACK-AM(JTRACK)
      WRITE(45,*) XSCO,YSCO,ZSCO,EKPART,NCASE,
&      CXTRCK,CYTRCK,CZTRCK,ISPUSR(2)
      ENDIF
    ENDIF
  ENDIF

  RETURN
*****END OF CODE MODIFIED BY EIDI*****
*
*
*=====
*
*      Event End DRAWing:
*
*

```

```

*=====*
*
*   ENTRY EEDRAW ( ICODE )
*   RETURN
*
*=====*
*
*   ENergy deposition DRAWing:
*
*   Icode = 1x: call from Kaskad
*           10: elastic interaction recoil
*           11: inelastic interaction recoil
*           12: stopping particle
*           13: pseudo-neutron deposition
*           14: escape
*           15: time kill
*   Icode = 2x: call from Emfsco
*           20: local energy deposition (i.e. photoelectric)
*           21: below threshold, iarg=1
*           22: below threshold, iarg=2
*           23: escape
*           24: time kill
*   Icode = 3x: call from Kasneu
*           30: target recoil
*           31: below threshold
*           32: escape
*           33: time kill
*   Icode = 4x: call from Kashea
*           40: escape
*           41: time kill
*           42: delta ray stack overflow
*   Icode = 5x: call from Kasoph
*           50: optical photon absorption
*           51: escape
*           52: time kill
*
*=====*
*
*   ENTRY ENDRAW ( ICODE, MREG, RULL, XSCO, YSCO, ZSCO )
*   IF ( .NOT. LFCOPE ) THEN
*       LFCOPE = .TRUE.
*       IF ( KOMPUT .EQ. 2 ) THEN
*           FILNAM = '/'//CFDRAW(1:8)//' DUMP A'
*       ELSE
*           FILNAM = CFDRAW
*       END IF
*       OPEN ( UNIT = IODRAW, FILE = FILNAM, STATUS = 'NEW', FORM =
&           'UNFORMATTED' )
*       END IF
*       WRITE (IODRAW) 0, ICODE, JTRACK, SNGL (ETRACK), SNGL (WTRACK)
*       WRITE (IODRAW) SNGL (XSCO), SNGL (YSCO), SNGL (ZSCO), SNGL
(RULL)
*   +-----*
*   | Quenching is activated : calculate quenching factor
*   | and store quenched energy in DTQUEN(1, jbk)
*   IF ( LQEMGD ) THEN
*       RULLL = RULL
*       CALL QUENMG ( ICODE, MREG, RULLL, DTQUEN )

```

```

*          WRITE (IODRAW) ( SNGL (DTQUEN(1, JBK)), JBK = 1, NQEMGD )
*          END IF
* | end quenching
* +-----*
*          RETURN
*
*=====*
*
*          SOurce particle DRAWing:
*
*=====*
*
*          ENTRY SODRAW
*          IF ( .NOT. LFCOPE ) THEN
*
*          END IF
*          WRITE (IODRAW) -NCASE, NPFLKA, NSTMAX, SNGL (TKESUM),
*          &
*          SNGL (WEIPRI)
* +-----*
* | (Radioactive) isotope: it works only for 1 source particle on
* | the stack for the time being
* IF ( ILOFLK (NPFLKA) .GE. 100000 .AND. LRADDC (NPFLKA) ) THEN
*     IARES = MOD ( ILOFLK (NPFLKA), 100000 ) / 100
*     IZRES = MOD ( ILOFLK (NPFLKA), 10000000 ) / 100000
*     IISRES = ILOFLK (NPFLKA) / 10000000
*     IONID = ILOFLK (NPFLKA)
*     WRITE (IODRAW) ( IONID, SNGL (-TKEFLK(I)),
*     &
*     SNGL (WTFLK(I)), SNGL (XFLK (I)),
*     &
*     SNGL (YFLK (I)), SNGL (ZFLK (I)),
*     &
*     SNGL (TXFLK(I)), SNGL (TYFLK(I)),
*     &
*     SNGL (TZFLK(I)), I = 1, NPFLKA )
* |
* +-----*
* | Patch for heavy ions: it works only for 1 source particle on
* | the stack for the time being
* ELSE IF ( ABS (ILOFLK (NPFLKA)) .GE. 10000 ) THEN
*     IONID = ILOFLK (NPFLKA)
*     CALL DCDION ( IONID )
* |
* +-----*
* | Patch for heavy ions: ???
* ELSE IF ( ILOFLK (NPFLKA) .LT. -6 ) THEN
*     WRITE (IODRAW) ( IONID, SNGL (TKEFLK(I)+AMNHEA(-
ILOFLK(NPFLKA))),
*     &
*     SNGL (WTFLK(I)), SNGL (XFLK (I)),
*     &
*     SNGL (YFLK (I)), SNGL (ZFLK (I)),
*     &
*     SNGL (TXFLK(I)), SNGL (TYFLK(I)),
*     &
*     SNGL (TZFLK(I)), I = 1, NPFLKA )
* |
* +-----*
* |
* ELSE
*     WRITE (IODRAW) ( ILOFLK(I), SNGL (TKEFLK(I)+AM(ILOFLK(I))),
*     &
*     SNGL (WTFLK(I)), SNGL (XFLK (I)),
*     &
*     SNGL (YFLK (I)), SNGL (ZFLK (I)),
*     &
*     SNGL (TXFLK(I)), SNGL (TYFLK(I)),
*     &
*     SNGL (TZFLK(I)), I = 1, NPFLKA )
* END IF

```



```

* |
* +-----+
*   RETURN
*
*=====
*
*   USer dependent DRAWing:
*
*   Icode = 10x: call from Kaskad
*       100: elastic interaction secondaries
*       101: inelastic interaction secondaries
*       102: particle decay secondaries
*       103: delta ray generation secondaries
*       104: pair production secondaries
*       105: bremsstrahlung secondaries
*       110: decay products
*   Icode = 20x: call from Emfsco
*       208: bremsstrahlung secondaries
*       210: Moller secondaries
*       212: Bhabha secondaries
*       214: in-flight annihilation secondaries
*       215: annihilation at rest secondaries
*       217: pair production secondaries
*       219: Compton scattering secondaries
*       221: photoelectric secondaries
*       225: Rayleigh scattering secondaries
*       237: mu pair production secondaries
*   Icode = 30x: call from Kasneu
*       300: interaction secondaries
*   Icode = 40x: call from Kashea
*       400: delta ray generation secondaries
*   For all interactions secondaries are put on GENSTK common (kp=1,np)
*   but for KASHEA delta ray generation where only the secondary elec-
*   tron is present and stacked on FLKSTK common for kp=npflka
*
*=====
*
*   ENTRY USDRAW ( ICODE, MREG, XSCO, YSCO, ZSCO )
*   ***** START ADDED BY KRISTIAN IN USDRAW*****
*   *input to mgdraw to write all positions for created neutrons in
*   *water (currently region no. 10)
*   **   WRITE(65,*) XSCO, YSCO, ZSCO, CXR (IP), CYR(IP),KPART(IP)
*
*
*   IF(ICODE .EQ. 101 .AND. MREG .EQ. 10) THEN
*       DO IP = 1, NP
*           IF(KPART(IP) .EQ. 8) THEN
*   *   Store origin of neutron (x,y,z)
*           i=i+1
*           IF (i .GT. 100) THEN
*               WRITE(65,*) XSCO,YSCO,ZSCO,Tki(IP),
*   &               Cxr(IP),Cyr(IP),Czr(IP)
*
*
*           WRITE(61,*) XSCO, Tki(IP)
*           i = 1
*       ENDIF
*   ENDIF

```

```

        END DO
        END IF
*
* Np = total number of secondaries *
* Kpart (ip) = (Paprop) id of the ip_th secondary *
* Cxr (ip) = x-axis direction cosine of the ip_th secondary *
* Tki (ip) = laboratory kinetic energy of ip_th secondary (GeV)*
* Wei (ip) = statistical weight of the ip_th secondary *
* etc. (look up the full list in $FLUPRO/flukapro/(GENSTK)
***** END ADDED BY KRISTIAN IN USDRAW*****

***** START ADDED BY EIDI*****
*input to mgdraw to write all positions for created gamma-rays, protons
and alpha in water

*PHOTON
  IF(ICODE .EQ. 101 .AND. MREG .EQ. 10) THEN
    DO IP = 1, NP
      IF(KPART(IP) .EQ. 7) THEN
*      Store origin of gamma (x,y,z)
        i = i + 1
        IF (i .GT. 100) THEN
          WRITE(66,*) XSCO,YSCO,ZSCO,Tki(IP),
&          Cxr(IP),Cyr(IP),Czr(IP)
          i = 1
        ENDIF
      ENDIF
    END DO
  END IF

*PROTON
  IF(ICODE .EQ. 101 .AND. MREG .EQ. 10) THEN
    DO IP = 1, NP
      IF(KPART(IP) .EQ. 1) THEN
*      Store origin of proton (x,y,z)
        i = i + 1
        IF (i .GT. 100) THEN
          WRITE(67,*) XSCO,YSCO,ZSCO,Tki(IP),
&          Cxr(IP),Cyr(IP),Czr(IP)
          i = 1
        ENDIF
      ENDIF
    END DO
  END IF

*ALPHA
  IF(ICODE .EQ. 101 .AND. MREG .EQ. 10) THEN
    DO IP = 1, NP
      IF(KPART(IP) .EQ. -6) THEN

*      Store origin of alpha (x,y,z)
        WRITE(68,*) XSCO,YSCO,ZSCO,Tki(IP),
&          Cxr(IP),Cyr(IP),Czr(IP)
        ENDIF

```

```

        END DO
    END IF

*
* Np = total number of secondaries *
* Kpart (ip) = (Paprop) id of the ip_th secondary *
* Cxr (ip) = x-axis direction cosine of the ip_th secondary *
* Tki (ip) = laboratory kinetic energy of ip_th secondary (GeV)*
* Wei (ip) = statistical weight of the ip_th secondary *
* etc. (look up the full list in $FLUPRO/flukapro/(GENSTK)
***** END ADDED BY EIDI*****

    IF ( .NOT. LFCOPE ) THEN
        LFCOPE = .TRUE.
        IF ( KOMPUT .EQ. 2 ) THEN
            FILNAM = '/'//CFDRAW(1:8)//' DUMP A'
        ELSE
            FILNAM = CFDRAW
        END IF
        OPEN ( UNIT = IODRAW, FILE = FILNAM, STATUS = 'NEW', FORM =
&          'UNFORMATTED' )
    END IF
* No output by default:
    RETURN
*=== End of subroutine Mgdraw =====*
    END

```

## B.2 Quantities restored

Table B-1: Overview of created secondaries with correlating output file number from the tracking code, and the quantities restored for this thesis.

	Water phantom/patient				Converter			
<b>Secondaries</b>	Proton	Gamma	Neutron	Alpha	Proton	Gamma	Neutron	Alpha
<b>File nr.</b>	67	66	65	68	48	47	45	49
<b>Quantities restored</b>	XSCO = position of creation (x-coord.) Tki(IP) = kinetic energy Cxr(IP), Cyr(IP), Czr(IP) = xyz-direction cosine				The number of secondary particles at the converter surface			

# Appendix C – Results from MC simulations

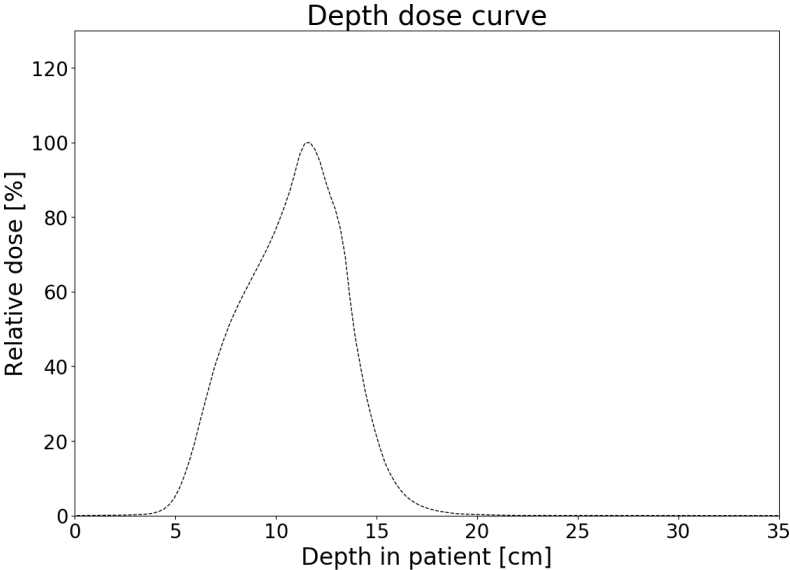


Figure C-1: Depth dose curve for the minimum proton beam energy in the SOBP, with 100 % relative dose at 11.6 cm.

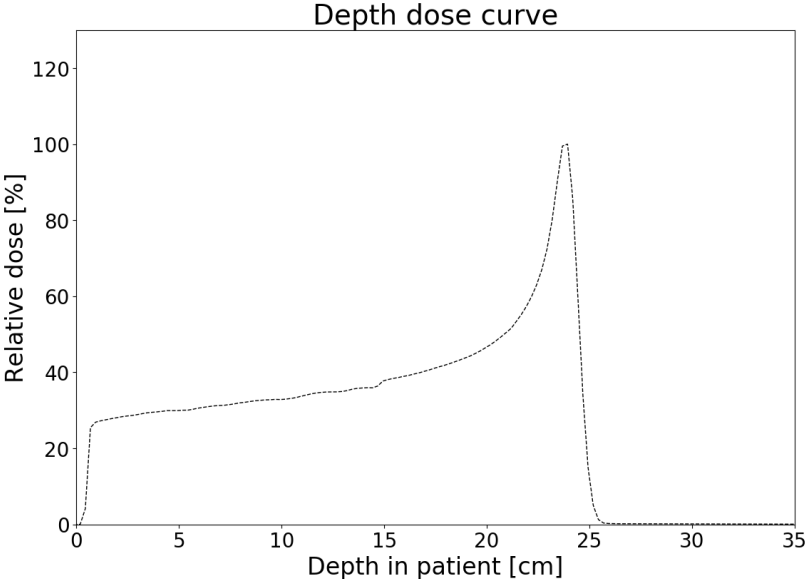


Figure C-2: Depth dose curve for the maximum proton beam energy in the SOBP, with 100 % relative dose at 23.8 cm.

Table C-1: Particle rate per primary proton in the water phantom and at the converter. The percentage of the secondaries reaching the convert from the ones created are also presented.

<b>Secondary particle</b>	<b>Proton</b>				<b>Gamma</b>				<b>Neutron</b>			
<b>Beam energy [MeV]</b>	100	160	200	230	100	160	200	230	100	160	200	230
<b>Production rate [p pr<sup>-1</sup>]</b>	0.12	0.25	0.36	0.45	0.04	0.078	0.10	0.12	0.03	0.085	0.13	0.18
<b>Particle rate – converter [p pr<sup>-1</sup>]</b>	2.3x10 <sup>-6</sup>	3.0x10 <sup>-5</sup>	2.4x10 <sup>-4</sup>	6.8x10 <sup>-4</sup>	2.3x10 <sup>-3</sup>	4.6x10 <sup>-3</sup>	5.6x10 <sup>-3</sup>	5.7x10 <sup>-3</sup>	7.4x10 <sup>-4</sup>	2.5x10 <sup>-3</sup>	4.0x10 <sup>-3</sup>	4.8x10 <sup>-3</sup>
<b>Reaching the converter [%]</b>	0.002	0.012	0.067	0.151	5.75	5.75	5.6	4.75	2.47	3.1	3.08	2.67

Table C-2: Particle rate per primary proton in the patient and at the converter.

<b>Secondary particle</b>	<b>Proton</b>	<b>Gamma</b>	<b>Neutron</b>
<b>Production rate [p pr<sup>-1</sup>]</b>	0.26	0.07	0.09
<b>Particle rate – converter [p pr<sup>-1</sup>]</b>	0.0001	0.005	0.003
<b>Reaching the converter [%]</b>	0.05	6.5	3.1